Technische Universität München
Lehrstuhl für Leichtbau

Design and optimization of high speed rotating CFRP disks with regard to their vibration behavior

Matthias Weinzierl

Vollständiger Abdruck der von der Fakultät für Maschinenwesen der Technischen Universität München zur Erlangung des akademischen Grades eines

Doktor-Ingenieurs (Dr.-Ing.)

genehmigten Dissertation.

Vorsitzender: Prof. dr. ir. Daniel J. Rixen

Prüfer der Dissertation:

1. Prof. Dr.-Ing. Horst Baier

2. Prof. Dr.-Ing. Manfred Hajek

Die Dissertation wurde am 10.08.2017 bei der Technischen Universität München eingereicht und durch die Fakultät für Maschinenwesen am 26.01.2018 angenommen.

♦ **Dedication** ♦

To Theodor.

Acknowledgements

First and foremost, I would like to express my sincere gratitude to my advisor Professor Dr.-Ing. Horst Baier, for his continuous support of my PhD study and related research during my whole time at the Chair of Lightweight Structures. He gave me a lot of freedom in my research field and his guidance helped me in all the time of research. I would also like to thank Prof. Dr.-Ing. Hajek and Prof. Dr. Rixen for supporting this thesis by being active members of the adjudication committee.

My sincere thanks also go to all of my colleagues at the Chair of Lightweight Structures (LLB) at Technische Universität München. The friendly and kind atmosphere gave me the basis for my work and research. A special thank you goes to my colleague, friend and fellow roommate Dipl.-Ing. Johannes Achleitner, who helped turn my time at LLB into a very productive and fruitful one.

Lastly, I would like to thank my wife and my parents for all their support and encouragement.

München, 10.08.2017 Matthias Weinzierl

List of own publications

This thesis is based on the following publications and working papers.

- M. Weinzierl, M. Schatz, V. Antonelli, and H. Baier. Structural design optimization of CFRP chopper disks. *Composite Structures*, 140:351–359, Apr. 2016. ISSN 0263-8223. doi: http://dx.doi.org/10.1016/j.compstruct.2015.12.016
- M. Weinzierl, V. Antonelli, M. Schatz, and H. Baier. A study of the structural dynamics of CFRP chopper disks. In *Proceedings of the 9th SAMPE Europe Technical Conference of the Society for the Advancement of Materials and Process Engineering*, pages 172–178, Sept. 2014. ISBN: 978-90-821727-1-3
- M. Weinzierl, M. Schatz, V. Antonelli, and H. Baier. Structural Design Optimization of CFRP Chopper Disks. In *Proceedings of ICCS 18 – 18th International Conference on Composite Structures*, Lisbon, June 2015
- M. Weinzierl, V. Antonelli, and H. Baier. Design and certification of the chopper disks for the NEAT II TOF spectrometer. In *Proceedings of ECCM 17 – 17th European Conference on Composite Materials*, Munich, June 2016. ISBN: 978-3-00-053387-7
- M. Weinzierl and H. Baier. Leichtbau bei extrem schnell rotierenden Scheiben für neutronenphysikalische Versuchsanlagen. In *Technisch-wissenschaftliche Seminarreihe: Hochleistungsstrukturen im Leichtbau*, Garching bei München, Dec. 2015. Lehrstuhl für Leichtbau
- M. Weinzierl and H. Baier. Design and optimization of a hub for a CFRP disk rotating at a very high speed. In *Proceedings of ICCS 19 – 19th International Conference on Composite Structures*, Porto, Sept. 2016
- M. Weinzierl, H. Baier, L. Krämer, and V. Antonelli. Design and certification of the chopper disks for the NEAT II TOF spectrometer: A lesson learned. In *Proceedings of DENIM 2015 – 4th Design and Engineering of Neutron Instruments Meeting*, Budapest, Sept. 2015
- M. Weinzierl and H. Baier. Chopper Supplier Forum 2016 Chopper disk manufacturer update. In *Proceedings of DENIM 2016 – 5th Design and Engineering of Neutron Instruments Meeting*, Lund, Sept. 2016

Abstract

Carbon fiber reinforced plastic disks with a diameter of up to 1 000 mm and rotational speeds in vacuum aimed for up to 500 Hz (30 000 rpm) are studied for their vibration behavior in this dissertation. One specific application of such disks is the neutron Time-of-Flight spectroscopy. These disks have one or more cut-outs, which causes stress peaks in the structure. The strength and the vibration behavior of such disks are researched in detail in this thesis, and proper design and material selections are chosen. The interaction between the disk and the hub on which the disk is mounted, as well as the structural dynamics of the whole system are in the focus of the studies. In particular, the effect of the membrane stiffening of the disk, which is caused by the centrifugal forces during rotation, is quantified. An improved design is achieved by numerical design optimization methods, which additionally to the vibration behavior take into account strength and manufacturing constraints. The computed results are validated by experimental testing. It is shown that the dynamic and strength tests confirm the calculated results. The maximum rotational speed of the disk could in total be increased by 25 % compared to the empirically determined initial design.

Kurzfassung

Scheiben aus kohlenstofffaserverstärktem Kunststoff mit einem Durchmesser von bis zu einem Meter und Drehzahlen im Vakuum von bis zu 500 Hz werden in dieser Dissertation auf ihr Vibrationsverhalten hin untersucht. Eine spezifische Anwendung stellt die Neutronen Flugzeitspektroskopie dar. Die oben genannten Scheiben haben meist mehrere Ausschnitte, was Spannungsspitzen in der Struktur hervorruft. Die Festigkeit sowie das Vibrationsverhalten solcher Scheiben werden in dieser Arbeit detailliert untersucht und beschrieben sowie passende Design- und Materialauswahlen getroffen. Die wechselseitigen Einflüsse, die die Scheibe und die Nabe aufeinander ausüben, sowie das komplette Scheibensystem stehen im Fokus dieser Studie. Im Speziellen wird auf den Effekt der Membranversteifung der Scheibe durch die Zentrifugalkräfte im rotierenden Zustand eingegangen. Ein verbessertes Design wird mittels numerischer Strukturoptimierungsmethoden erreicht, welche zusätzlich zu dem Vibrationsverhalten Festigkeits- und Fertigungsrestriktionen berücksichtigen. Die berechneten Ergebnisse werden durch experimentelle Tests validiert. Es wird gezeigt, dass sowohl die dynamischen Messungen als auch die Berstversuche die Berechnungen bestätigen. Die maximale Drehzahl konnte im Vergleich zu einem empirisch ermittelten Ausgangsdesign um 25 % gesteigert werden.

Contents

List of Figures

List of Tables

Nomenclature

α	Thermal expansion coefficient
$\boldsymbol{\rho_e}$	Vector of element density
$\boldsymbol{B}$	Gyroscopic matrix of small foot point excitation
$\boldsymbol{C}$	Elasticity tensor
$\boldsymbol{D}$	Damping matrix
$\boldsymbol{K(U)}$	Stiffness matrix, nonlinear
$\boldsymbol{K_{const}}$	Stiffness matrix, constant
$\boldsymbol{K}$	Stiffness matrix
$\boldsymbol{M}$	Mass matrix
$\boldsymbol{N}$	Gyroscopic matrix of elastic deflection
$\boldsymbol{U}$	Nodal displacement
$\boldsymbol{V}$	Transposition matrix
Δ	Laplace operator
η_s	Slave node
Γ_m	Master surface
λ	Empirical factor for the calculation of natural frequencies
g	Acceleration of gravity
μ	Coefficient of friction
∇	Nabla operator
ν	Poisson's ratio
Ω	Continuum body
ω	Angular frequency
$\Omega(\mathbf{x_S})$	Domain of the shape variables
ω_n	Angular frequency of the disk
ω_{cyc}	Rotational speed
$\omega_{e\omega}$	Angular frequency of natural frequency $f_{e\omega}$
ρ	Specific gravity
σ_r	Radial stress
τ_m	Shear strength of an isotropic material
ε	Mechanical strain
φ	Angle in polar coordinate system
ϱ	Density
ϱ^*	Closest point

$\sigma^{\mathbf{u}}$ ..... Stress field
$\mathbf{b_k}$ ..... Base vector
$\mathbf{F}_l$ ..... Nodal force vector, linear
$\mathbf{F}_{nl}$ ..... Nodal force vector, nonlinear
$\mathbf{g}$ ..... Vector of inequality constraints
$\mathbf{h}$ ..... Vector of equality constraints
$\mathbf{t_P}$ ..... Vector of ply thicknesses
$\mathbf{u_i}$ ..... Displacement field
$\mathbf{x_S}$ ..... Vector of shape variables
$\mathbf{x}$ ..... Vector of design variables
$\mathbf{z}$ ..... Vector of objective functions
ξ ..... weight factor
$\{\mathbf{p}\}\boldsymbol{E}$ ..... Variable external loads
$\{\mathbf{s}\}\boldsymbol{E}$ ..... Small foot point or reference point excitation movement
$\{\mathbf{x}\}\boldsymbol{E}$ ..... Small grid point deflection
A ..... Lateral surface
d ..... Diameter
d_i ..... Inner diameter of a disk
d_j ..... Joint diameter
d_o ..... Outer diameter of a disk
$d_{i,hub}$ ..... Inner diameter of the hub
$d_{o,hub}$ ..... Outer diameter of the hub
E ..... Young's modulus
E_x ..... Young's modulus in x-direction
E_y ..... Young's modulus in y-direction
$E_\parallel$ ..... Young's modulus longitudinal
$E_\perp$ ..... Young's modulus transverse
E_{HS} ..... Young's modulus of the high stiffness laminate
E_{IS} ..... Young's modulus of the intermediate stiffness laminate
f_e ..... Natural frequency
F_f ..... Force of friction
F_n ..... Normal force
$f_{e,1}$ ..... First natural frequency
$f_{e,i}$ ..... i-th natural frequency
f_{st} ..... Parasitic frequency
FI ..... Failure index

$g_l(x_j)$ ..... Vector of inequality constraint functions
G_xy ..... Shear modulus in xy-plane
$G_{\parallel\perp}$ ..... Shear modulus
h ..... Thickness
$h_k(x_j)$ ..... Vector of equality constraint functions
k ..... Number of eigenmode
l_j ..... Length of the joint
m ..... Mass
N ..... Stiffness of a plate
n_{cn} ..... Set of nodes around the central through-hole of a disk
n_{DV} ..... Number of design variables
n_{EC} ..... Number of equality constraint functions
n_{f_e} ..... Number of considered natural frequencies
n_{IC} ..... Number of inequality constraint functions
n_{ON} ..... Set of nodes at the outer diameter of the hub
n_O ..... Number of objective functions
N_{SF} ..... Safety factor
p ..... Load per unit area
p_j ..... Joint pressure
r ..... Radius
$R_{\parallel}^{+}$ ..... Compression strength longitudinal
$R_{\parallel}^{-}$ ..... Tensile strength longitudinal
$R_{\perp}^{-}$ ..... Tensile strength transverse
r_i ..... Inner radius of a disk
R_m ..... Tensile strength of an isotropic material
r_o ..... Outer radius of a disk
$R_{\parallel\perp}$ ..... Shear strength
R_{ILSS} ..... Interlaminar shear strength
S_f ..... Safety against failure
S_g ..... Safety against gliding
T ..... Temperature
t ..... Time
u_r ..... Radial displacement
V ..... Volume
w ..... Deflection of a plate
x_j ..... Vector of design variables

z	Objective function
$z_i(x_j)$	Vector of objective functions
ALM	Additive Layer Manufacturing
BER II	Neutron source Helmholtz Zentrum Berlin II
CFRC	Carbon fiber reinforced carbon
CFRP	Carbon fiber reinforced plastic
ESS	Energy storage systems
FAA	Federal Aviation Administration
FEM	Finite element method
FESS	Flywheel energy storage systems
FRM II	Research Reactor Munich II
GFRP	Glass fiber reinforced plastic
LLB	Chair of Lightweight Structures
MFD	Method of feasible directions
MLZ	Heinz Maier-Leibnitz Zentrum
NEAT	Time-of-flight spectrometer of the Helmholtz neutron source
PDE	Partial differential equation
S2N	Surface to node
S2S	Surface to surface
TOF	Time-of-Flight
TUM	Technical University of Munich

1 Introduction

This first chapter gives an overview of the general functions of disks rotating at a high speed and of their fields of application.

Contents

1.1. Motivation

Disks rotating at a high or a very high speed are used in different fields of application. Up until now, such disks, which are made of carbon fiber reinforced plastic (CFRP), have had a diameter of up to 750 mm and have been aimed at reaching operational speeds of up to 500 Hz and above. These very high rotational speeds do not only cause a strength problem of the disks but also problems with the structural dynamics. Even small static or dynamic unbalancing leads to high loads on the disk as well as the bearings. In this dissertation, a deepened knowledge of the physics of such disks will be provided. Different methods of structural analysis and numerical design optimization will be applied to a specific CFRP disk. A major focus of the research will be placed on the optimization of the vibration behavior of the disks during rotation. Furthermore, the contact behavior between the disk and the hub will be taken into consideration during the design process of the entire system. An adequate material selection with regard to the strength of the disk will be made. With these methods, an enhancement of the disk considering its operational behavior and its rotational speed will be gained.

1.2. CFRP disks for time-of-flight experiments

In general, the Time-of-Flight (TOF) describes different methods of measuring the time of an object flying from one point to another. The object can be a particle, an atom or also an electromagnetic wave. The TOF method is commonly used in many scientific experiments involving neutron scattering. It allows for the investigation of a great variety of topics, e.g. diffusive processes in liquids and melts, high-frequency acoustic propagation, optical vibrational modes, magnetic excitations and tunneling spectroscopy [32, 33, 34]. In neutron TOF technique, a pulsed monochromatic beam strikes a test sample and the energies of the scattered neutrons are determined by their time of flight onto an array of detectors, as shown in figure 1.1 [66]. In the TOF spectrometer, several so-called chopper disks rotate around an axis parallel to the neutron beam, reaching operational speeds of up to 380 Hz. The disks can either be used to pulse the beam or as velocity filters, in order to monochromatize the beam. Acting as neutron selectors, their filtering ability is enhanced by utilizing neutron-absorbing materials. The area directly in contact with the beam is coated with a boron epoxy material, which prevents the neutrons from running through the disk. Consequently, only neutrons traveling across the cut-outs are extracted from the incoming beam [8, 35, 36, 118].

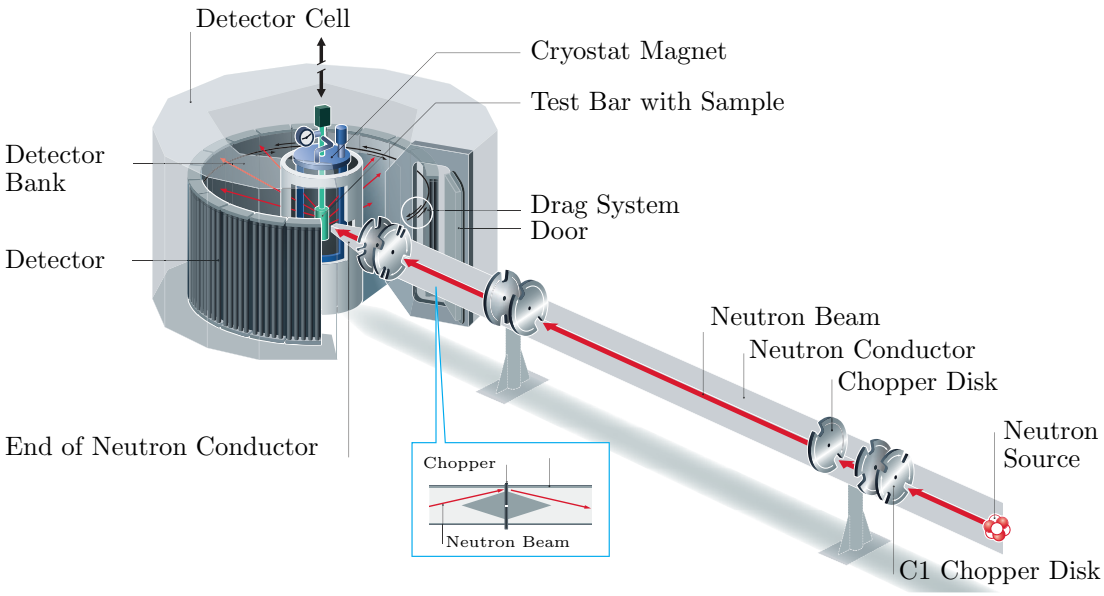

Figure 1.1.: Schematic plan of the TOF spectrometer NEAT II [66].

In the past, such disks were designed to be made of aluminum. Since the 2000s, the Chair of Lightweight Structures (LLB) of the Department of Mechanical Engineering

at Technical University of Munich (TUM) has specialized in the design and production of CFRP chopper disks. This change in material became necessary since the rotational speed of the disks increased and aluminum reached its strength limit. Quasi-isotropic CFRP has a higher weight-specific strength than aluminum. The typical diameter of a CFRP chopper disk is between 500 mm and 750 mm with a weight of approximately 6 kg [5, 6, 7, 9, 139]. The thickness distribution decreases from approximately 40 mm around the central through-hole to 1.5 mm at the outer diameter. The decrease in thickness distribution is based on a plane stress state assumption and on a constant stress disk profile [49, 137].

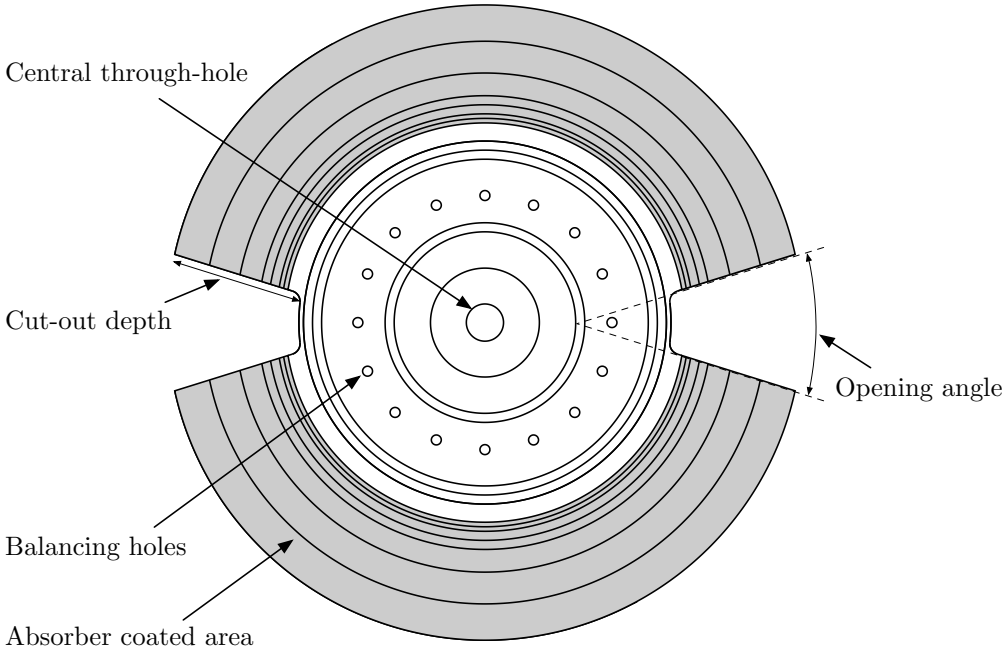

Figure 1.2.: Sketch of a chopper disk.

A general sketch of a chopper disk is shown in figure 1.2. The chopper disk is mounted in the central through-hole on a hub, which then is connected to the shaft. The inner plateau is designed to attach the disk to the hub and the outer plateau to get a planar surface for the drilling of the balancing holes. These holes are needed to add weights to the disk for dynamical balancing. A chopper disk has three major design constraints:

- Natural frequencies – vibrations during operation.
- Disk-hub connection – radial extension of the central through-hole.
- Strength – maximum stress due to centrifugal force.

A thicker cross section leads to a higher stiffness of the disk yet at the same time to higher centrifugal forces, caused by the additional mass. This inconsistency makes it difficult to design a chopper disk. Below, a method is described how to improve a chopper disk with a numerical optimization.

1.3. Retrospect of disk design

Originally, chopper disks were made of aluminum. Due to the higher weight-specific strength of CFRP compared to aluminum, fiber-reinforced disks were then established for chopper disk systems with high rotational speeds. CFRP chopper disks have been designed by LLB since 2003, specializing in designs for light disks with a high rotational speed [11, 103, 144]. Compared to an aluminum disk, the main advantages of a CFRP disk are the higher weight-specific strength and the better connection between the coating material and the disk. The coating material is a mixture of epoxy resin and neutron absorbing boron carbide. A drawback of CFRP disks are the manufacturing variances. Due to the autoclave process with high pressure and high temperatures during curing, the CFRP disk has internal stresses after the demolding, which leads to a higher axial run-out of the edges of the disk.

Three examples of chopper disk systems are presented in chapter 2. Disks made of aluminum are still in use, but only for chopper disk systems with a rotational speed of up to 250 Hz and a diameter of up to 600 mm [97, 98, 99, 115].

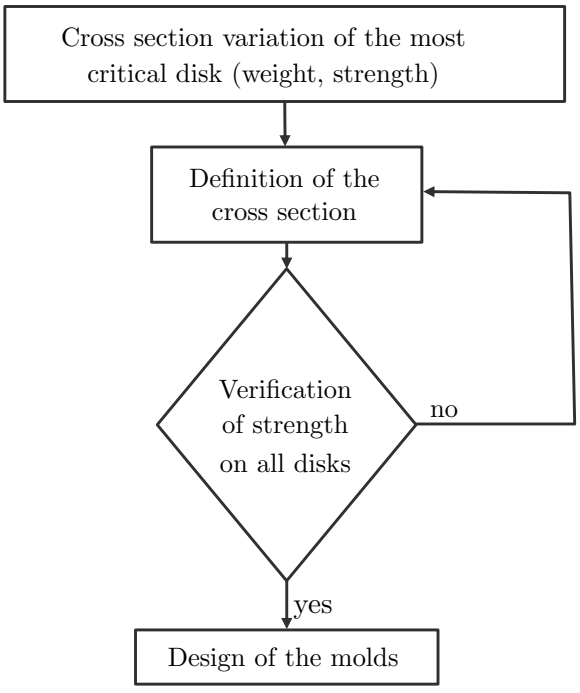

Figure 1.3.: Strength driven design process of chopper disks.

In the beginning, the design process of chopper disks was strength driven [3]. A chopper disk system is comprised of several disks, usually of four to seven disks. With regard to

manufacturing costs, it is beneficial to use one mold with one cross section for all the disks of the system. Therefore, the disk with the most critical cut-outs was chosen and a suitable cross section was defined. This cross section was verified for all other disks of the system. If the cross section was not suitable for one of the disks of the system, the cross section was revised until it fitted for all the disks. This pattern is shown in sketch 1.3.

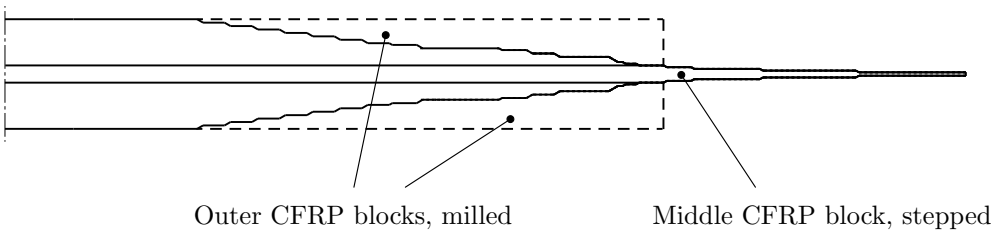

Figure 1.4.: Cross section generated by the initial manufacturing method.

The first CFRP disks were designed in three parts. The middle block had a cross section with a variable thickness, which was achieved by a stepping in the laminate. The outer blocks were manufactured with a constant thickness and glued onto the middle block. Afterwards, the cross section was milled into these outer parts. The absorber material was only applied onto the middle block. With this method, it was possible to thicken the disk around the cut-outs. Over time, there proved to be a strength reduction in the laminate due to micro cracks caused by the milling process.

1.4. Problem statement

CFRP disks show a particular vibration behavior at high speed rotation. This leads to a stagnation of the operational speed at around 350 Hz. For an increase in rotational speeds, a detailed knowledge of the physics of high speed rotating CFRP disks is necessary, which will allow for the application of optimization methods. In this research, various methods of structural analysis and numerical design optimization are applied to CFRP disks.

In the past, CFRP disks, rotating at a very high speed, were designed in a strength driven process. With an increase in operational speed as well as in diameters and cut-out depth, structural dynamics are beginning to be of greater importance. Such disks will, however, not meet the requirement of a first natural frequency being above the rotational frequency. The design optimization applied in this research will take into account the stiffening of the disk due to centrifugal forces during operation as well as the influence of the stepping of the laminate onto the natural frequencies. Furthermore, manufacturing constraints, the strength of the disk and the contact behavior between disk and hub will be considered.

Starting with a detailed structural analysis of existing CFRP disks, an enhanced design will be created, using numerical design optimization methods. This process will be executed on a specific disk with demanding requirements regarding the diameter of the disk, the operational speed and the size of the cut-outs. Finally, the advantage of the applied optimization methods will be validated with multiple experimental tests and measurements of the new disk design.

1.5. Overview of chapters

In chapter 1, a short introduction into the topic of this thesis is given. Some fields of application for CFRP disks are named, especially the neutron research area with chopper disks for TOF experiments. Furthermore, a retrospect of the design of CFRP disks is given, to be followed by the problem statement.

In chapter 2, multiple examples of high-speed rotating CFRP disks are given. Three different TOF experiments with their individual CFRP disks are introduced as well as the flywheels for energy storage.

In chapter 3, the mathematical essentials of the design method used in this thesis are given. The finite element method with a focus on CFRP is described. The particularities of such CFRP laminates in the context of rotating disks are described in detail. Further on, the numerical optimization algorithms used in the multidisciplinary design optimization of the disks are introduced.

In chapter 4, the fundamentals of rotordynamics are described analytically. The influencing factors of rotordynamics on the design of the disks are highlighted.

In chapter 5, a profound analysis of existing CFRP disks is given. The numerical methods from chapter 3 are applied. Moreover, a nonlinear contact analysis of the connection between the disk and the hub is performed.

In chapter 6, a novel holistic design optimization process for CFRP disks rotating at a very high speed is introduced. The complete design optimization process consisting of an increase in structural dynamical performance of the disk and a decrease of the stress peaks in the laminate is presented in detail. Furthermore, a comparison to analytical calculations is given.

In chapter 7, experimental tests of CFRP disks are described. The natural frequencies as well as the strength of the disks are measured and the results are discussed.

In chapter 8, the results of the structural analysis are compared to the results of the experimental measurement. The correlation of the values is discussed in detail.

In chapter 9, the results of this thesis are discussed and a conclusion and a summary are given.

2

Application examples of CFRP disks

This chapter depicts some examples of usage of CFRP disks. A major application is neutron research where so-called chopper disks are used. Other than that, disks rotating at a very high speed are used in many different applications like for example energy storage systems or turbines. This chapter gives an overview of the application of the CFRP disks with a focus on chopper disks applied in neutron research.

Contents

2.1. Overview of different application areas

High-speed rotating CFRP disks are used in different ways of application. For example, in the field of energy storage they are used as so-called flywheels. The size and the mass of these flywheels varies from miniature applications in mobile devices such as gyroscopes up to very large machines in power plants. Accelerating the flywheel induces energy into the system, and with a deceleration of the rotor, energy is gained from the system. The specific use of flywheels with CFRP disks is discussed in this chapter in section 2.3. Another field of application is the neutron research, where so-called chopper disks are used to adjust the speed of the neutrons in the neutron beam. Compared to the flywheels, chopper disks are relatively thin and reach tip speeds of up to $1\,000\,{}^{m}/_{s}$. Most of the CFRP disks which are described, analyzed, optimized and experimentally tested in this thesis are chopper disks. Some application examples are presented in the following section 2.2.

2.2. Chopper disks in neutron research

In 1932, James Chadwick first discovers the neutron. Only a few years later, scientists observe that neutrons can be diffracted by crystalline matter. The neutron scattering methods have steadily improved since the 1930s and nowadays a range of various high-performance methods is available, presenting detailed information about the properties and the behavior of almost all kinds of materials. Neutron research is conducive to fields of research such as biology, chemistry, materials science, particle physics and many more [27, 54, 55, 64, 71, 82, 124].

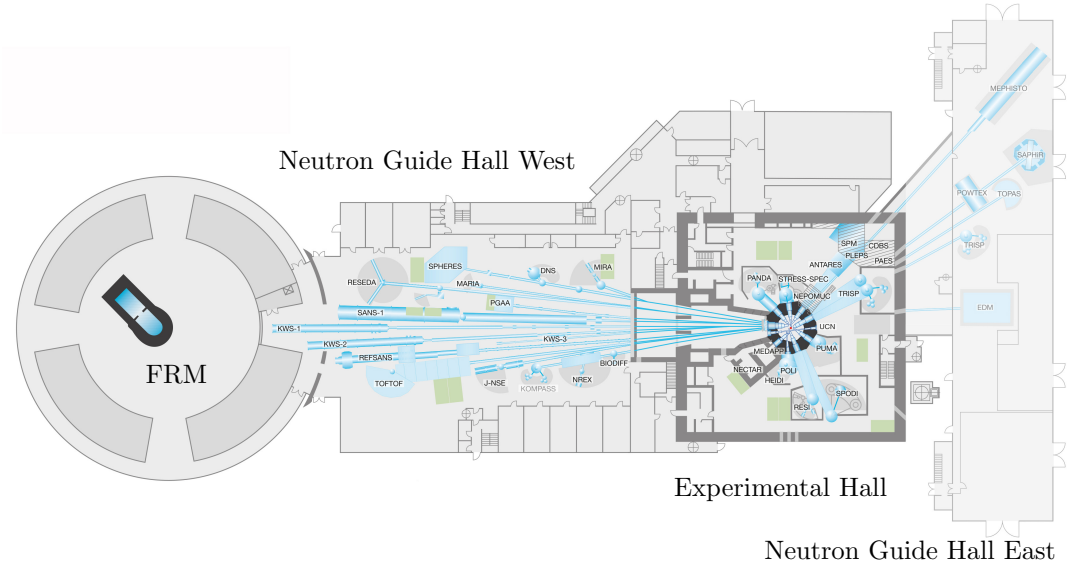

Figure 2.1.: Neutron Source Instruments at the MLZ in Garching [64].

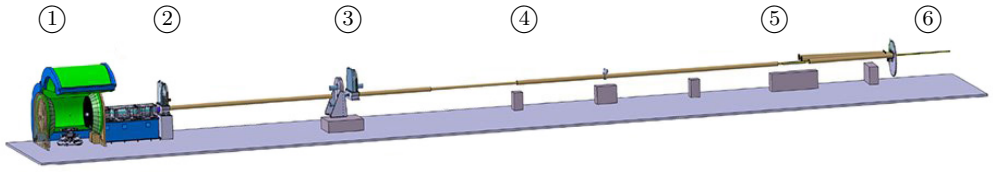

① Sample and detector
② Band-chopper disk
③ Overlap chopper disk
④ Safety shutter
⑤ Intrument shutter
⑥ Neutron guide

Figure 2.2.: Schematic Setup of POWTEX Project at the MLZ [64].

Many different neutron experiments, which are shown in figure 2.1, have been carried out at the Heinz Maier-Leibnitz Zentrum (MLZ) in Garching, which is near Munich in Germany. The neutron source, called the Forschungsreaktor München II (FRM II), is placed in the experimental hall and provides the radially arranged instruments with a neutron beam. The FRM II is the most powerful neutron source in Germany and offers worldwide the widest spectrum of neutrons ranging from ultra cold neutrons up to the fast neutrons from the converter facility [64, 139].

Figure 2.2 shows a typical setup of an instrument at the MLZ. The neutron beam is led from the neutron source through a neutron guide to the pulse chopper disk and afterwards through a second neutron guide to the sample and the detector. As every instrument has its individual setup, there are many different instruments arranged in the hall of the MLZ, which can be seen in figure 2.1 and in photograph 2.3 [132, 133, 136, 138, 149, 154].

Figure 2.3.: Photograph of the Experimental Hall of the MLZ [64].

2.2.1. Cold neutron time-of-flight spectrometer

The so-called TOFTOF chopper disk system is a cold neutron time-of-flight (TOF) spectrometer located at the neutron source FRM II at MLZ in Garching. The TOFTOF spectrometer can be used for quasi-elastic and inelastic neutron scattering. The spectrometer comprises seven chopper disks rotating at a high speed. The disks both monochromatise and pulse the neutron beam. Figure 2.4 shows a sketch of the TOFTOF system. The disks

operate at a rotational speed of 366.66 Hz and have a diameter of 600 mm. The weight of each disk is approximately 6.3 kg. The CFRP design of the TOFTOF chopper disks consists of two parts: The layers from the outer diameter up to the diameter of the bottom of the cut-outs are put in a stepped way into the mould. The second part of the layers from the diameter of the bottom of the cut-outs to the central through-hole is built with a constant diameter of the layers and milled after the curing and demolding. A sketch of this scheme is shown in figure 1.4. This kind of design was developed by the LLB in 2003 [101]. An advantage of this design is a continuous change of the thickness of the disk. This leads to a solution best fitting for a constant stress disk profile, described by Vullo et al [137]. As a material, M40J carbon prepreg is used. This material has a relatively high stiffness and a medium strength. The material parameters are listed in table 2.1.

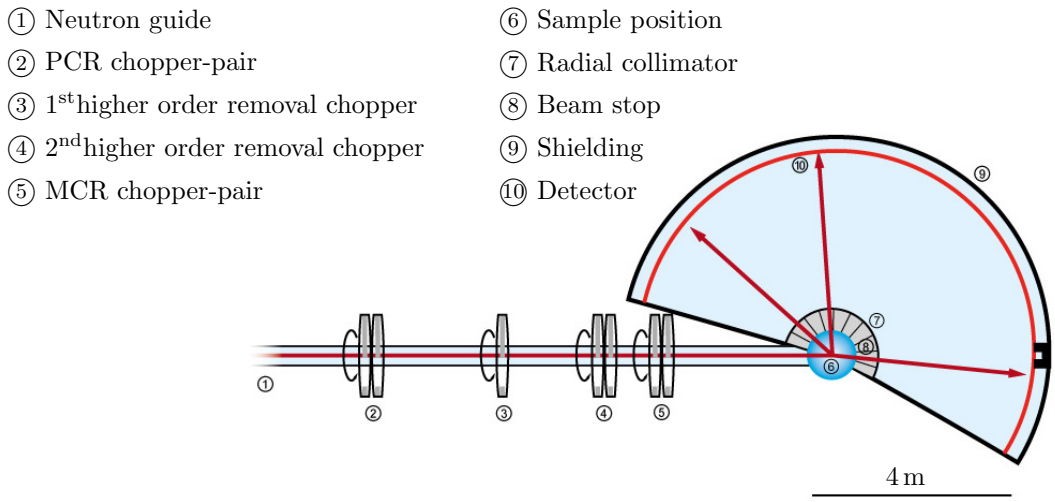

Figure 2.4.: Sketch of the TOFTOF System at FRM II [65].

Table 2.1.: Material properties of M40J with epoxy M18 resin at $V_f = 60\,\%$ [4].

$E_\parallel$ [MPa]	$E_\perp$ [MPa]	$G_{\parallel\perp}$ [MPa]	$R_\parallel^-$ [MPa]	$R_\perp^-$ [MPa]	$R_{\parallel\perp}$ [MPa]	$R_\parallel^+$ [MPa]	R_{ILSS} [MPa]
220 000	7 970	4 971	2 475	50	81	1 130	88

2.2.2. Time-of-flight spectrometer for short pulses and high neutron flux

The so-called "NEAT" chopper disk system is located at the neutron source Helmholtz Zentrum Berlin (BER II) [56]. The first chopper disk of the system comprising seven disks, subdivides the neutron beam into discreet packets of neutrons. At the second chopper disk, neutrons in this discreet packet that have the wrong speed are obstructed. The rotational speed during operation is planned to be 333.33 Hz. The outer diameter of the disks is 700 mm. The cut-outs are relatively large, compared to other chopper disks, and have a maximum opening angle of 34 ° and a maximum depth of 135 mm. The combination of a very high rotational speed and large cut-outs leads to different structural and dynamical problems, which are described in detail later on in this dissertation in chapter 5. A sketch of the NEAT chopper disk system with its seven disks is shown in figure 1.1. The dimensions of the CFRP disks of the NEAT project are used in multiple calculations in this thesis. The overspeed spin test in chapter 7 as well as the experimental measurement of the natural frequencies are conducted with a prototype disk of the NEAT project.

2.2.3. High-intensity time-of-flight diffractometer

The neutron spectrometer POWTEX is a high-intensity time-of-flight diffractometer and is designed by RWTH Aachen University and Forschungszentrum Jülich. The chopper disk system of the POWTEX is designed and produced by LLB. POWTEX is an abbreviation for POWder and TEXture, as the system will be used in solid-state chemistry, geoscience and materials science [64].

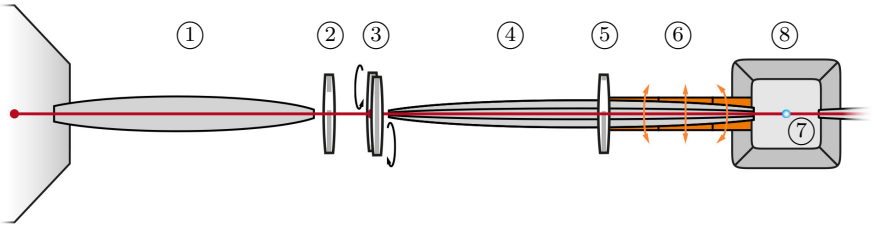

① Neutron guide
② Overlap chopper
③ Double-disk pulse chopper
④ Neutron guide
⑤ Bandwith chopper
⑥ Guide changer
⑦ Sample ≤ 1 cm^3
⑧ Detector

Figure 2.5.: Sketch of the POWTEX System at FRM II [64].

Several new concepts are combined in the instrument design: The neutron guide has a focal point of $10 \cdot 10\,\mathrm{mm}^2$ in the plain of the counter-rotating pulse chopper disks. This is a relatively small area compared to other chopper disk systems such as NEAT or TOFTOF. This small focal point leads to an optimized time resolution and reduces the background of the source. Aiming a sharp pulse of neutrons, two counter-rotating pulse chopper disks are used [149]. These disks operate at a rotational speed of 200 Hz and are placed at a distance of 5 mm to each other in the plain of the focal point of the neutron beam. In figure 2.5, the pulse chopper disks are labeled with ③. Both, the short distance between the disks and the virtual rotational speed of 400 Hz of the counter-rotating pulse choppers lead to a pulse of $10\,\mu$s. The disks have a diameter of 750 mm, which is the largest diameter of a CFRP chopper disk ever designed by LLB.

2.3. Flywheels for energy storage systems

A specific possibility of energy storage systems (ESS) is the flywheel energy storage system (FESS) [22, 89]. A flywheel is a mechanical application which is designed to store rotational energy. The amount of energy stored in a flywheel is linear proportional to its mass and is proportional to the square of its rotational speed. The mass of a flywheel is constant during operation. In order to increase the stored energy, the flywheel gets accelerated to a higher rotational speed. A general review of flywheels is given by Arani in "Review of Flywheel Energy Storage Systems structures and applications in power systems and microgrids" [12] and by Mousavi in "A comprehensive review of Flywheel Energy Storage System technology" [89]. Arani and Mousavi present the field of application such as FESS in electrical vehicles, railways or wind power systems. Furthermore, they describe different variants of rotors, generators and bearing systems such as permanent magnetic bearings and active magnetic bearings.

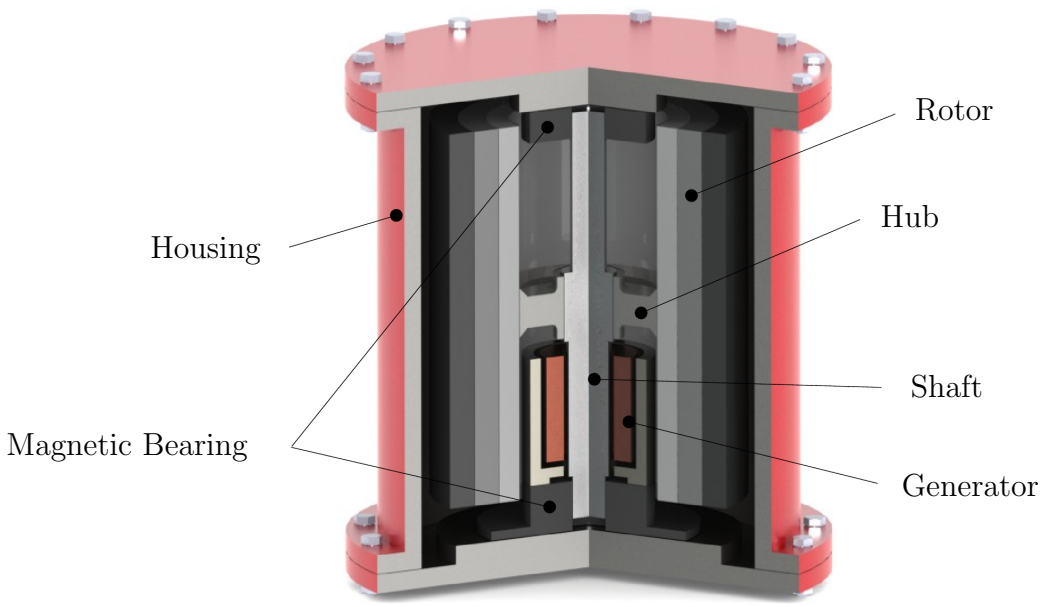

Figure 2.6.: Sketch of a flywheel [95].

The rotors of a FESS are standardly made of steel. The high density of the steel leads to a high mass of the rotors and thus to a high rotational energy. Compared to other materials, a flywheel made of steel is relatively cost effective. Such flywheels rotate on conventional bearings which are limited to low maximum rotational speeds [12, 26, 84].

Flywheels with a high energy density are designed of CFRP and have magnetic bearings, which leads to maximum possible rotational speeds of 1 000 Hz [31]. In figure 2.6, the sketch of a flywheel is shown. It consists of the following components [13, 22, 46, 79]:

- Rotor, which stores the rotational energy.
- Hub, which connects the rotor to the shaft.
- Shaft, which connects the flywheel to the bearings and the generator.
- Generator, which accelerates and decelerates the flywheel.
- Housing, which enables the vacuum.
- Magnetic bearings, which allow for high rotational speeds.

The limiting factor of standard flywheels is the strength of the steel. New applications with rotors made of CFRP or of composite hybrids allow for a higher energy density due to the higher specific strength of CFRP compared to steel [77, 78]. Krack and Mertiny discuss in "Cost optimization of hybrid composite flywheel rotors for energy storage" the advantage of rotors which are designed with a composite hybrid of glass fiber reinforced plastic (GFRP) and CFRP over those made of steel.

In contrast to most of the chopper disks used in neutron research, flywheels are predestined to be manufactured with filament winding. The dimensions of flywheels show a wide variety. The rotors can be designed to be relatively thick, as shown in the sketch of figure 2.6. The construction is compact due to the uniform dimensions in diameter and hight. Another possibility of the design of flywheels is a relatively thin disk which is able to rotate at a higher speed than the previous variant. For this design, a material with a higher specific strength is needed, for example CFRP or carbon fiber reinforced carbon (CFRC) [130, 131]. Hiroshima presents in "Spin test of three-dimensional composite rotor for flywheel energy storage system" a CFRP flywheel rotor with a diameter of 306 mm which is tested with a rotational speed of 833 Hz [67]. This equals a tip speed of 800 $^{m}/_{s}$. This is comparable to CFRP chopper disks, which reach maximum tip speeds of 900 $^{m}/_{s}$.

3

Fundamentals of modeling and simulation methods of disk systems

This chapter deals with the fundamentals of the structural analysis used in this thesis. For the calculations of CFRP, analytical approaches are often not applicable. Especially for disks with cut-outs or even unsymmetrical cut-outs, the finite element method (FEM) is a suitable approach. This chapter gives an introduction to the methods employed in this thesis followed by a description of the contact modeling applied. Finally, a numerical optimization approach is presented, which is used in the design process in chapter 6.

Contents

3.1. Requirements for modeling and simulation of disks

The description of the physics of the CFRP disks treated in this dissertation requires various computation methods. The geometry of the disks with their large cut-outs is too complex for an analytical calculation of the stress distribution during rotation. The loads affecting the disks arise on the one hand from the high centrifugal forces caused by high rotational speeds of up to 500 Hz, and on the other hand from the vibrations caused by the disk passing through its natural frequencies. The oscillation amplitudes of the disk lead to a shift of the application points of the centrifugal force and therefore to a more complex and nonlinear system behavior. Hence, the FEM is chosen for the structural analysis of the disks. With this method, the strain and stress distribution as well as the vibration behavior during rotation are computed. A brief introduction into the FEM is given in this chapter in section 3.2.

Furthermore, the connection behavior between the CFRP disk and the aluminum hub is researched in detail. The complexity of this connection behavior lies in the fact that during rotation the CFRP disk widens itself more than does the hub. Hence, in order to solve these boundary problems, nonlinear computation methods are used, which are presented in section 3.3.

A new approach of designing CFRP disks is presented in chapter 6. In the past, the design was enhanced empirically. With the knowledge gained from the detailed structural analysis in chapter 5, the disks are designed with numerical optimization methods, which are briefly introduced in this chapter in section 3.4.

3.2. Finite element method

This section describes the particularities of fiber-reinforced plastic in FEM calculations and their effect on structural dynamics. Due to the complexity of the laminate stepping and the geometrical dimensions of CFRP disks with cut-outs, the FEM method is the most suitable one.

The FEM is a numerical approach to solving partial differential equations (PDE) with boundary conditions. With this technique, the domain of interest is divided into smaller finite elements. Hence, large and complex structures can be computed by a stepwise calculation of the elements. Approximating functions in finite elements are defined in terms of nodal values of the favored physical field. The initially continuous physical problem gets transformed into a discretized finite element problem, where the values of the nodes are unidentified.

3.2.1. Basics of the finite element method

This section gives a brief description of the finite element method which is used in this thesis. The finite element method (FEM), or sometimes called finite element analysis (FEA), is a computational technique which is used to solve boundary value problems. These boundary value problems are also called field problems. The field is the domain of interest, which in mechanical engineering most often represents a physical structure consisting of the continuum body Ω and the displacements $\mathbf{u_i}$ [129]. This results in a strain tensor ε. With the elasticity tensor $\boldsymbol{C}$ the following equation (3.1) can be gained, where a connection between the stress field $\sigma^{\mathbf{u}}$ and the displacement field $\mathbf{u_i}$ is given:

$$\sigma^{\mathbf{u}} = \boldsymbol{C}\varepsilon^{\mathbf{u}} \tag{3.1}$$

For a detailed description of the FEM and FEA in mechanical engineering and in the domain of structures see Neto et al. “Engineering Computation of Structures: The Finite Element Method” [90] and Blaauwendraad “Plates and FEM” [25].

3.2.2. Finite element modeling of a CFRP disk

There are different options for modeling a structure made of fiber-reinforced laminate. A comparison of three variants of mesh options of a disk is shown with figure 3.1. The left part a) shows a model with tetra volume elements, part b) shows a two-dimensional model

with shell elements and part c) shows a variant with layered three-dimensional volume elements [52, 102]. In the first variant (a), the structure is meshed with three-dimensional elements such as tetra elements, and the material data of a quasi-isotropic layup are used. This method allows for first assumptions of the deflection of the component under a given load, but a detailed failure prediction is not possible.

A more detailed option is a meshing with two-dimensional shell elements (b). For each element, the layup of the laminate can be defined and a stiffness matrix can be calculated. This option allows for a more precise consideration of the behavior of the single layers of the fiber reinforced laminate than does the first option. An in-plane failure such as fiber fraction or a matrix failure can be predicted with such a model.

For considering failures between two layers such as interlaminate shear stress (ILSS) failure, an even more detailed model is necessary (c). Therefore, every layer of the laminate is modeled with volume elements. These three-dimensional elements have orthotropic material parameters which depend on the fiber direction of the layer itself. Compared to the first two options, the layered model causes the most effort concerning the modeling and it is very cost-intensive concerning computational time.

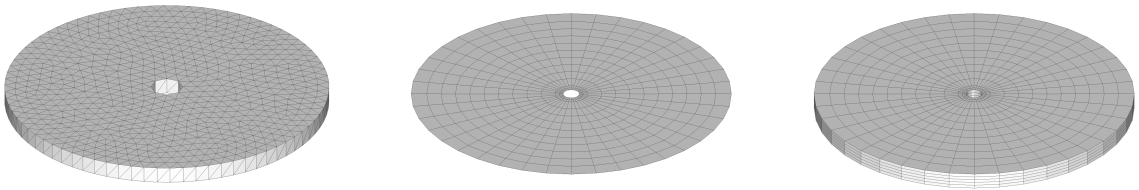

a) b) c)

Figure 3.1.: Comparison of three different mesh variants of a disk.

3.2.3. Anisotropy of bending stiffness of fiber-reinforced disks

Due to their rotationally symmetrical shape and the presence of the cut-outs, CFRP disks are usually manufactured with a quasi-isotropic layup. The polar diagram of the in-plane Young's Modulus of a UD lamina is shown in figure 3.2. Especially in the case of thin structures, though, their dynamic behavior is dictated by the choice of stacking sequence, which, however, does not affect their overall structural behavior [1]. An explanatory picture can be found in figure 3.4, where the values of the D_{11} of the ABD-Matrix, representing the bending stiffness in the local coordinate system, are plotted against the laminate global coordinate system.The stacking sequence of the layup of the $[0/45/90/\text{-}45]_s$ laminate is

shown in figure 3.3. The stacking of the layers starts from the top of the laminate with a 0° layer parallel to the x-direction of the global coordinate system.

The plot in figure 3.4 shows that the bending stiffness has its maximum in the area around 170° and its minimum around 65°. This becomes more evident with a minimum possible amount of layers and becomes less important for a number of layers higher than 128. It is remarkable that even a laminate with 16 layers and a quasi-isotropic layup of $[0/45/90/\text{-}45]_{2s}$ shows a difference in bending stiffness of factor 2.

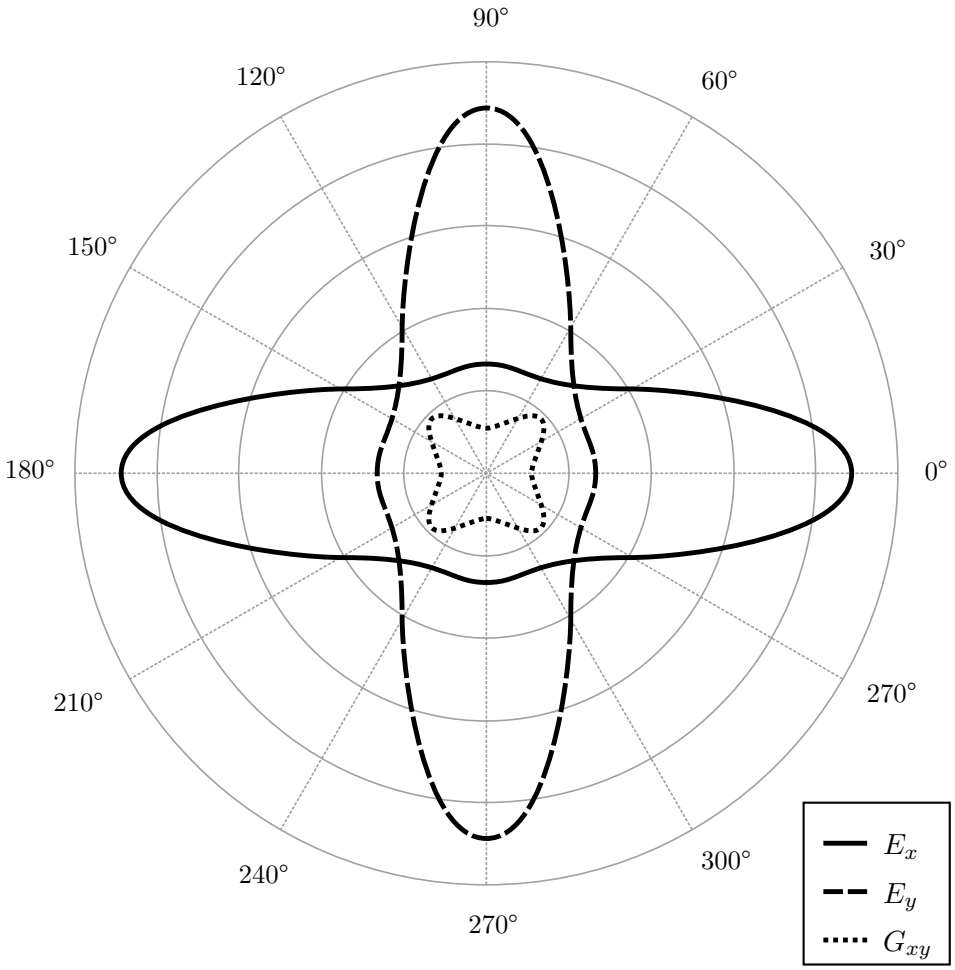

Figure 3.2.: Polar diagram of Young's modulus of a UD lamina.

The anisotropy of the material can also be observed in the shape of the natural frequencies, as shown in figure 3.5. Here, the difference of the shape of the eigenmode modeled either as a layered quasi-isotropic material (left) or as a quasi-isotropic homogenized material, the shape will be completely symmetric. Due to the anisotropy in bending stiffness

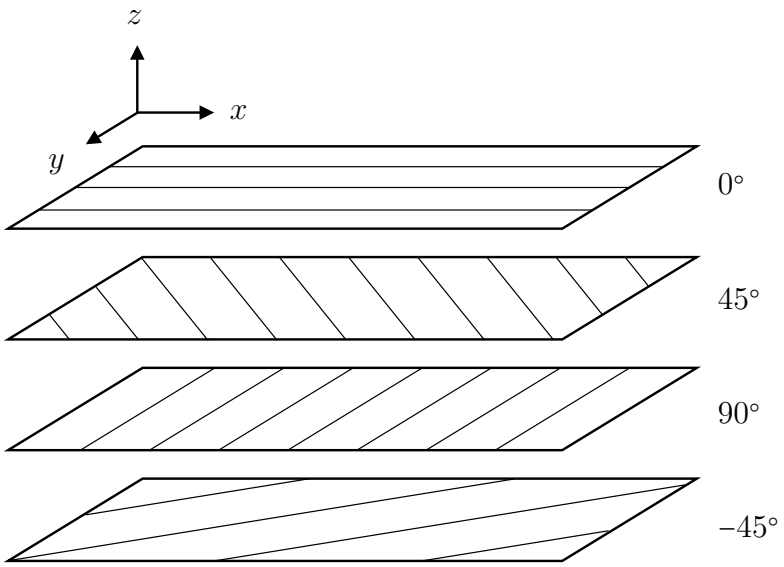

Figure 3.3.: Stacking sequence of the [0/45/90/-45] laminate.

this is not the case if a layered inhomogeneous material is used. The quasi-isotropic homogenized version shows the classical "umbrella eigenmode": the disk oscillates radially around its complete outer edge. In the case of a layered model, the disk oscillates around the x- and y-axis inversely, which can be seen as a "stingray eigenmode". The oscillation axes of the layered quasi-isotropic disk are turned by 65° compared to the global coordinate system. This corresponds to the direction of the minimum bending stiffness of the laminate, as shown in figure 3.4 [139].

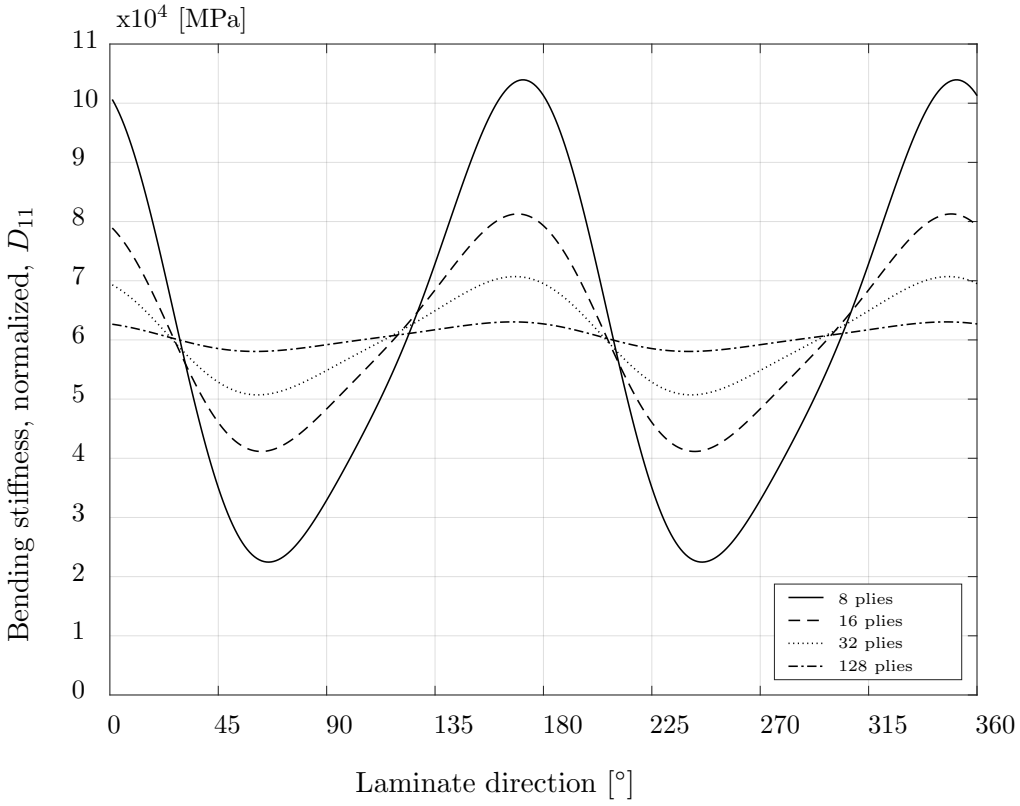

Figure 3.4.: Normalized bending stiffness D_{11} of the M30SC laminate with quasi-isotropic layup $[0/45/90/\text{-}45]_s$.

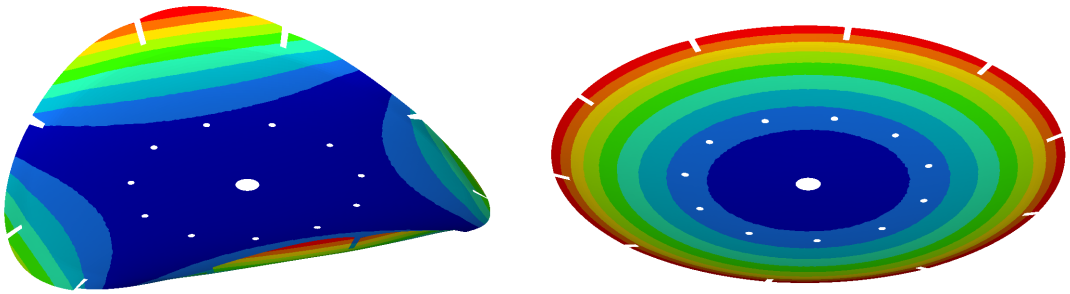

Figure 3.5.: Third eigenmode of a CFRP disk, left modeled with a layered quasi-isotropic laminate ("stingray eigenmode"), right modeled with an isotropic material ("umbrella eigenmode").

3.3. Contact analysis of disk-hub connections

In order to describe the detachment process of the disk from the hub and the contact status of the shaft-hub connection, finite-element simulations are conducted. Such a connection occurs between the CFRP disks and the hub as well as between the hub and the shaft of the disk systems dealt with in this thesis. The connection between the disk and the hub is tested experimentally in section 7.2.1. The fundamentals needed for the calculation of the connection are presented in the following subsections.

At the beginning of an analysis, the most important criteria is the decision whether a model has to be calculated using linear or nonlinear solution approaches. The analysis in section 5.1 is based on a linear assumption. In contrast, contact analysis in structural mechanics uses nonlinear boundary conditions that need to be solved using nonlinear solution approaches. The linear and nonlinear assumptions are compared in the following subsections based on Launhardt "Numerical Contact Simulation of the Shaft-Hub Joint-Connection of CFRP Chopper Disks" [80].

3.3.1. Linear analysis

The following assumptions are made in the linear finite-element theory:

- Displacements are small, as a rule of thumb below 5 % of the dimensions of the structure.
- Strain is linear proportional to stress, and the Hookean material model $\sigma = E \cdot \varepsilon$ is applied, neglecting plasticity.
- Loads are conservative and independent of displacements and temperature.
- Throughout the complete calculation, boundary conditions remain constant.

In the linear analysis, a set of equations is solved as shown in equation 3.2:

$$\boldsymbol{K_{const}} \cdot \boldsymbol{U} = \mathbf{F}_l \tag{3.2}$$

In equation (3.2), $\boldsymbol{K_{const}}$ is the constant stiffness matrix of the structure, $\boldsymbol{U}$ the nodal displacement and $\mathbf{F}_l$ the linear nodal force vector. In this case, the loads which are applied to the structure, are proportional to the displacements. Linear problems sets are proportional and reversible, which leads to relatively short computation times. Additionally,

load cases can be superposed to save computational effort [106]. Linear analysis is used for the optimization of the CFRP disks in chapter 6 in this thesis as the requirements listed above have been satisfied. Nevertheless, the oscillation amplitudes of the disk can lead to a shift of the application points of the centrifugal force and therefore to a nonlinear system behavior. Disks are operated at speeds which are far beyond natural frequencies. Hence, the vibration level is low and in a first approach, the non-linearity can be neglected.

3.3.2. Nonlinear analysis

Nonlinear analysis takes into account that for many applications these simplifications are not valid. For example, geometry changes, nonlinear material behavior or contact phenomena lead to a new set of equations:

$$\boldsymbol{K}(\boldsymbol{U}) \cdot \boldsymbol{U} = \mathbf{F}_{nl} \tag{3.3}$$

In equation (3.3), the nonlinear stiffness matrix $\boldsymbol{K}(\boldsymbol{U})$ depends on the nodal displacement $\boldsymbol{U}$ while $\mathbf{F}_{nl}$ represents the nonlinear nodal force vector. These nonlinear equations cannot be solved with the same algorithms as linear ones. Different, usually more complex, solution methods need to be applied that take into account different types of nonlinearity [80]. There are three different nonlinearities mentioned in literature: Geometric nonlinearity, boundary nonlinearity and material nonlinearity. The first two variants are briefly described in the following subsections, as they occur on the disks mentioned in this thesis.

3.3.2.1. Geometric nonlinearity

Geometric nonlinearity is caused by large deformations. As a rule of thumb, displacements of up to 5 % from the original dimensions can be treated as small or infinitesimal and therefore may be solved under the assumption of small displacements. For rotations, a maximum angle of 5 degrees is recommended when using linear solvers. Changes in the geometry during simulation might also have significant influence on the behavior of the system. The moment of inertia changes under deformation, for example a formerly stiff cross section might become unstable during loading. A typical example of geometric nonlinearities are buckling phenomena where new equilibrium equations need to be solved for large deflections. With regard to the CFRP disks, the shift of the application points of the centrifugal force caused by the vibration amplitudes can lead to a geometric nonlinearity.

In contrast to the linear equation, the general nonlinear equation (3.3) must therefore be recalculated after a certain amount of displacement or deformation, in order to adequately correspond to the new behavior of the system. The frequency of the adaption can be selected in the FEM tools [80].

3.3.2.2. Boundary nonlinearity and contact

The displacement boundary conditions are used in chapter 5.2.1. Here, the connections between the disk and the hub at various loads are calculated with a numerical software tool. Literature differentiates between two types of boundary condition: traction boundary condition and displacement boundary condition. The traction boundary condition is also called force boundary condition [72, 80]. For example, a traction boundary condition nonlinearity occurs in systems with fluid pressure. Traction boundary is described with equation 3.4. Here, $\mathbf{F}_{nl}$ represents the external nodal force vector and $\mathbf{u}$ represents the nodal displacement.

$$\bar{\mathbf{F}}_{nl} = \bar{\mathbf{F}}(\mathbf{u}) \tag{3.4}$$

Displacement boundary conditions depend on the deformation itself and require nonlinear approaches that satisfy equation 3.5. Here, $\bar{\mathbf{u}}$ represents the displacement boundary condition and $\mathbf{u}$ the unknown nodal displacement.

$$\mathbf{u}(x) = \bar{\mathbf{u}}(x) \tag{3.5}$$

3.3.3. Numerical contact modeling in finite element analysis

While the basics of contact between structures and the different causes of non-linearity have already been presented, their numerical integration into finite-element solvers is going to be discussed now. Several approaches and theories concerning contact treatment exist and in the following subsections a standard set-up is presented.

3.3.3.1. Master-slave contact detection algorithm

In principal, contacts in most finite element solvers are computed either between sets of surfaces or sets of slave nodes and master surfaces. Areas where contacts occur are defined as contact surfaces in the preprocessor. Here, surface elements are selected on each part.

One surface is defined as the master segment and the other one as the slave segment. Depending on whether a surface to surface (S2S) or surface to node (S2N) approach has been selected, the solver automatically extracts the corresponding boundary nodes and element faces [152].

For each slave node a master surface must be found via the closest point approach where the closest point ϱ^* on a master surface Γ_m from a slave node η_s is defined by:

$$\varrho^* \in \Gamma_m : \forall\, \varrho \in \Gamma_m,\ |\eta_s - \varrho^*| \leq |\eta_s - \varrho| \tag{3.6}$$

During the calculation, the penetration of slave nodes into the master surface is checked and prevented either by adding stiffness through spring elements to the part or by solving additional nonlinear contact equations. A shortcoming of this method is the need to specify the contact area a priori. This is not always possible, especially in highly dynamic, multiple body systems. With CFRP disks, however, the contact area can be defined precisely a priori. For the most computation shown in chapter 5.2.1, an S2S modeling is chosen. The inner area of the CFRP disk represents the master surface and the outer area of the hub represents the slave surface.

3.3.3.2. Contact discretization

After determining the geometry of the contact, an appropriate interface type is selected, depending on the solver, the goal of the analysis and the known or anticipated behavior of the system. The interface type can be either a node to node or node to surface discretization variant.

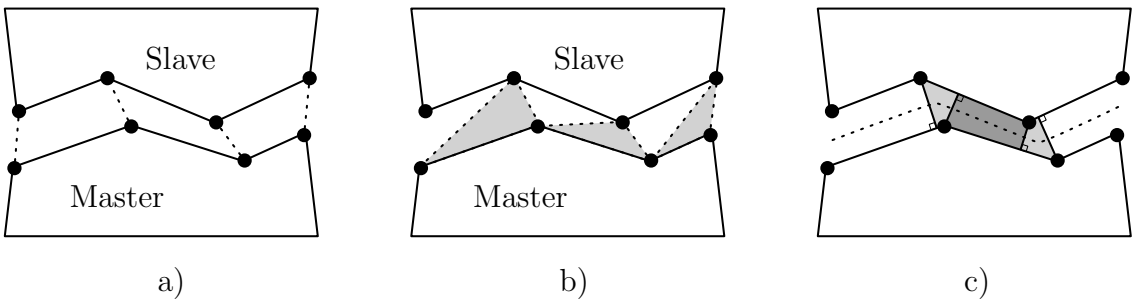

Figure 3.6.: Variants of the contact discretization, a) Node to node, b) Node to surface, c) Surface to surface.

In the node to node method, master and slave nodes are connected with each other. In the node to surface method, slave nodes are aligned over surface edges of the master surface. Another approach is given by the surface to surface method, which offers the possibility to resolve large deformations and higher order shape functions. The three sketches in figure 3.6 show the schematic representation of each resolution method.

If closed contact surfaces are detected, reaction forces are applied to the contact nodes in order to prevent penetration through each other. Nodes not in contact are discarded from the analysis and not included in the contact treatment.

3.4. Numerical optimization

A new approach of designing CFRP disks is presented in this dissertation in chapter 6. In the past, the design was enhanced empirically. With the knowledge gained from the detailed structural analysis in chapter 5, the disks are designed with numerical optimization methods, which are briefly introduced in this section.

3.4.1. Optimal design task

Optimization is a process in order to find a better or even the best solution for a design problem. The design has to be described mathematically by system equations and design variables. The aim of the optimization is given with the objective functions, and the constraints are described by the boundaries in which the system can be optimized [16, 17, 18, 28, 61, 86, 108, 114, 125]. In chapter 6 of this thesis, multiple numerical design optimizations are conducted in order to increase the performance of CFRP disks. In this section, the theoretical basics of numerical optimization are presented. Built on these essentials, the design optimization is performed in chapter 6. A general optimization formulation is given in equation (3.7), where $\mathbf{x}$ represents the vector of design variables, $z(\mathbf{x})$ is the objective function, $\mathbf{g}(\mathbf{x})$ is the vector of the inequality constraint functions and $\mathbf{h}(\mathbf{x})$ is the vector of the equality constraint functions [18].

$$\begin{aligned} \min \quad & z(x_j) \\ \text{and} \quad & h_k(x_j) = 0 \\ \text{so that} \quad & g_l(x_j) \leq 0 \end{aligned} \tag{3.7}$$

with

x_j	...	Vector of design variables with	j	=	$1, \ldots, n_{DV}$
$z(x_j)$	...	Objective function			
$h_k(x_j)$	...	Vector of equality constraint functions with	k	=	$1, \ldots, n_{EC}$
$g_l(x_j)$	...	Vector of inequality constraint functions with	l	=	$1, \ldots, n_{IC}$

The objective function $z(\mathbf{x})$ is to be minimized to achieve the aim of the optimization statement within the boundaries of the fulfilled constraints.

In this dissertation, the design variables $\mathbf{x}$ are mostly the thicknesses of elements or zones of the disks. The objective function $z(\mathbf{x})$ varies between the natural frequencies of the disk, the radial widening of the central through-hole and the stress peaks at the

bottoms of the cut-outs. The equality constraints **h** are rarely used in this thesis, while the inequality constraints **g** comprise mass restrictions, failure indices and minimum natural frequencies.

3.4.2. Optimality conditions

For an optimization statement with constraints and the functions $z(\mathbf{x})$, $\mathbf{g}(\mathbf{x})$ and $\mathbf{h}(\mathbf{x})$ being twice continuous differentiable regarding x_i, the problem can be noted as a Lagrange function L with the Lagrange multipliers λ_j and η_k, as shown in the following equation (3.8) [85].

$$L(\mathbf{x}, \mathbf{g}, \mathbf{h}) = z(\mathbf{x}) + \lambda_j g_j(\mathbf{x}) + \eta_k h_k(\mathbf{x}) \tag{3.8}$$

The necessary condition, which has to be true for a combination of the Lagrange multipliers λ_j and η_k at an optimum value $\mathbf{x_{opt}}$, is the Karush-Kuhn-Tucker criteria. It includes the sum of all partial derivatives with regard to the design variables x. The constraints are multiplied with their Lagrange multiplier, as shown in the following equation (3.9).

$$\left.\frac{\partial z}{\partial x_i}\right|_{x_{opt}} + \sum_j \left.\frac{\partial g_j}{\partial x_i}\right|_{x_{opt}} \cdot \lambda_j + \sum_j \left.\frac{\partial h_k}{\partial x_i}\right|_{x_{opt}} \cdot \eta_k = 0 \tag{3.9}$$

In addition to the general constraint equations (3.10) and (3.11), the Lagrange multipliers for inequality constraints must not be negative. Additionally, every product of the multiplier with its constraint function must be zero, as shown in equation (3.12).

$$g_j(\mathbf{x}) \leq 0 \tag{3.10}$$

$$h_i(\mathbf{x}) = 0 \tag{3.11}$$

$$\lambda_j \geq 0 \tag{3.12}$$

$$g_j(\mathbf{x})\lambda_j = 0 \tag{3.13}$$

In equation (3.9), only those terms with $\lambda_j > 0$ are taken into consideration. In equation (3.13), this is only true for $g_j = 0$, which shows that the constraint is active. A further necessary condition has to be fulfilled, which is a positive definite Hessian matrix at the point for a local minimum, as shown in the following equation (3.14) [85, 125].

$$\mathbf{H}(L(\mathbf{x},\lambda,\eta)) = \frac{\partial^2 L}{\partial x_i \partial x_j}(\mathbf{x},\lambda,\eta); \quad \text{with } i,j = 1,...,n \text{ positive definite} \tag{3.14}$$

For a global minimum, the Hessian matrix has to be positive definite in the whole solution space, which correlates to the Lagrange function being convex [18].

3.4.3. Optimization process

The process of the optimization can be divided into several steps. A general optimization sequence is described in the following listing [18].

1. The optimization statement is formulated.
2. A starting vector $\mathbf{x}^{(k)}$ is defined $(k = 1)$.
3. A system analysis is conducted to obtain the system response.
4. The gradients of the system response are calculated.
5. The objective functions and the constraint functions as well as their gradients are evaluated.
6. The global and the local stopping criteria are checked for convergence. The admissibility and the feasibility of the design variable vector are checked. If the criteria are fulfilled, the optimization stops here.
7. If the stopping criteria are not fulfilled, a change vector $\Delta\mathbf{x}^{(k)}$ is calculated by the optimization algorithm with a search direction vector $\mathbf{s}^{(k)}$ and a step length $\alpha^{(k)}$. The search direction points towards lower values of the objective function.
8. The design variables vector for the next step is calculated: $\mathbf{x}^{(k+1)} = \mathbf{x}^{(k)} + \Delta\mathbf{x}^{(k)}$
9. Steps 3. to 8. are repeated until the stopping criteria are fulfilled and a solution has converged.

In figure 3.7, a two-dimensional example is shown with the design variables x_1 and x_2 on the two axes and lines for constant values of the objective function $z(\mathbf{x})$. The solution space is limited by the two constraints g_1 and g_2. The optimum solution is the lowest value of z, which does not violate the constraints. The search vector $\alpha \cdot \mathbf{s}$ goes from a solution $\mathbf{x}^{(k)}$ at step k to a better solution $\mathbf{x}^{(k+1)}$ at the next step [125].

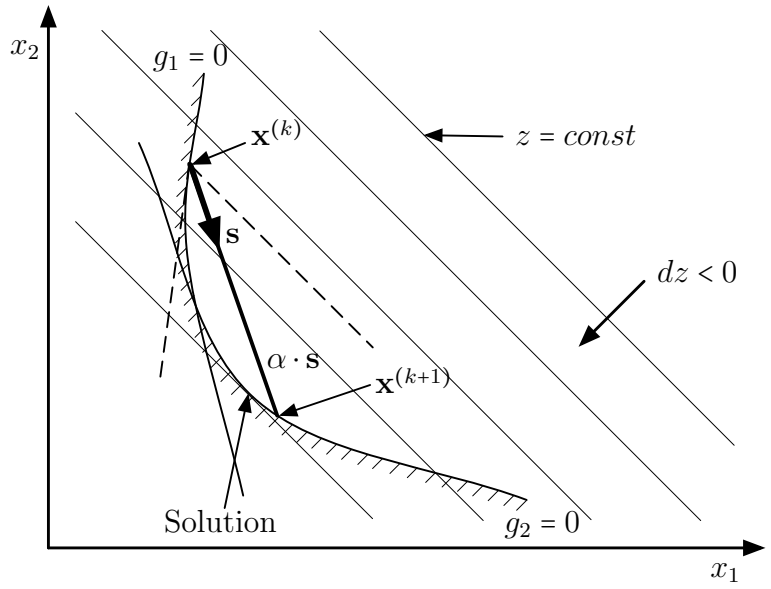

Figure 3.7.: Optimization step from k to $k+1$.

For practical application in mechanical engineering, there are different types of structural optimization, which are illustrated in figure 3.8 and listed below:

- Sizing Optimization: Geometric parameters (e.g. cross-section) that describe a structure are adjusted.
- Shape Optimization: The contours of a structure are adjusted by moving boundary nodes or curves that describe the shape. This can be used for example to minimize peak stresses of a structure.
- Topology Optimization: The material density inside a design space is adjusted, which results in an optimized material distribution for given boundary conditions.

As becomes apparent from figure 3.8, topology optimization is the most general optimization approach, influencing the overall topology, the shape of the surfaces and the size of the structure [23]. It is used in this dissertation in section 6.3.3, where a a new hub design is generated with a topology optimization with regard to a temperature load. Shape optimization is limited to a domain with a fixed topology, which means that no further boundaries, like holes, are created. Here, only the already existing boundaries are shifted. The shape optimization is applied to the cut-outs of CFRP disks treated in section 6.2.4. With topology optimization as a first step to creating a good boundary shape for a structure, shape optimization can be used as a second step for further optimization [23]. The sizing optimization is used for the adaption of the thickness of shell elements during

the design optimization of CFRP disk in section 6.2.2. Here, the outer dimensions of the disk as well as the dimensions of the cut-outs are predefined and only the thickness of the laminate is varied.

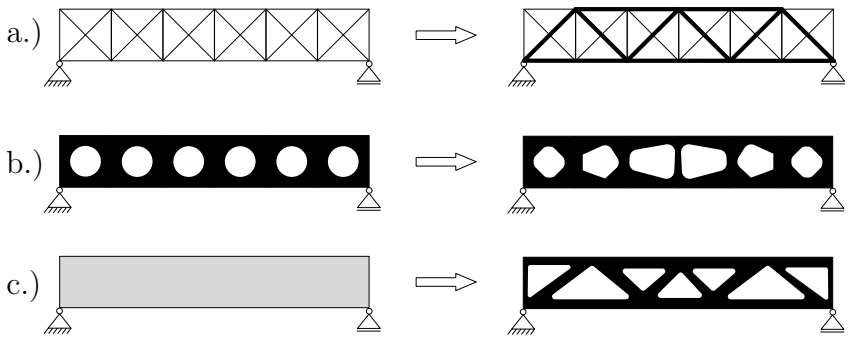

Figure 3.8.: Types of structural optimization, initial design on the left, optimized design on the right: a) sizing optimization, b) shape optimization and c) topology optimization.

3.4.4. Optimization algorithms

The numerical design optimizations of the disks presented in this dissertation are conducted with the software tool Altair Hyperworks Optistruct, which uses among others the method of feasible direction (MFD) algorithm [81, 92, 94]. The MFD is a gradient based deterministic algorithm. For detailed information on the algorithms used in the software tool see "OptiStruct User's Guide" [69].

To determine a solution, an optimization algorithm is used after the formulation of the optimization problem. There are the following types of methods [18, 85]:

- Enumerative: All possible combinations of design variables are analyzed to find a global optimum, which limits this method to very small problems with only one or two design variables.
- Deterministic: Gradient information is used to approach an optimum in a few steps. This optimum can be either local or global.
- Stochastic: The design variables are changed randomly, thus two optimization runs with the same start vector do not always lead to the same solution.
- Optimality Criteria Method: Physical properties of the optimization problem are used for a specific algorithm.

4

Rotordynamic principles of high-speed rotating disks

In this chapter, the criticality of dynamics is featured. First, the analytical equations for plates and disks are expressed and established. Subsequently, natural frequencies of disks and their critical triggering are taken into consideration. A profound understanding of rotordyamics is a basic requirement for the design of a disk which is meant to show stable behavior with regard to its structural dynamics. In this chapter, the influencing factors of the natural frequencies are described as well as the effect of rotation on natural frequencies.

Contents

4.1. Theoretical background of rotordynamics

In technical literature, there are numerous publications on the stiffness and the oscillations of circular plates, beginning with Kirchhoff in the 1880s up until the modern finite element method (FEM) researches in our days. In the following chapters, the most important technical literature, equations and basic approaches are presented and summarized [24, 53, 68, 93, 116, 120, 134].

4.1.1. Analytical basics of the calculation of vibration behavior

The most important plate equations are set up by Kirchhoff in 1882 [73] and are also known as the "Kirchhoff theory of plates". These equations are based on the Euler-Bernoulli beam theory. In 1922, Southwell publishes his thesis with the title "On the Free Transverse Vibrations of a Uniform Circular Disc Clamped at its Centre; and on the Effects of Rotation" [119]. He continues the equations set up by Kirchhoff, which are formed generally for plates, and adapts them for circular disks, using the results achieved by Mindlin for thicker plates.

In 1929, Reißner researches on thin, circular plates and achieves semi-analytical results for the natural frequencies [105], while Dirr concentrates on the precise calculations of plate oscillation in a plain [42]. For large deformations of such a plate, Rückert makes assumptions in his thesis entitled "Kirchhoff plates and large deformation" [109, 110].

General equations for structural mechanics can be found in the works by Freymann [43] and Gasch [47, 48]. Both consider analytical as well as numerical calculations. Furthermore, Stephan goes into detail about disk and plate oscillations in his work "Schwingungen elastischer Kontinua" [122].

4.1.2. Equation of motion extended with gyroscopic effects

The equation of motion is given with the matrices of mass $\boldsymbol{M}$, of damping $\boldsymbol{D}$ and of stiffness $\boldsymbol{K}$. These matrices relate the response $\mathbf{x(t)}$ of the system to the external forces $\mathbf{f(t)}$ which are applied to the system. The general differential equation of motion is given with equation 4.1 [59]:

$$[\boldsymbol{M}]\{\ddot{\mathbf{x}}(\mathbf{t})\} + [\boldsymbol{D}]\{\dot{\mathbf{x}}(\mathbf{t})\} + [\boldsymbol{K}]\{\mathbf{x}(t)\} = \{\mathbf{f(t)}\} \tag{4.1}$$

For rotating structures, this equation of motion is extended by the gyroscopic matrix $\boldsymbol{G}$. $\boldsymbol{G}$ is the gyroscopic matrix of the vibration velocity and includes Coriolis elements and $\boldsymbol{N}$. Here, $\boldsymbol{N}$ is the gyroscopic matrix of elastic deflection and includes the centrifugal elements [76, 153]. This extended matrix in given with equation 4.2:

$$\begin{aligned}[\boldsymbol{M}]\cdot\{\ddot{\mathbf{x}}\}\boldsymbol{E}+[\boldsymbol{D}+\boldsymbol{G}]\cdot\{\dot{\mathbf{x}}\}\boldsymbol{E}+[\boldsymbol{K}+\boldsymbol{N}]\cdot\{\mathbf{x}\}\boldsymbol{E}=\\ =[\boldsymbol{M}]\cdot[\boldsymbol{V}]\cdot\{\ddot{\mathbf{s}}\}\boldsymbol{E}+[\boldsymbol{B}]\cdot[\boldsymbol{V}]\cdot\{\dot{\mathbf{s}}\}\boldsymbol{E}+\{\mathbf{p}\}\boldsymbol{E}\end{aligned} \tag{4.2}$$

with

$\boldsymbol{M}$	...	Mass matrix
$\boldsymbol{D}$	...	Damping matrix
$\boldsymbol{K}$	...	Stiffness matrix
$\boldsymbol{N}$	...	Gyroscopic matrix of elastic deflection including Coriolis elements
$\boldsymbol{B}$	...	Gyroscopic matrix of small foot point excitation
$\boldsymbol{V}$	...	Transposition matrix, which consists of distances between grid point and foot point
$\{\mathbf{x}\}\boldsymbol{E}$	...	Small grid point deflection, components measured relative to moving structure (non inertial)
$\{\mathbf{s}\}\boldsymbol{E}$	...	Small foot point or reference point excitation movement, components measured relative to an inertial point
$\{\mathbf{p}\}\boldsymbol{E}$	...	Variable external loads

For the computation and solving of rotating systems in numerical tools, these gyroscopic effects can be activated for example in the software tool ANSYS with the command `CORIOLIS, ON, --, --, RefFrame, RotDamp`. This is conducted in this thesis for the generation of different Campbell diagrams, which show the vibration behavior of a disk versus the rotational speed. For a more in-depth description of the implementation of the gyroscopic effects in the software tools, see ANSYS "Rotordynamic Analysis Guide" [70].

4.2. Analytical calculation of natural frequencies

It is possible to calculate the natural frequencies of plates analytically. To begin with, the plate equation, set up by Kirchhoff, has to be used to calculate the bending stiffness of a plate. This is demonstrated in the following subchapters.

4.2.1. Kirchhoff's plate equation

To calculate the bending stiffness of a plate, Kirchhoff makes the following assumptions for a plate:

- Constant thickness.
- Plane cross section.
- Small deflections.
- Homogeneous material.
- Rigidity over the thickness of the plate.

With these assumptions, Kirchhoff sets up his basic equation, also called Kirchhoff's plate equation, as shown in equation (4.3).

$$\left(\frac{1}{r}\frac{\partial}{\partial r} + \frac{\partial^2}{\partial r^2} + \frac{1}{r^2}\frac{\partial^2}{\varphi^2}\right)^2 \cdot w = \Delta\Delta w = \nabla^4 w = \frac{p}{N} \tag{4.3}$$

Equation (4.3) is set up for a polar coordinate system, which is suitable for circular plates such as saw disks or chopper disks. In equation 4.3, w is the deflection of the plate and $p = p(r, \varphi)$ is load per unit area with r as the radius and φ as the angular in the polar coordinate system. Δ is the Laplace operator, ∇ is the Nabla operator, and N represents the bending stiffness of the plate.

To calculate the bending stiffness N, as used in equation (4.3), the attempt made by Bernoulli has to be chosen. The result of the rearrangement is shown in equation (4.4).

$$N = \frac{E \cdot h^3}{12(1-\nu^2)} \tag{4.4}$$

In equation (4.4), E is Young's modulus, h is the thickness of the plate and ν is Poisson's ratio. The bending stiffness of the plate rises on a linear basis with Young's modulus and with the third power of the thickness.

4.2.2. Kirchhoff's plate oscillation

To calculate the natural frequencies of a plate, a differential equation has to be set up, based on equation (4.3):

$$\Delta\Delta w = \nabla^4 w = -\frac{\varrho \cdot h}{N} \cdot \frac{\partial^2 w}{\partial t^2} \tag{4.5}$$

In equation (4.5), the variable t is introduced for the time. The resolution of equation (4.5) is achieved through adaptation of Bessel's differential equation. The detailed solution can be read in the publication by Friebe [44], while the final function is shown in the following equation:

$$f_e = \underbrace{\frac{\left(\frac{d_i}{d_o}\right)^2 \cdot \lambda^2}{2 \cdot \sqrt{12(1-\nu^2)}}}_{\zeta} \cdot \frac{h}{\pi \cdot d^2} \cdot \sqrt{\frac{E}{\varrho}} \tag{4.6}$$

In equation (4.6), f_e is the natural frequency, d is the diameter with its limitations d_o for the outer diameter and d_i for the inner diameter. The first part of equation (4.6) can be summarized using the variable ζ, which is among others dependent on the empirical value of λ:

$$\zeta = f(d_i/d_o, \lambda, k, \nu) \tag{4.6a}$$

The variable λ again is dependent on the index of the eigenmode, represented by the variable k, and is set up semi-analytically and empirically. Southwell gives a table of values for different eigenmodes in his publication [119]. The variable ζ can be extracted from equation (4.6) and is here displayed in a short version:

$$f_e = \zeta \cdot \frac{h}{\pi \cdot d^2} \cdot \sqrt{\frac{E}{\varrho}} \tag{4.6b}$$

From equation (4.6b) it becomes apparent that the natural frequencies rise on a linear basis with the thickness of the disk and with the square root of Young's modulus, whereas they drop with the second power of the diameter and with the square root of the material density. This effect is validated with a CFRP disk in chapter 6.2.2.5.

4.2.3. Residual stress caused by the rotation of disks

Rowinski sets up an equation for the residual stress in radial direction in rotating disks, based on the assumptions of Timoshenko [107]:

$$\sigma_r = \omega^2 \cdot r_o^2 \cdot \frac{\varrho}{g} \cdot \frac{3+\nu}{8} \left[1 + \left(\frac{r_i}{r_o}\right)^2 - \left(\frac{r_i}{r}\right)^2 - \left(\frac{r}{r_o}\right)^2 \right] \tag{4.7}$$

In equation (4.7), σ_r is the stress in radial direction, r is the radius with its limitations r_o for the outer radius and r_i for the inner radius, and g is the acceleration of gravity. The variable ω represents the angular frequency of the disk. From equation (4.7) it becomes apparent that the residual stress rises with the second power of the angular frequency and the outer radius. The maximum residual stress in radial direction is on the inner radius.

4.2.4. Effect of rotation on natural frequencies

Southwell sets up the following approximation formula for the natural frequencies influenced by the residual stress caused by rotation:

$$f_{e\omega} = \sqrt{f_e^2 + \lambda\omega^2} \tag{4.8}$$

In equation (4.8), $f_{e\omega}$ is the natural frequency as a function of the angular frequency, composed of the natural frequency f_e of the non-rotating disk and of the stiffening part due to the centrifugal force. Equation (4.8) is an approximation formula based on the empirical variable λ, which leads to inaccurate values. Rowinski and Friebe measure $f_{e\omega}$ to get a verified value for the following equations.

4.3. Critical speeds of rotating disks

For the contemplation of the critical rotational speeds, Rowinski supposes a stationary reference system [107]. Derived from the equations for the harmonic oscillation, he sets up the following functions:

$$\omega_{e\omega} t - k\omega_n t \sim f_{e\omega} - k f_n = f_1 \tag{4.9}$$

$$\omega_{e\omega} t - k\omega_n t \sim f_{e\omega} + k f_n = f_2 \tag{4.10}$$

In equations (4.9) and (4.10), $\omega_{e\omega}$ is the angular frequency of the natural frequency $f_{e\omega}$, and ω_n is the angular speed of the disk while k represents the index of the eigenmode [50, 151].

4.3.1. Campbell diagrams

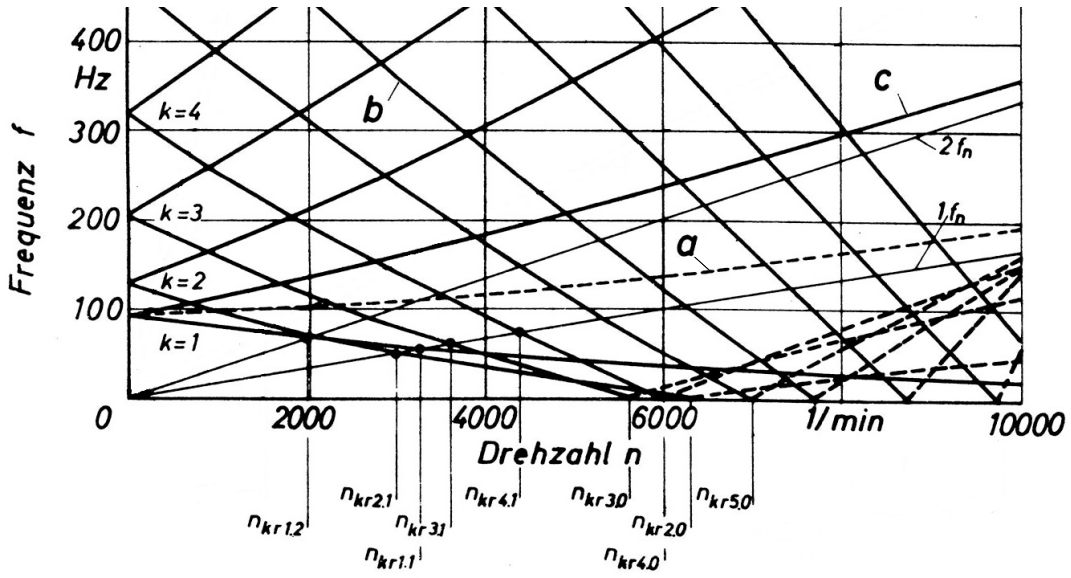

Figure 4.1.: Extract of a Campbell diagram [107].

In diagram 4.1, three graphs a, b and c are plotted. Graph a shows the natural frequency $f_{e\omega}$ versus the rotational speed of the disk. Graph b shows the frequency f_1 from equation (4.9) and graph c shows the frequency f_2 from equation (4.10). Graph a is only plotted for the nodal diameter k_1, graphs b and c are plotted for the nodal

diameters $k = 1, 2 \ldots 4$. It is possible to read out different critical rotational speeds from the diagram. The notation of the critical rotational speed is $n_{cr\,k.i}$, with k for the number of the eigenmode and i for the harmonic rotary frequency. There are different kinds of critical rotational speeds, which are summarized below:

- Critical rotational speed $n_{cr\,k.0}$ with oscillation caused by a constant parasitic force, e.g. $n_{cr4.0} = 6\,050\,\text{rpm}$ in diagram 4.1.
- Critical rotational speed $n_{cr\,k.1}$ with oscillation caused by a rotary frequency of the shaft, e.g. $n_{cr1.1} = 3\,500\,\text{rpm}$ in diagram 4.1.
- Critical rotational speed $n_{cr\,k.i}$ with oscillation caused by harmonics of the rotary frequency, e.g. $n_{cr\,1.2} = 2\,000\,\text{rpm}$ in diagram 4.1.
- Critical rotational speed with oscillation caused by a free, constant parasitic frequency, e.g. $f_{st} = 1\,050\,\text{Hz}$ at $n_{cr\,6.i} = 3\,750\,\text{rpm}$ in diagram 4.1.

The critical rotational speed can be directly calculated with the following equation:

$$n_{cr\,k.i} = f_e \cdot \frac{60}{\sqrt{(1 \pm k)^2 - \lambda}} \tag{4.11}$$

resp. transformed with f_e from equation (4.6b) directly from the geometric parameters of the disk:

$$n_{cr\,k.i} = \frac{\zeta h}{\pi \cdot d^2} \sqrt{\frac{E}{\varrho}} \cdot \frac{60}{\sqrt{(1 \pm k)^2 - \lambda}} \tag{4.12}$$

In equations (4.11) and (4.12), the same problem of precision appears as in chapter 4.2.4, due to the approximation formula and the empirical variables.

4.4. Balancing of disks and impact on their dynamic behavior

Unbalancing occurs on rotating objects when the rotating axis does not equal the main axis of inertia. Unbalancing at high speeds leads to high forces and to vibrations. There are three different kinds of unbalancing:

- Static unbalancing
- Couple unbalancing
- Dynamic unbalancing

Static unbalancing occurs when the center of gravity of a body is not on the axis of rotation. The unbalance is defined as a point mass at a certain radius from the center of rotation and is given with equation 4.13:

$$\mathbf{U} = m \cdot \mathbf{r} \, [\mathrm{g\,mm}] \tag{4.13}$$

During the static balancing process, a counter weight is placed at an angle of 180° to the unbalanced mass in order to compensate this parasitic mass. Couple unbalance occurs on a statically balanced rotor, which has two equal masses positioned symmetrically about the center of gravity but placed on the opposite side of the middle layer of the rotor or disk. When a disk rotates, these two masses shift the inertia axis, so that it is not aligned with the axis of rotation any more. Dynamic unbalancing describes a combination of both, static and couple unbalancing. It occurs on most rotors due to the fact that it is hardly probable that two equal masses, which are out of the middle layer, are turned to each other at exactly 180°.

If the rotor has a diameter of more than 10 times its thickness, static balancing is reasonable [83]. Nevertheless, a very good balancing is only achievable with a static and a dynamic balancing. The CFRP disks dealt with in this thesis are all balanced statically and dynamically. Figure 4.2 shows a CFRP disk with a diameter of 750 mm and a mass of 5.8 kg mounted on a dynamically balancing machine. Typical values of the residual unbalance of such a disk are $4\,[\mathrm{g\,mm}]$ for the static case and $420\,[\mathrm{g\,mm^2}]$ for the dynamic case.

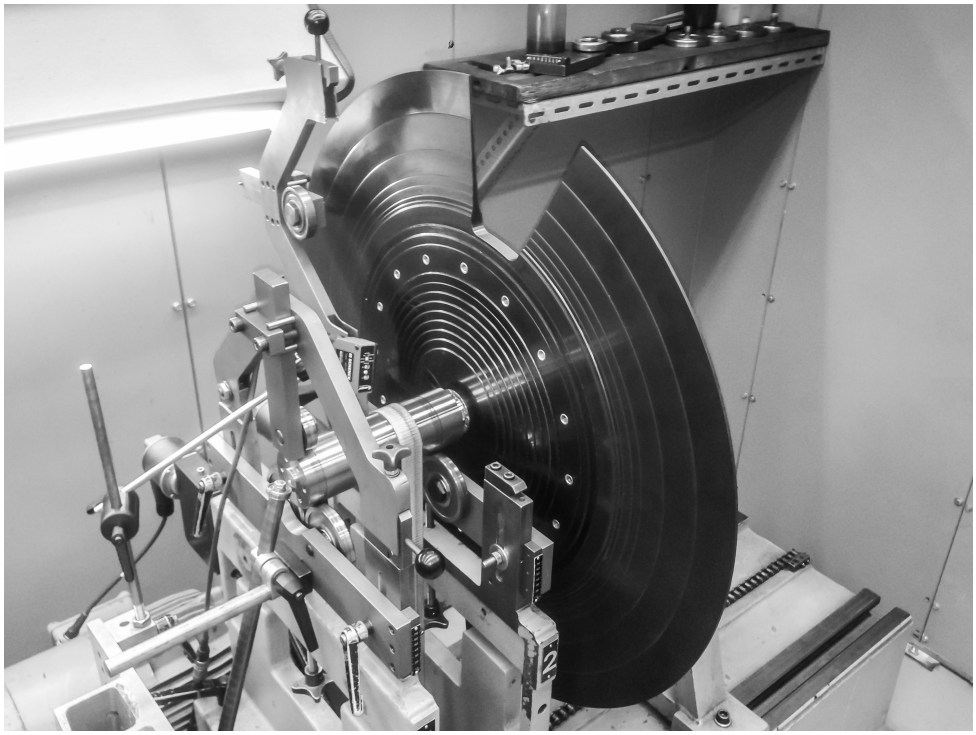

Figure 4.2.: CFRP disk mounted on a balancing machine.

5

Structural analysis of CFRP disks

In this chapter, a detailed structural analysis of the strain distribution, the strength and the natural frequencies of rotating CFRP disks is presented.

Contents

5.1. Structural analysis of a CFRP disk

As a basis for the calculations and optimizations, an actual chopper disk with a diameter of 700 mm is chosen. The disk has been designed for a rotational speed of 333.3 Hz and has two cut-outs, as illustrated schematically in figure 1.2. The dimensions of the disk and the requirements on the disk are listed in table 5.1.

Table 5.1.: Dimensions of the actual chopper disk.

Diameter	700 mm
Maximum thickness	26.2 mm
Minimum thickness	3.2 mm
Operational speed	333.3 Hz
Material	M30SC carbon fiber prepreg
Number of windows	2
Opening angle of the windows	34 °
Depth of the windows	135 mm
Mass	5.351 kg
Diameter of the central through-hole	50 mm

Table 5.2.: Material properties M30SC UD.

$E_\parallel$ [MPa]	$E_\perp$ [MPa]	$G_{\parallel\perp}$ [MPa]	$R_\parallel^-$ [MPa]	$R_\perp^-$ [MPa]	$R_{\parallel\perp}$ [MPa]	$R_\parallel^+$ [MPa]	R_{ILSS} [MPa]
149 130	6 595	3 070	2 535.5	30.4	104.6	682.5	65.1

5.1.1. Finite element model for the analysis of a disk

A finite element (FE) model is built and the three design criteria of natural frequencies, disk-hub connection and strength are calculated. The laminate of the disk is obtained by hand lay-up of M30SC prepreg and press molded at 135 °C at a pressure of 6.8 bar. The stacking sequence is quasi-isotropic and symmetrical of the form $[0/45/90/\text{-}45]_{s,n\text{-}times}$, with a nominal ply thickness of 0.156 mm. The material properties of the unidirectional lamina are summarized in table 5.2. These properties are measured by LLB according to

DIN EN 2561, DIN 65378, DIN EN ISO 527-4 and DIN EN 2563 [38, 39, 40, 41]. The material properties of the quasi-isotropic laminate are listed in table 5.3. The tensile modulus and the shear modulus of the laminate are calculated from the values of the unidirectional lamina. The elongation at break $\varepsilon_{\max,test}$ = 1.78 % of the quasi-isotropic laminate at specimen level is measured by LLB according to ASTM D 3039 [14]. A safety factor of 1.4 for manufacturing deviations is applied to this ultimate strain. This safety factor has been validated by many burst and crash tests done by LLB in previous chopper disk projects.

Table 5.3.: Material properties M30SC quasi-isotropic laminate $[0/45/90/\text{-}45]_s$.

E_{xx}, E_{yy} [MPa]	E_{zz} [MPa]	G [MPa]	ϱ [$\frac{\text{g}}{\text{cm}^3}$]	$\varepsilon_{\max,test}$ [%]	$\varepsilon_{\max,emp}$ [%]
54 000	6 600	21 000	1.52	1.78	1.27

5.1.2. Computation of the natural frequencies

First, the natural frequencies of the disk are calculated with a numerical modal analysis. In order to verify this analysis, the natural frequencies are measured. For this, four acceleration sensors are placed on the edge of the disk, and the natural frequencies are measured using a bump test in which the disk gets treated with a hammer. To obtain values that allow for a comparison of the numerical modal analysis with the measurement, the impact of the sensors on the mass distribution of the disk has to be taken into consideration. Each sensor has a weight of 20 g and is placed on the outer diameter of the disk. The FE model of the disk is modified in a way that the sensors are modeled as mass points. A more detailed description of the measurement of the eigenmodes can be found in chapter 7.1.

Table 5.4.: Comparison of the natural frequencies of the modified FE model with the measurement.

	Mode 1	Mode 2	Mode 3
Modified FE model	169 Hz	193 Hz	218 Hz
Measurement	162 Hz	188 Hz	209 Hz

In comparison to the measurements, the numerical results of the modified FE model

show a deviation of between 3 % and 5 %. The values are shown in table 5.4. Concerning the natural frequencies, the FE model used here shows a deviation rate lower than 10 % and can thus be regarded as an appropriate one. The shapes and the corresponding frequencies of the first three natural frequencies of the disk without acceleration sensors are shown in figure 5.1.

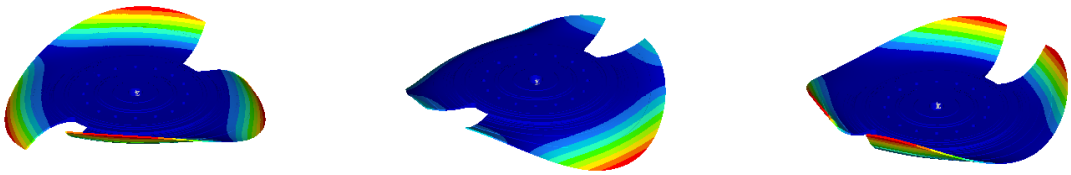

Mode 1: 217 Hz | Mode 2: 228 Hz | Mode 3: 237 Hz

Figure 5.1.: Shapes and values of the first three natural frequencies.

5.1.3. Computation of the radial displacement of the central through-hole of a CFRP disk

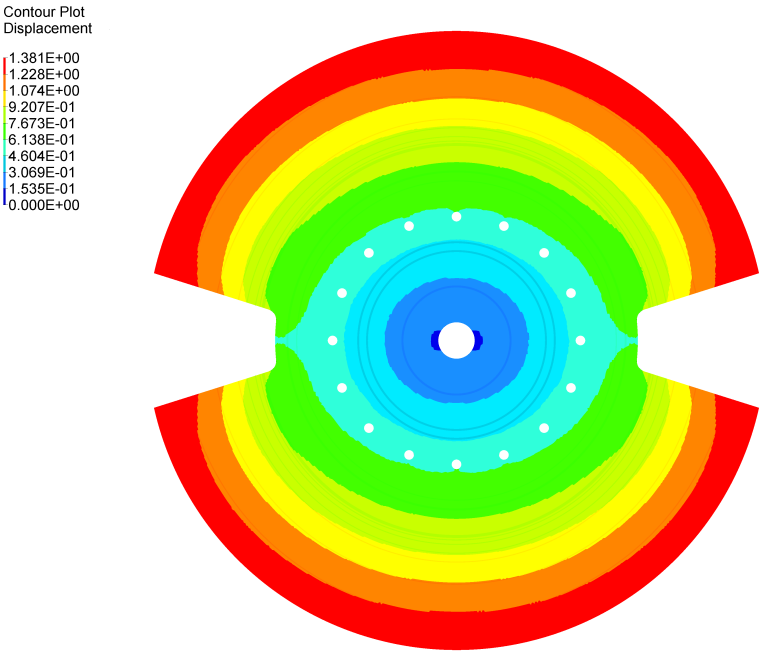

Figure 5.2.: Radial displacement field of a CFRP disk at 350 Hz.

The second design criterion, the disk-hub connection, is mainly determined by the radial extension of the central through-hole. The analysis of the actual disk shows an oval radial widening around the central hole of between 0.11 mm to 0.14 mm at a rotational speed of 350 Hz. The radial displacement of this disk is plotted in figure 5.2. The oval shape of the widening is caused by the non-uniform mass distribution due to the cut-outs. The smallest radial extension is in the direction of the cut-outs, where centrifugal forces are at their lowest. To verify these calculations, a CFRP disk without cut-outs is manufactured. The radial extension of the central through-hole of this test disk is 0.10 mm at a rotational speed of 298 Hz. In this disk, a full aluminum hub with a radial oversize of 0.10 mm is assembled by cold pressing-in. The radial extension of the aluminum hub during rotation is 0.001 mm, which can be regarded as negligible. Hence, a spinning test of this disk is done with the aim of measuring the detachment of the disk from the hub at a rotational speed around 298 Hz. During the spinning test, the vibrations of the shaft are measured. They are plotted together with the rotational speed versus the time in figure 5.3, where three areas are marked. The first area I shows a resonance starting at $t = 180$ s and ending at $t = 410$ s with a maximum vibration of 18 %. This resonance is the second eigenmode of the shaft and occurs in every spinning test of a comparable disk. In area II, the disk gets further accelerated from 280 Hz to 306 Hz, showing a constant vibration level around 20 %. At a rotational speed of 306 Hz there is an abrupt increase in shaft vibrations from 20 % to 90 %, which is caused by the disk detaching itself from the hub. This is a deviation of 2.7 % from the calculated detachment speed. The detachment is marked with area III in figure 5.3. Accordingly, the FE model of the disk-hub connection can be seen as an appropriate one and can further be used for optimization tasks.

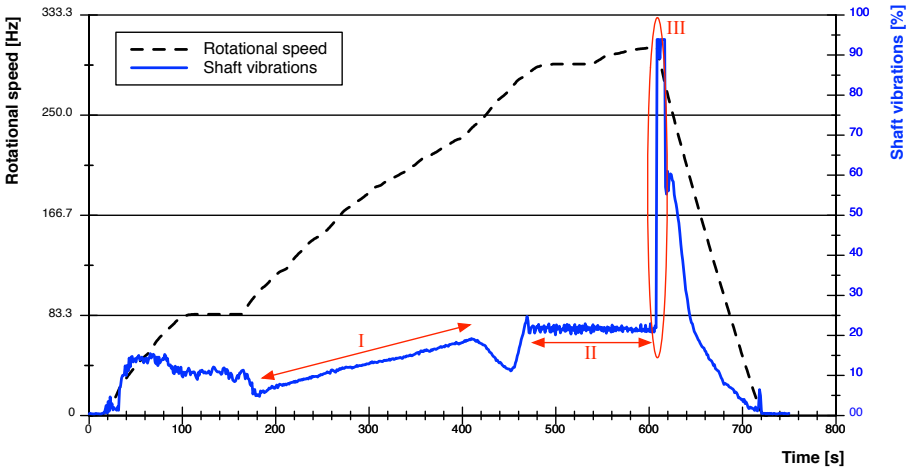

Figure 5.3.: Spinning test of a disk without cut-outs and with a full aluminum hub.

5.1.4. Calculation of the strain in disks caused by vibrations

During the acceleration of a disk, the passing of resonance frequencies is inevitable. If the rotational speed of the disk equals a natural frequency, the disk gets triggered with the corresponding eigenmode. An experimental measurement of the pass of a resonance frequency is shown in chapter 7.2.1. The vibration caused by this resonance implies a bending load on the disk. The larger the amplitude of the vibration, the larger is the bending load. The deflection of the amplitude is mainly driven by the damping of the disk. An exemplary bending strain of a disk is shown in figure 5.4. The displacement is scaled by factor 10. The maximum strain of 0.14 % occurs at the edge of the cut-out in the outer layer of the disk, which is the boron coating. This strain is 10 times lower than the maximum tolerable strain of the boron coating. Additionally, the strain occurs in an area which is slightly stressed by the centrifugal load during rotation. From this it follows that the load implied by the passing of resonance frequencies is bearable for the structure and does not need to be considered during the optimization process. Nevertheless, before the end of the constructive design process, a calculation of the bending strain is conducted for each disk.

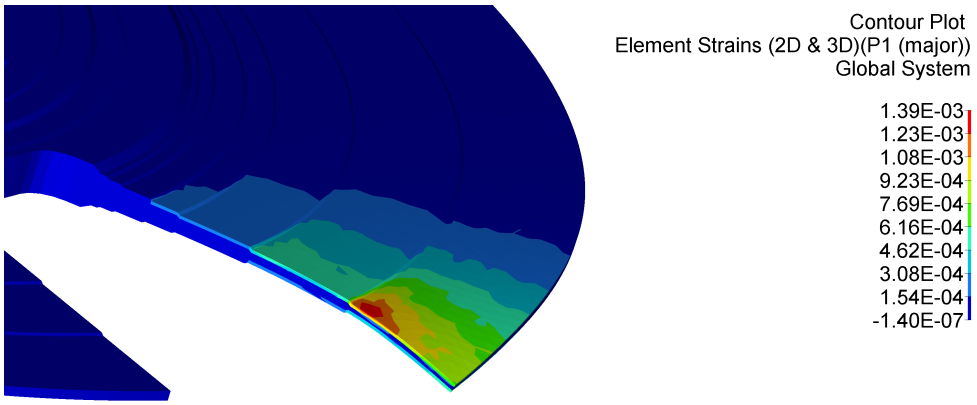

Figure 5.4.: Strain distribution in a CFRP disk caused by a bending load.

5.2. Contact analysis of the disk-hub connection

Up until now, the behavior of the press fitted disk-hub connection was evaluated by independently analyzing the disk and the hub. The contact condition at operational velocity was defined by comparing the radial displacements of the central through-hole of the disk with the outer surface of the hub. The design of the press fitting was accepted if the widening of the hub was equal to or higher than the widening of the through-hole of the CFRP disk. This approach follows the assumption that the CFRP disk is much stiffer than the aluminum hub. Thus, the widening of the central through-hole of the disk is not influenced by the contact pressure. An analysis of the three-dimensional widening of the through-hole of a CFRP disk is shown in the half-section in figure 5.5. The maximal radial widening of 0.23 mm occurs in the center plane of the disk [20, 21].

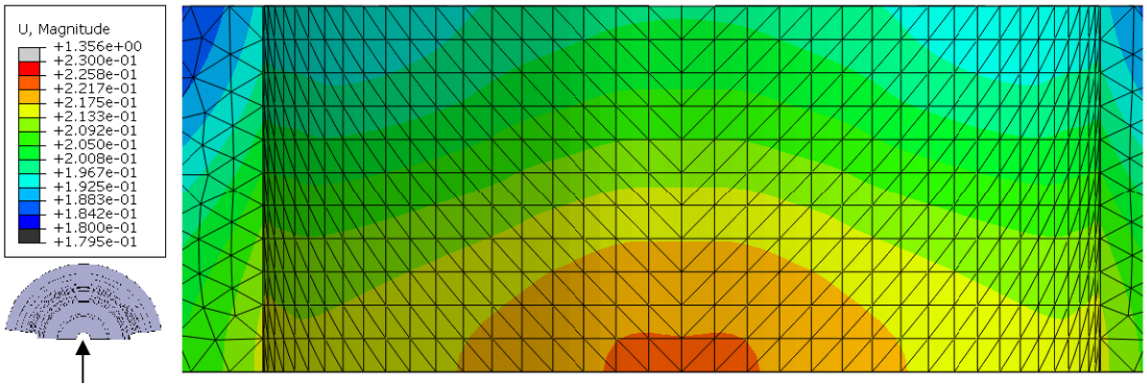

Figure 5.5.: Half-section of the radial displacement field of the central through-hole of a CFRP disk at a rotational frequency of 500 Hz.

While providing a first evaluation of the contact behavior, the approach described above has some shortcomings. Firstly, it neglects that the hub does not remain in a perfect cylindrical shape after assembling. Initially, only the edges of the bearing surfaces are in contact, while the major part of the surface is bent inwards. This is shown in figure 5.6. This phenomenon is tested experimentally with an existing CFRP disk and an aluminum hub. The hub is pressed out of the CFRP disk and the scratches on the indentation of the hub and the disk do not show exactly the condition predicted by the calculations. The indentation is shown in figure 5.7 with red marks. On the left side (a) in figure 5.7, the scratches on the indentation in the CFRP disk are shown and on the right side (b), the indentation in the aluminum hub. The result of the calculation is that only a line at the edge of the wings of the hub is in contact with the disk. The experimental test confirms

that indeed not the complete wing is in contact with the disk but it also shows that the contact area is larger than a line.

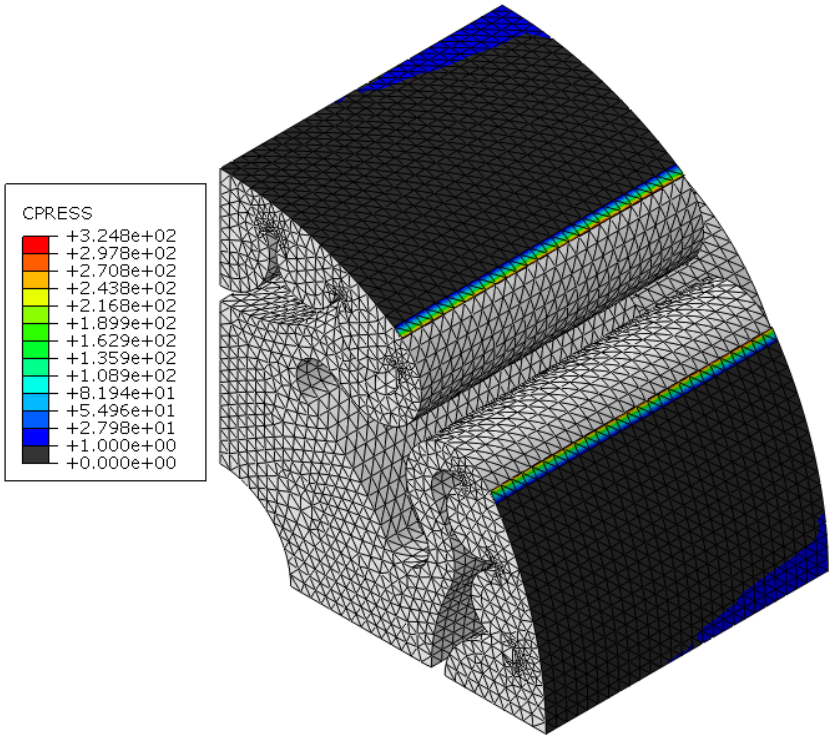

Figure 5.6.: Initial contact pressure between disk and hub after the cold pressing-in.

Moreover, the influence of the non symmetrical widening of the central through-hole of the CFRP disk is not taken into account in the independently modeled approach. The widening of the disk shows a gradient in thickness direction due to its tapered cross section. Also, the cut-outs lead to an asymmetry in the radial displacement. Lastly, a simple comparison of the radial displacements only allows for a qualitative statement on the contact state, yet no information on the actual contact pressure can be obtained. Therefore, a new approach is made and described below.

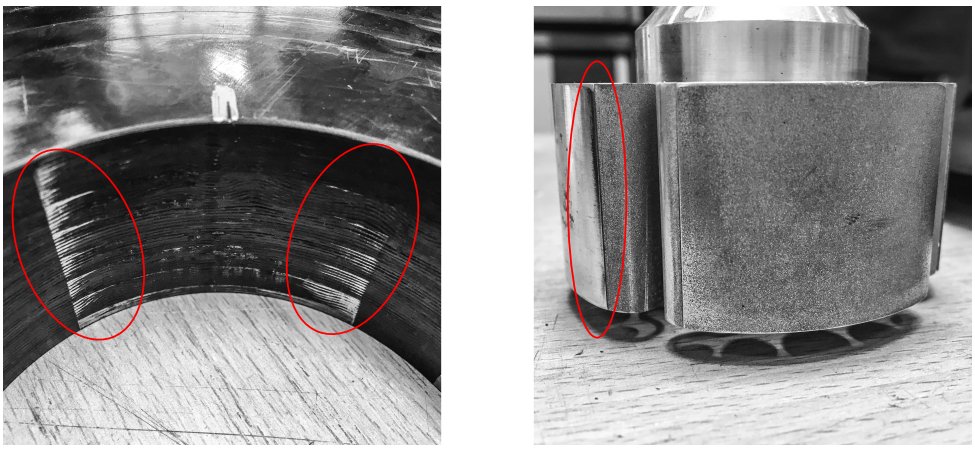

(a) (b)

Figure 5.7.: Scratches on the indentation of the disk (a) and on the pressed-out hub (b).

5.2.1. Finite element modeling of the contact phenomena of the disk-hub connection

A three-dimensional finite element model including both disk and hub is created and the contact interactions are evaluated. Nonlinear static analyses are carried out using the methods described in chapter 3.3. The results of these calculations are the contact area and the contact pressures. The values obtained for the contact area and the pressure are appropriate indicators for comparing different press-fitting designs, but without a failure criteria, it is not possible to predict the detachment precisely.

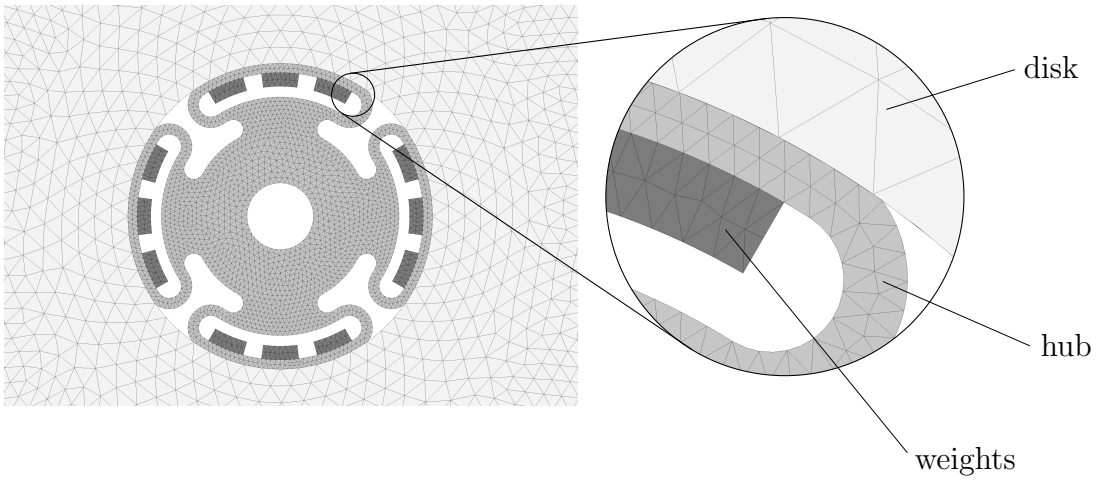

Figure 5.8.: FE model of the aluminum hub with the tungsten weights and the CFRP disk with a zoom into the contact area.

Table 5.5.: Material properties of the CFRP used for the nonlinear contact analysis between the CFRP disk and the aluminum hub with the tungsten weights.

E_{xx}, E_{yy} [MPa]	E_{zz} [MPa]	G [MPa]	G [MPa]	ν_{xy} [−]	ν_{xz}, ν_{yz} [−]
54 300	7 290	20 500	2700	0.322	0.260

Figures 5.8 and 5.9 show exemplary FE models of the assembly. Only one eighth of the disk and the hub are modeled and symmetry boundary conditions are applied. The full model consists of a total number of 900 000 tetrahedral elements with quadratic shape functions. A relatively fine mesh is applied to the hub and the region around the central through-hole of the disk, whereas the rest of the disk is meshed with larger elements, since the interest in the results of the analysis is limited to the contact surfaces and their behavior at high rotational frequencies. Equivalent orthotropic properties of the laminate are used and listed in table 5.5. The boron coating is modeled with non-structural mass points on the outer area of the disk. A major difficulty arises from the modeling of the tungsten weight bars, which are used to increase the contact pressure between the hub and the disk at high rotational frequencies. As shown in figure 5.9, they are glued as stripes on the inner surface of the hub wings.

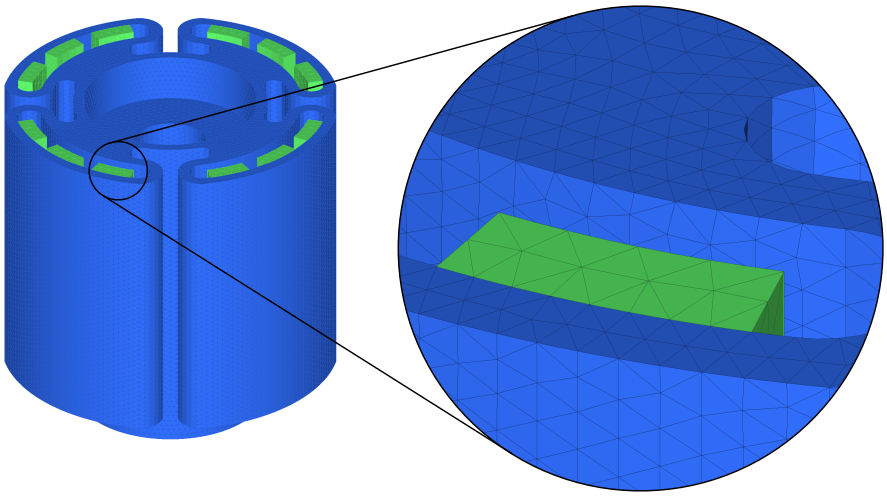

Figure 5.9.: FE model of the hub with the tungsten weights (green).

In order to limit the computational effort, a single mesh covering the hub and the weights is chosen. Figure 5.9 shows in its zoom the conforming mesh and the coincident

nodes at the boundary between the hub and the weight bars. However, this does not reflect the real configuration, which only allows for a transfer of compression loads between the aluminum hub and the tungsten weights. The conforming mesh leads to an unrealistic stiffening of the hub. One option to counteract this unwanted stiffening is to use properties with a lower stiffness for the tungsten weights. All hub designs are analyzed with two values for the tungsten Young's modulus - the original value, given in table 5.6 and representing the more conservative case, and a reduced modulus of 2 000 [MPa]. The actual solution can be expected to be in between of those two cases.

Table 5.6.: Material properties of the aluminum and tungsten used for the contact analysis of the hub.

	E [MPa]	ν [−]	ϱ [$\frac{\text{g}}{\text{cm}^3}$]	$R_{p,0.2}$ [MPa]
Aluminum 7075	72 400	0.3	2.7	300
Tungsten Densimet D176	360 000	0.3	17.6	

Contact interactions are defined between the outer hub surfaces and the inner surface of the central through-hole of the CFRP disk. Figure 5.8 shows the initial configuration with a nonconforming mesh and an overlap due to the oversize fitting. The bearing surfaces of the hub are chosen as the slave side, due to the lower stiffness and finer mesh. Only normal contact stresses are accounted for, i.e. a frictionless tangential behavior is assumed. The Lagrange multiplier method is used for constraint enforcement.

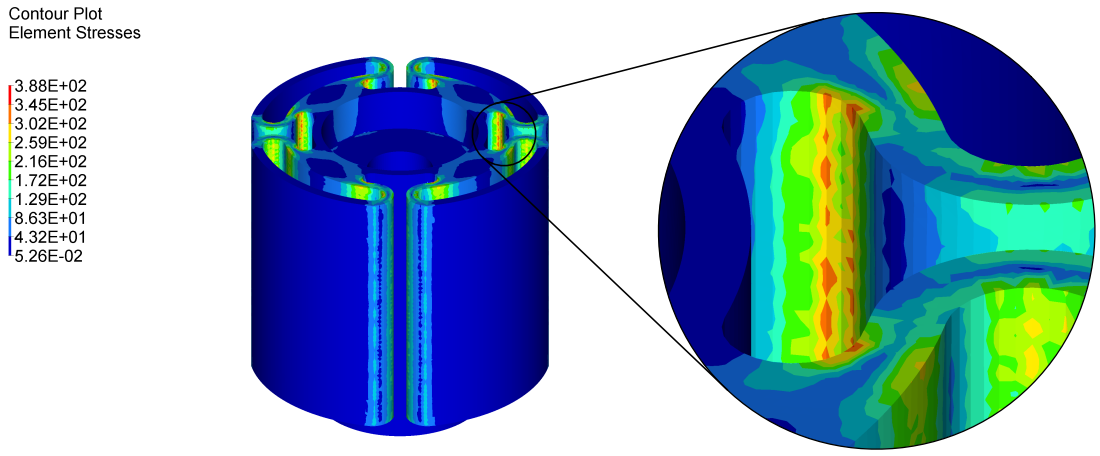

Figure 5.10.: Stress distribution of the hub after cold pressing-in [MPa].

6

Structural design optimization process for a holistic improvement of CFRP disks

After the analysis of high-speed rotating CFRP disks in the previous chapter, an enhanced design approach is presented in this chapter using analytical and numerical optimization tools. The aim is to achieve a dynamically more stable disk. The three major aspects of natural frequencies, of widening of the central through-hole and of the failure index in the highly stressed areas of the disk are taken into consideration in a holistic optimization process.

Contents

6.1. Analytical optimization of the widening of a rotating disk

An analytical solution for the displacement field of a circular disk is established. It is assumed that the disk shows one clear thickness jump at r_E and further, that the thickness h' after the jump is far lower than the inner one, i.e. $h' \ll h$. The contribution of this much lower thickness h' is neglected in terms of stiffness, albeit, its moment of inertia is not.

$$r' = \frac{h'}{r_E^2 \cdot h}(r'_E)^3 \tag{6.1}$$

A sketch of the disk used for the analytical consideration is shown in figure 6.1.

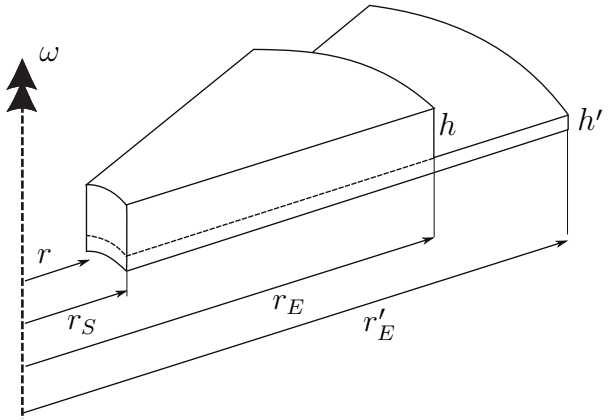

Figure 6.1.: Sketch of the analytical model.

The equation of mechanical equilibrium stated in cylindrical coordinates is given in equation (6.2):

$$\nabla_r \sigma + \vec{f} = 0 \tag{6.2}$$

A plane stress state is assumed, i.e. $\sigma_{zz} = \sigma_{\vartheta Z} = \sigma_{rz} = 0$, as well as an axial symmetry of $\sigma_{r\vartheta} = 0$, which leads to $\frac{\partial \sigma_{\vartheta\vartheta}}{\partial \vartheta} = 0$ and therefore to $\sigma_{\vartheta\vartheta} = \sigma_{\vartheta\vartheta}(r)$. The first equilibrium in r direction given by equation (6.2) is

$$\frac{\partial \sigma_{rr}}{\partial r} + \frac{\sigma_{\vartheta\vartheta} - \sigma_{rr}}{r} = b_r. \tag{6.3}$$

The body force b_r is caused by the centripetal acceleration and can be defined to be

$$b_r = -\rho \omega_{cyc}^2 (r - r_S + r'), \tag{6.4}$$

with ω_{cyc} being the rotational speed of the disk. Inserting the constitute law and the kinematic equation into (6.3) leads to the differential equation for the radial displacement field u_r.

$$r^2\frac{\mathrm{d}^2u_r}{\mathrm{d}r^2} + r\frac{\mathrm{d}u_r}{\mathrm{d}r} - u_r + \frac{1-\nu^2}{E}\rho\omega_{cyc}^2 r^2(r - r_S + r') = 0 \tag{6.5}$$

With the following equation, the solution of the differential equation (6.5) is given.

$$u_r = c_1 r + c_2\frac{1}{r} - \frac{\xi_b}{8}r^3 - \frac{\xi_b}{3}r^2(r' - r_S), \quad \text{with } \xi_b := \frac{1-\nu^2}{E}\rho\omega_{cyc}^2 \tag{6.6}$$

The integration constants are determined by the boundary conditions imposed on the disk. Hence, the radial stresses σ_{rr} have to be zero at the inner radius of the disk, i.e. $r = r_S$, and $r = r_E$ at the outer ring of the disk.

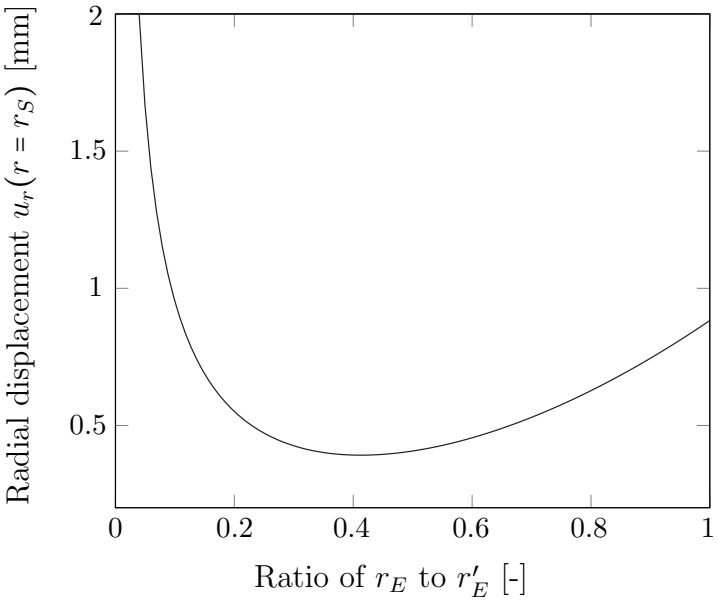

Figure 6.2.: Analytic results of the radial displacement of the central through-hole versus the ratio of r_E to r'_E.

As can be seen in figure 6.2, the widening of the central through-hole u_r has a distinctive minimum at roughly $\frac{r_E}{r'_E} \approx 0.4$. This analytical outcome is based on different assumptions. One assumption presumes the optimal thickness distribution for the given disk to be determined by a sharp step, as can be seen in figure 6.1. The results of the analytical optimization show a good correlation to the results of the numerical computation in section 6.2.3.

6.2. Numerical optimization of CFRP disks

A general optimization statement is given with equation (6.7), with **z**, **h**, **g** and **x** being the objective, the equality constraints, the inequality constraints and the design variable vector [57, 111]. Throughout the optimization process, the optimization algorithm minimizes the objective **z**, while simultaneously fulfilling all constraint functions **h** and **g**. These constraints basically represent restrictions imposed by physics or technical reality, e.g. stress limits or manufacturing restrictions [135]. Most later defined optimization tasks have been solved by taking advantage of the gradient-based optimization algorithm method of feasible directions (MFD), as it has proved conceptually simple, feasible in all iterations, and computationally efficient [30, 58, 69, 104].

$$\min_{\mathbf{x}} \{ z_i(x_j) \mid h_k(x_j) = 0 \mid g_l(x_j) \leq 0 \} \tag{6.7}$$

with

x_j	...	Vector of design variables with	j	=	$1, \ldots, n_{DV}$
$z_i(x_j)$	...	Vector of objective functions with	i	=	$1, \ldots, n_O$
$h_k(x_j)$	...	Vector of equality constraint functions with	k	=	$1, \ldots, n_{EC}$
$g_l(x_j)$	...	Vector of inequality constraint functions with	l	=	$1, \ldots, n_{IC}$

Equation 6.7 is the general mathematical form of an optimization problem. A multi-objective optimization problem appears when more than one objective $n_O > 1$ has to be considered [111]. In the case that only one objective function $n_O = 1$ occurs, the optimization problem is termed single objective optimization problem. In section 6.2.2, a CFRP disk is at first optimized with a single objective function. Subsequently, this optimization problem is extended in section 6.2.2.3 to a multi-objective optimization, which comprises a weighted sum of multiple natural frequencies.

The numerical optimizations are computed on a cluster at the Chair of Lightweight Structures at TUM. The cluster consists of 40 nodes of type FUJITSU Server PRIMERGY RX200 S8, each comprising a quad core processor Intel Xeon CPU E5-2637 v2 with 3.50 GHz [45]. The solving of the optimization problems with a number of iterations of between 6 and 30 requires a computation time of up to 5 h.

6.2.1. Finite element model for numerical design optimization of a disk

For a numerical optimization, a two dimensional FE model with a fine and symmetrical mesh is necessary. In contrast to the analysis of section 5.1, where triangular elements of the second order are used, in this section, a radial symmetrical mesh is generated of rectangular elements with quadratic basis functions. The quadratic basis functions are preferable to linear basis functions for avoiding an overestimation of the structural stiffness [18]. As a reference model for the numerical optimizations shown below, a rotational symmetrical model with 98 582 elements and 158 002 nodes is used. A sketch of the model is shown in figure 6.3. With the zoom of figure 6.3, it can be seen that the elements are built up with concentric circles and radial lines. Around the central through-hole, 250 elements are placed. To achieve constant aspect ratio of the elements from the inner to the outer diameter of the disk, the length in radial direction is increased in proportion to the radius. In the area around the cut-outs, the mesh is refined for obtaining more precise stress and strain results in this highly stressed area. A cylindrical coordinate system is used.

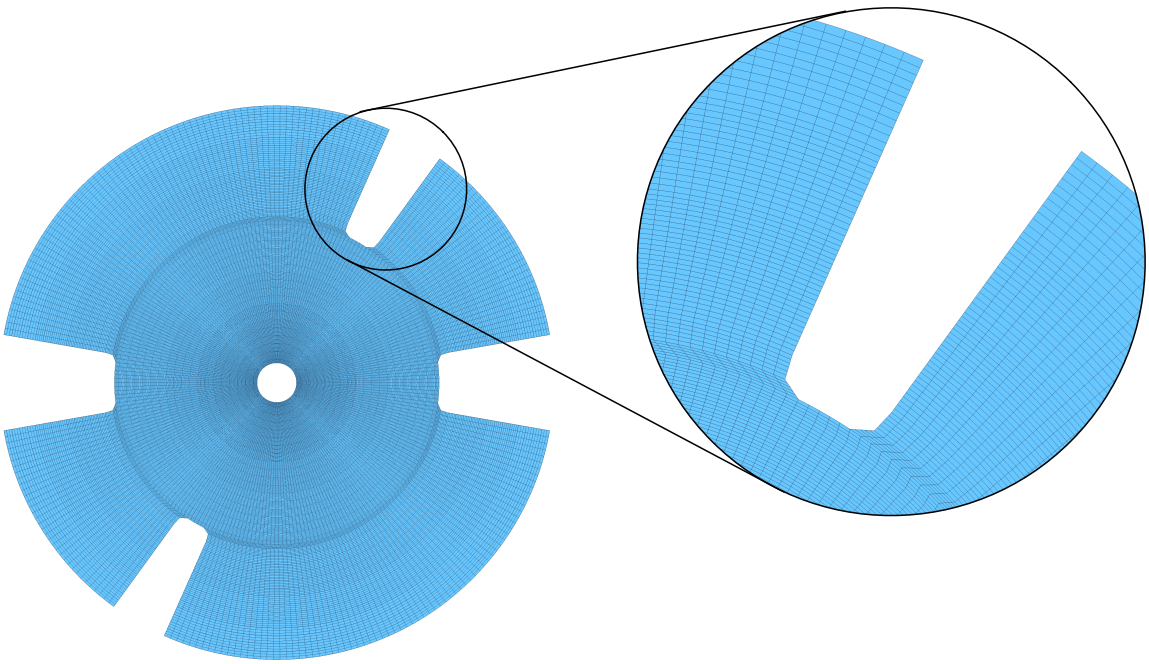

Figure 6.3.: FE model for the numerical optimization.

6.2.2. Optimization of the structural dynamic behavior

For the dynamically stable performance of a rotating disk, it is preferable if the natural frequencies are higher than the rotational speed [10, 83]. In this case, no excitation of natural frequencies or resonances is to be expected [87, 126]. If the disk passes a natural frequency during acceleration, the corresponding eigenmode will be triggered. Depending on the damping of the disk, this will consequently lead to strong vibrations or, in the worst case, to a resonance catastrophe.

Due to the centrifugal forces during rotation, the disk receives a membrane stiffening [49, 88, 127, 137]. The centrifugal forces induce strain in the structure, which leads to a prestress. With an increase of the strain and the corresponding prestress, the natural frequencies of the structure increase as well [51, 53].

With a numerical optimization approach, the thickness of the disk is varied for achieving maximal natural frequencies. The corresponding optimization task is formalized in general with equation 6.8.

$$\min_{\mathbf{t_P}} \{ z(\mathbf{t_P}) \mid \mathbf{g}(\mathbf{t_P}) \leq 0 \} \tag{6.8}$$

with

$$z = -f_e(\mathbf{t_P}) \tag{6.9}$$

$$g_1 = \frac{m(\mathbf{t_P})}{m_{max}} - 1 \leq 0 \tag{6.10}$$

$$g_{1+j} = FI_j \cdot N_{SF} - 1 \leq 0 \quad \text{with } j = 1, \ldots, n_{elem} \tag{6.11}$$

with

z	...	Objective function
f_e	...	Natural frequency
$\mathbf{t_P}$	...	Vector of ply thicknesses, i.e. vector of design variables
$\mathbf{g}$	...	Vector of constraints
m	...	Mass
FI_j	...	Failure index of element j
N_{SF}	...	Safety factor

In equation 6.8, f_e represents the natural frequencies. This optimization problem maximizes the natural frequencies with a variation of the thickness distribution while taking into account a mass restriction and failure restrictions. The maximum-strain failure criterion is used with an empirical value of $\varepsilon_{\max,emp} = 1.27\,\%$, which is the result of the

measured value of $\varepsilon_{\max,test} = 1.78\,\%$ applied with a safety factor of 1.4 in order to consider manufacturing deviations and other uncertainties. This safety factor has been determined in multiple strength tests of previous projects at LLB. Hence, this criterion allows for an acceptable prediction of the failure in the initial design process [60]. The material data of the applied M30SC quasi-isotropic laminate are equal to the ones shown in chapter 5.1 in table 5.3. Given the uncertainty regarding the load, a further safety factor of $N_{SF} = 1.2$ is added to the failure index FI_j.

Below, different variants for the objective function z are analyzed in a parameter study. In an initial step, only the first natural frequency is taken into consideration:

$$z = -f_{e,1}(\mathbf{t_P}) \tag{6.12}$$

This single objective function can be divided into three different variants:

1. First natural frequency of the static disk $f_{e,1}$
2. First natural frequency of the rotating disk $f_{e,1,\omega}$
3. First natural frequency of the static disk with mode-tracking $f_{e,1,track}$

Variant 1 differs from variant 2 in that it considers the membrane stiffening of the disk due to the centrifugal forces during rotation. The maximum membrane stiffening is achievable by reducing the laminate to its minimum thickness, as can be seen on the right side in figure 6.4. This is in contrast to an optimum weight distribution for high natural frequencies. It is also in total contrast to the maximum achievable rotational speed of the disk, which is mainly driven by the centrifugal load [96, 123, 150]. In table 6.1, the values of the natural frequencies of variants 1 and 2 are shown for the static case, hence for the non-rotating disk. Between the values of variants 1 and 2, there is a factor of ca. 10 in the static case. The first natural frequency in variant 1 is 245.4 Hz while it is 20.4 Hz in variant 2. The corresponding thickness distribution of both variants is shown in figure 6.4.

Table 6.1.: Comparison of the natural frequencies of the objective functions concerning the static and the rotating disk in the static system.

Mode No.	1	2	3	4	5	6	7	8	9	10
$z = f_{e,1}$ [Hz]	245.4	247.5	251.1	256.8	294.2	302.4	331.0	339.4	342.8	354.3
$z = f_{e,1,\omega}$ [Hz]	20.4	21.5	26.9	27.4	42.7	43.2	58.4	58.9	69.8	70.4

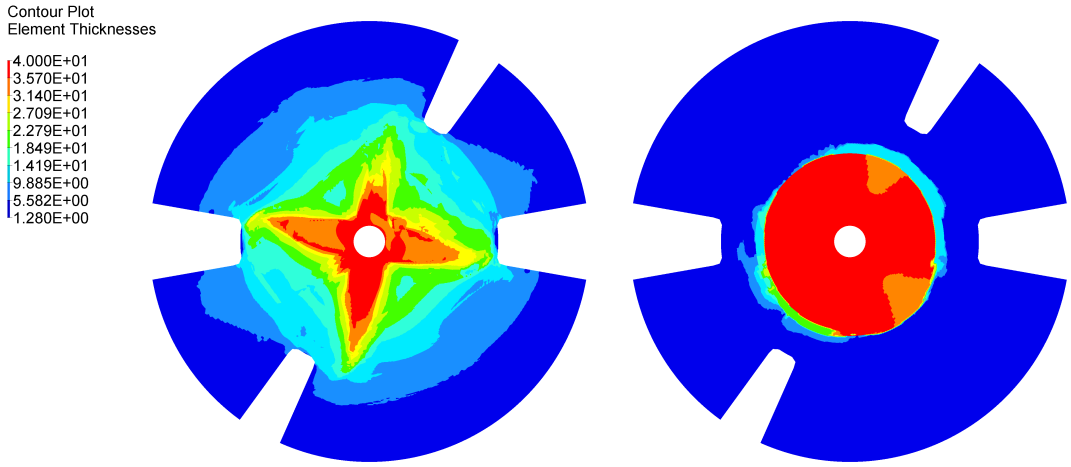

Figure 6.4.: Comparison of the thickness distribution of the optimized disk with objective functions concerning the static (left) and the rotating (right) disk.

In table 6.2, a comparison between the natural frequencies of the objective functions concerning the static and the rotating disk in the system rotating at 384 Hz is listed. In contrast to the static case, where the results differ from each other by a factor of 10, the values of the first natural frequency during rotation are close to each other. The first natural frequency in variant 1 is 544.6 Hz while it is 532.2 Hz in variant 2. This shows that the optimization of variant 2 converges in a local minimum. For the first 10 natural frequencies, the values of variant 1 are all higher than the ones of variant 2. Nevertheless, both variants lead to a first natural frequency during rotation being higher than the rotational frequency. Concerning manufacturing constraints, variant 2 shows a non-producible thickness distribution. Hence, in section 6.2.2.1, the manufacturing constraints are added to the optimization.

Table 6.2.: Comparison of the natural frequencies of the objective functions concerning the static and the rotating disk in the system rotating at 384 Hz.

Mode No.	1	2	3	4	5	6	7	8	9	10
$z = f_{e,1}$ [Hz]	544.6	560.1	575.4	633.7	673.3	717.9	767.2	787.8	809.5	819.8
$z = f_{e,1,\omega}$ [Hz]	532.2	536.0	541.3	546.3	571.2	581.1	582.4	586.7	590.9	599.3

Variant 3 of the optimization, which includes a mode-tracking, leads to different results. The solution is bound to the first natural frequency of the first iteration. Normally, the shape of the first eigenmode is a bending mode of the disk. Consequently, an increase of

this first bending mode is achievable by a thick rib in 90° orientation to the bending axis. When the optimization has converged, the value of this tracked first natural frequency is increased by factor 10 or even more, whereas the second natural frequency, which is now the one with the lowest value, remains at a low level. The thickness distribution of a disk optimized for a high first natural frequency with mode tracking is shown in figure 6.5.

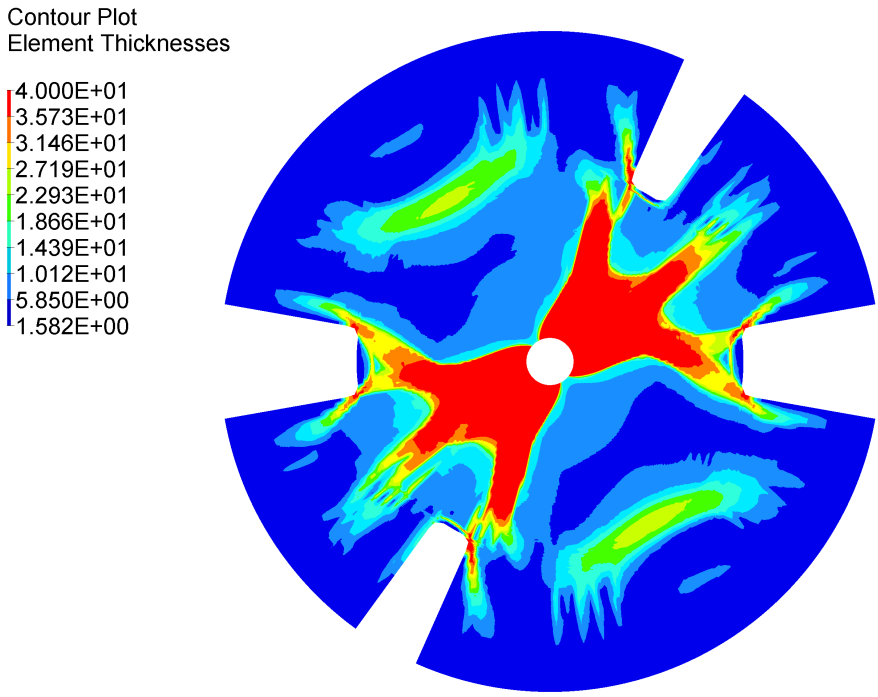

Figure 6.5.: Thickness distribution of a disk optimized for a high first natural frequency with mode-tracking.

As predicted, a rib occurs diagonally across the disk. On the large wings, there are two additional small ribs with a maximum thickness of 30 mm. The design is very stiff in the direction of the first bending mode but neglects all shapes of the other eigenmodes. Hence, the shape of the first eigenmode of the optimized design shows a bending mode with an axis of 90° to the optimized one. This shape of the first eigenmode is shown in figure 6.6. In summary, it can be said that the mode-tracking increases the natural frequency of the tracked mode significantly yet leads to an unsuitable design for two reasons: First, the second natural frequency remains at a low value and becomes the new first eigenmode of the optimized design. Second, the gradient of the thickness distribution is too high. The first shortcoming can be treated by formulating a multi-objective problem statement, as introduced in section 6.2.2.3. Such a multi-objective optimization is able to take into

account multiple natural frequencies. The second shortcoming can be treated by adding a constraint to the gradient of the thickness distribution.

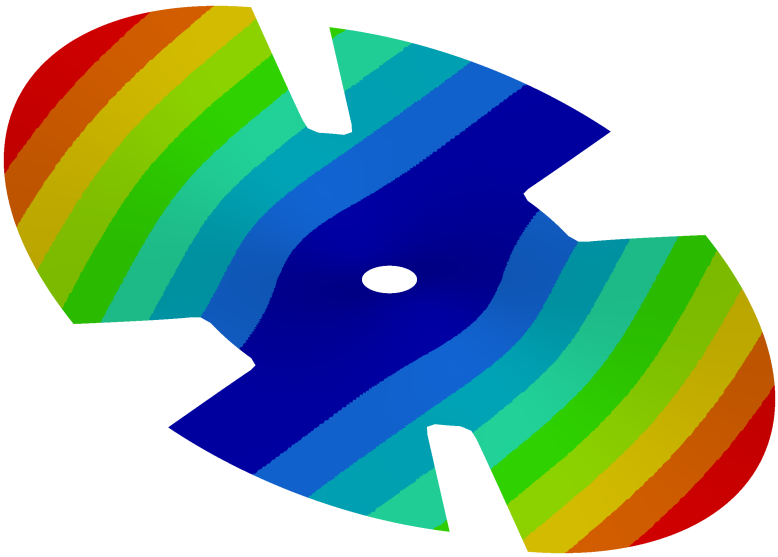

Figure 6.6.: Shape of the first natural frequency taken into consideration by the mode-tracking function.

Such a focus placed by mode-tracking on the first natural frequency and on the shape of the first eigenmode can be avoided if the objective function is extended to several natural frequencies. An example is given with equation 6.13:

$$z = -\sum_{i=1}^{n_{f_e}} f_{e,i}(\mathbf{t_P}) \tag{6.13}$$

This optimization problem maximizes the sum of the first natural frequencies from 1 to n_{f_e} with a variation of the thickness distribution, while taking into account a mass restriction and failure restrictions. The result of this optimization concerning the first five natural frequencies with $n_{f_e} = 5$, a mass restriction of 9 kg and a design space limit of 40 mm is a variant with more ribs compared to the results before. The main rib has disappeared but several small ribs around the cut-outs and on the wings have appeared. The thickness distribution is shown in figure 6.7. With the sum of the first five natural frequencies, the optimization problem is a multi objective one, which is dealt with in detail in section 6.2.2.3.

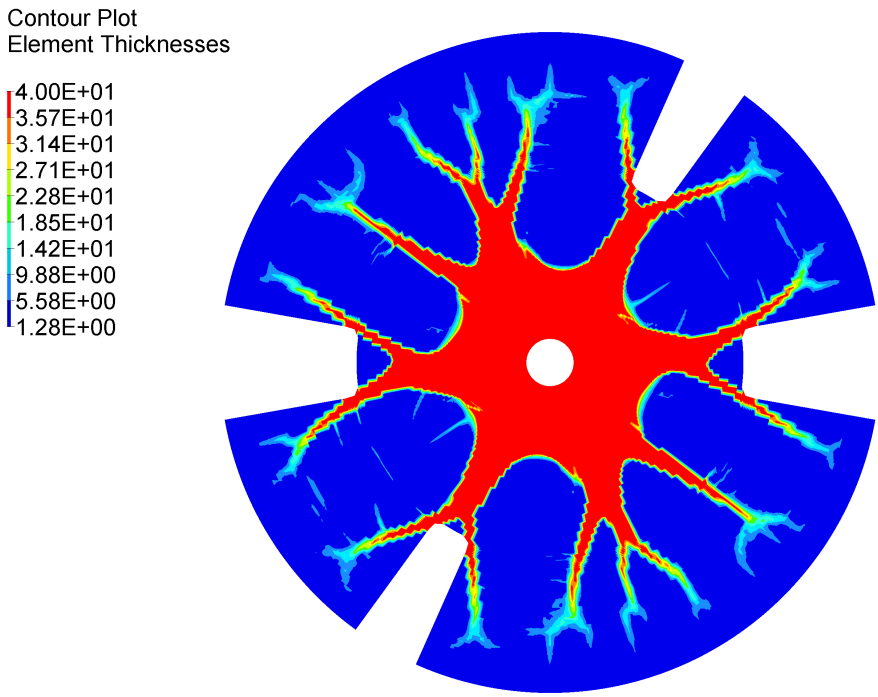

Figure 6.7.: Optimized thickness distribution for higher natural frequencies with regard to the first five natural frequencies.

6.2.2.1. Manufacturing constraints in the optimization process

Some of the thickness distributions presented in the previous sections have an abrupt change in thickness, which leads to problems during manufacturing as well as to stress peaks in the laminate [111, 112]. Regarding the manufacturing constraint of a rotationally symmetric disk, two possibilities are presented in this section. First, a cyclic pattern grouping with 140 equal areas and second, a zone based optimization with 34 circular zones with an equal thickness of the laminate. The first variant of the cyclic pattern grouping is equal to a cake with 140 equal pieces, and is a suitable solution for a disk. The high number of cyclic patterns prevents the occurrence of ribs. It is important to ensure that the number of elements at the inner diameter of the disk is higher than the number of patterns. The second variant divides the disk into different zones, which have a constant thickness of the laminate. This reduces the number of design variables considerably. In the previous optimization tasks, the number of design variables equals the number of elements in the design space. A FE model of a disk with 34 circular zones is shown in figure 6.8. The design variables are reduced from 52 330 free sizing elements to 34 zones, which reduces the computational time by a factor of 2.3 from `03h:15min` to `01h:30min`.

The absolute time refers to the quad core processor used, which is an Intel Xeon CPU E5-2637 v2 with 3.50 GHz as described in section 6.2.

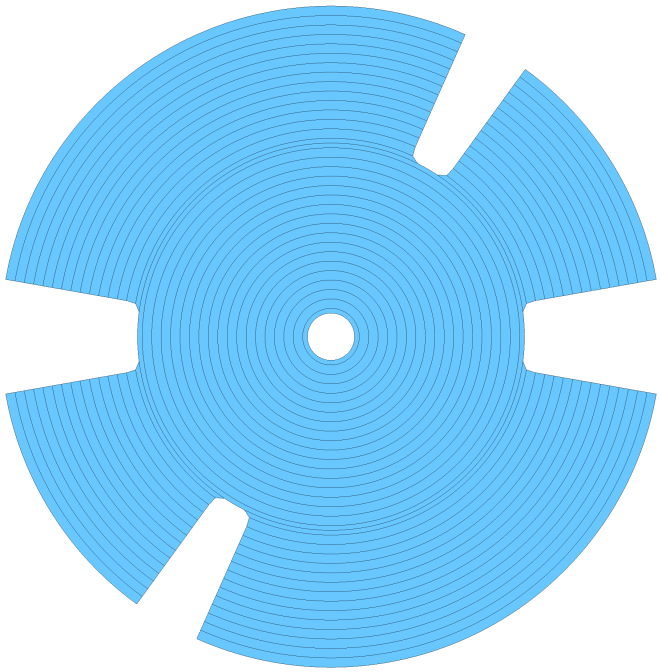

Figure 6.8.: Zone based optimization model.

In figure 6.9, the optimized thickness distribution of a CFRP disk with a mass constraint of 9 kg and design variables with a limit of 40 mm is shown. Compared to figure 6.7, the ribs around the cut-outs have disappeared and the gradient of the thickness change is significantly smaller. The objective function is referred to in equation 6.12 with variant 1, where the single objective function considers the first natural frequency in the static case. The first natural frequency of this design is 269.1 Hz in the static system and thus 10 % higher than in the design which does not consider manufacturing, as listed in table 6.1.

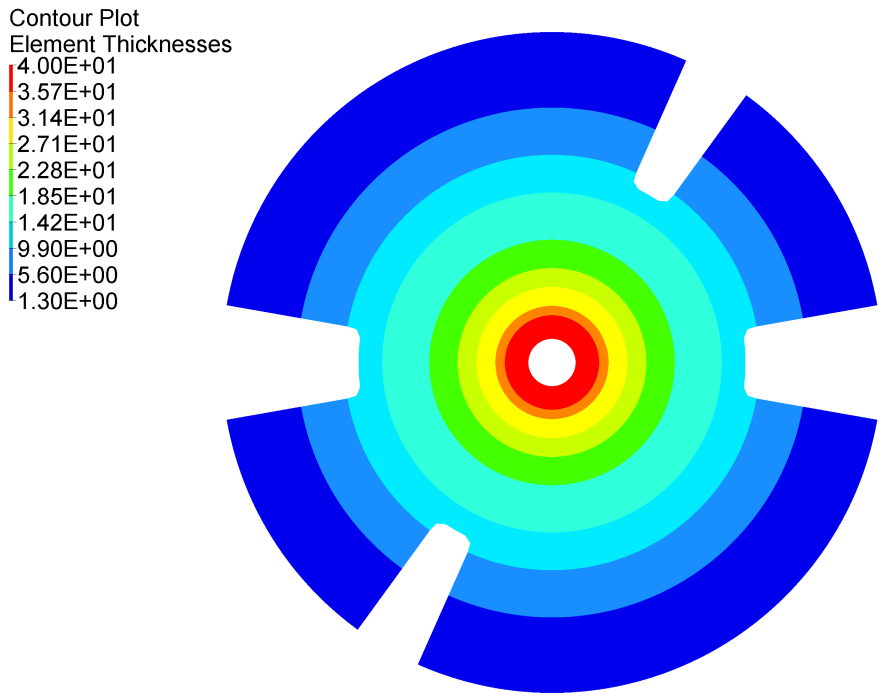

Figure 6.9.: Thickness distribution of a CFRP disk, optimized for high natural frequencies with regard to manufacturing constraints.

6.2.2.2. Convergence behavior of the optimization

In this section, the convergence behavior of the optimization is described exemplarily. The convergence of the unweighted optimization corresponding to table 6.3 with $\xi_i = 1$ is plotted in figure 6.10. Iteration 0 starts with a constant value of 9.7 mm for all design variables, which causes a first natural frequency of 58.2 Hz in the static system. After six iterations, the maximum of the first natural frequency is reached with a value of 156.7 Hz, while all constraints are fulfilled. Depending on the size of the FE model and the optimization task, the number of iterations can vary from 5 to over 50. For most of the optimization tasks, a stop criterion of 80 iterations is chosen and the convergence tolerance is set to 0.005.

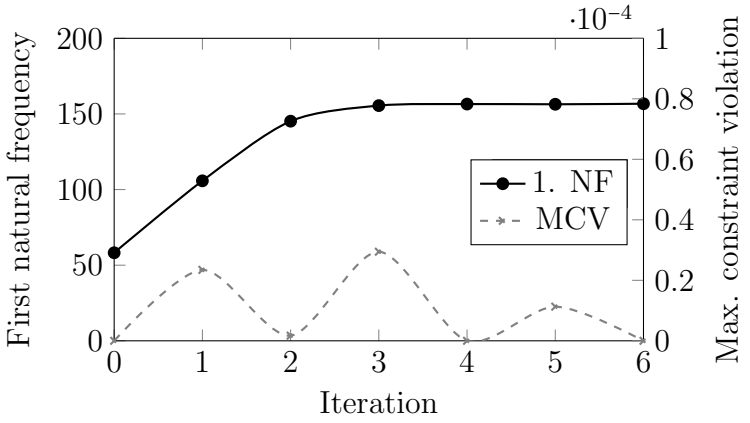

Figure 6.10.: Convergence of the unweighted optimization: First natural frequency (NF) and the maximum constraint violation (MCV).

6.2.2.3. Multi-objective problem statement

At the end of section 6.2.2, the single objective optimization is extended to a multi objective one with equation 6.13, which is repeated here:

$$z = -\sum_{i=1}^{n_{f_e}} f_{e,i}(\mathbf{t_P}) \tag{6.14}$$

The summation of the natural frequencies in equation (6.14) leads to a multi-objective design problem, in which the higher natural frequencies dominate the optimization, as their magnitudes are higher than the ones of the lower natural frequencies. Adding weight factors to the natural frequencies can compensate for this effect. In order to quantify this domination effect for the case of $n_{f_e} = 5$ on an exemplary CFRP disk, the disk is optimized twice: First, with a weight factor of $\xi_i = 1$ for all natural frequencies and second, with adapted weight factors $\xi_i = {}^{f_5}/_{f_i}$ that are calculated by the results of the first optimization in order to normalize the magnitudes of the natural frequencies. The objective function of the second optimization is described with equation (6.15). For both optimizations, a mass constraint of 6 kg and design variables with a limit of 20 mm are chosen.

$$z = -\sum_{i=1}^{5} \xi_i \cdot f_{e,i}(\mathbf{t_P}) \tag{6.15}$$

with

z	...	Objective function
n_{fe}	...	Number of considered natural frequencies
ξ_i	...	Weight factor of i-th natural frequency
$f_{e,i}$	...	i-th natural frequency
$\mathbf{t_P}$	...	Vector of ply thicknesses, i.e. vector of design variables

The results of the comparison of the unweighted to the weighted optimizations shown in table 6.3 indicate that the influence of the weighting is negligible. Due to the weighting, the first natural frequency increases by 0.06 % and the fifth one decreases by 0.25 % compared to the unweighted optimization. Hence, further optimizations are done with a constant weight factor $\xi_i = 1$.

Table 6.3.: Comparison of the unweighted to the weighted optimizations.

$\xi_i = 1$	$\xi_i = \frac{f_5}{f_i}$
$f_{e,1} = 156.7\,\text{Hz}$	$f_{e,1,\xi} = 156.8\,\text{Hz}$
$f_{e,2} = 157.1\,\text{Hz}$	$f_{e,2,\xi} = 157.1\,\text{Hz}$
$f_{e,3} = 167.3\,\text{Hz}$	$f_{e,3,\xi} = 167,3\,\text{Hz}$
$f_{e,4} = 200.1\,\text{Hz}$	$f_{e,4,\xi} = 199.6\,\text{Hz}$
$f_{e,5} = 200.4\,\text{Hz}$	$f_{e,5,\xi} = 199.9\,\text{Hz}$

The summation of the first natural frequencies is necessary to avoid a focusing on one specific shape of an eigenmode. This is illustrated in figure 6.11, where in a.) only the first natural frequency is taken into account in a single objective optimization process. Here, a rib with nearly the maximum thickness of 40 mm appears on the small wing between the cut-outs. The shape of the first eigenmode describes a bending of this small wing. In order to increase the value of this first natural frequency, the wing of the disk gets stiffened with the rib. This is, however, also from the point of view of manufacturing, not a suitable solution. In area b.) in figure 6.11, the sum of the first three natural frequencies is used in the objective function, while it is in area c.) the sum of the first five and in area d.) the sum of the first ten natural frequencies. The calculation is performed without a weight factor. As shown in the previous paragraph, for the first five natural frequencies the influence of the domination of the higher natural frequencies is negligible. In area d.) in figure 6.11, small ribs appear from the center to the outside. Hence, the sum of the first five natural frequencies is used for the following optimization tasks. This solution cannot

be seen as a general one and has to be validated in each optimization task for all different designs of the cut-outs of the disk.

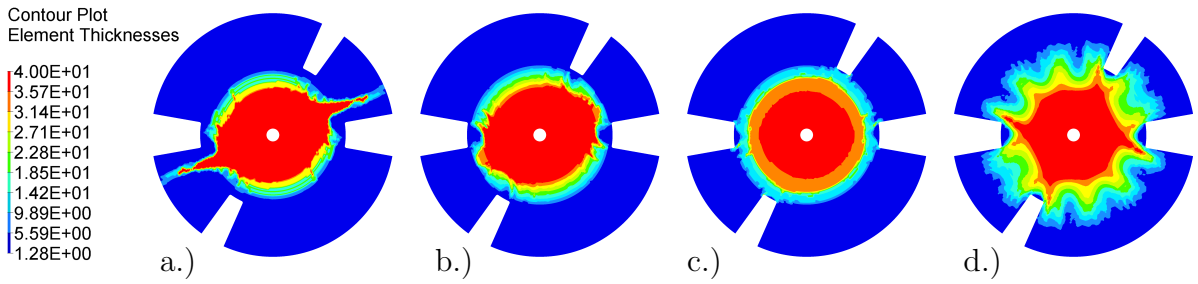

Figure 6.11.: Comparison of the thickness distribution for different optimizations with a variation of n_{f_e}, a.) $n_{f_e} = 1$, b.) $n_{f_e} = 3$, c.) $n_{f_e} = 5$, d.) $n_{f_e} = 10$.

As described in section 4.2.4, the natural frequencies depend on the rotational frequency. To avoid a triggering of the disk by the rotational frequency, it is a conservative approach to design the disk in a way that its first natural frequency in the static case is above the maximum rotational speed during operation. In some cases, this approach is not feasible due to manufacturing or strength constraints. In this particular case, the influence of the rotational speed on the natural frequencies has to be taken into consideration during the numerical optimization process. The optimization formulation taking into consideration the rotational speed is shown in the following equations:

$$\min_{\mathbf{t_P}} \{ z(\omega_{cyc}, \mathbf{t_P}) \mid \mathbf{g}(\mathbf{t_P}) \leq 0 \} \tag{6.16}$$

with

$$z = -\sum_{i=1}^{5} f_{e,\omega_{cyc},i}(\omega_{cyc}, \mathbf{t_P}) \tag{6.17}$$

$$g_1 = \frac{m(\mathbf{t_P})}{m_{max}} - 1 \leq 0 \tag{6.18}$$

$$g_{1+j} = FI_j \cdot N_{SF} - 1 \leq 0 \quad \text{with } j = 1, \ldots, n_{elem} \tag{6.19}$$

with

z	...	Objective function
$f_{e,\omega_{cyc},i}$	...	i-th natural frequency at rotational speed ω_{cyc}
ω_{cyc}	...	Rotational speed
$\mathbf{t_P}$	...	Vector of ply thicknesses, i.e. vector of design variables
$\mathbf{g}$	...	Vector of constraints
m	...	Mass
FI_j	...	Failure index of element j
N_{SF}	...	Safety factor

The results of this optimization are listed in table 6.4. The values are compared to line two in table 6.1 and table 6.2. In the static case, the first natural frequency is increased from 20.4 Hz to 25.4 Hz. In the system rotating at 384 Hz, the first natural frequency is increased from 532.2 Hz to 571.3 Hz. The thickness distribution of this design is shown in figure 6.12. The results in the rotating system show a very high frequency compared to the results in the previous sections. Nevertheless, the values of the natural frequencies in the static case are too low.

Table 6.4.: Comparison of the natural frequencies of the multi objective functions with $n_{f_e} = 5$ in the dynamic and in the static system.

Mode No.	1	2	3	4	5	6	7	8	9	10
Static system [Hz]	25.3	25.4	26.2	26.3	31.7	31.8	47.5	47.6	54.4	54.5
Rotating system [Hz]	571.3	578.4	594.9	608.9	624.7	628.3	648.1	649.0	659.6	660.6

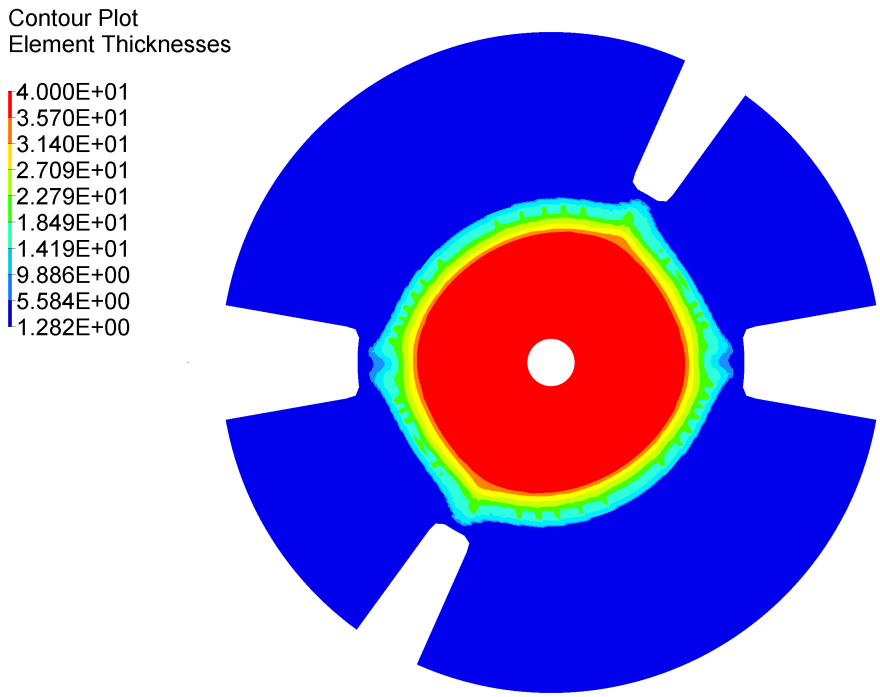

Figure 6.12.: Thickness distribution of a disk, optimized with $n_{f_e} = 5$ for high natural frequencies at a rotational speed of $\omega_{cyc} = 384\,\text{Hz}$.

6.2.2.4. Parameter study with different constraints

The results of the parameter study of the optimization concerning varied maximum thickness constraints and varied maximum mass constraints of the disk are plotted in figure 6.13. The maximum thickness is a constraint of the design space and is chosen in a range from 10 mm to 40 mm. The constraint limits of the mass of the disk are chosen in a range from 2 kg to 9 kg. All combinations of design space variation and mass constraint variation are computed and plotted in the three-dimensional graph of figure 6.13. Here, a ridge is visible, which represents a suitable combination of mass and maximum thickness. For the values in area A, due to higher maximum thickness, little or no increase in natural frequencies is attainable. A high maximum thickness leads to an abrupt change in thickness at the center of the disk, which complicates manufacturing. This can be seen in figure 6.12. The higher mass in area B does not lead to any advantage but makes this disk unnecessarily heavier than the one whose values are shown on the ridge.

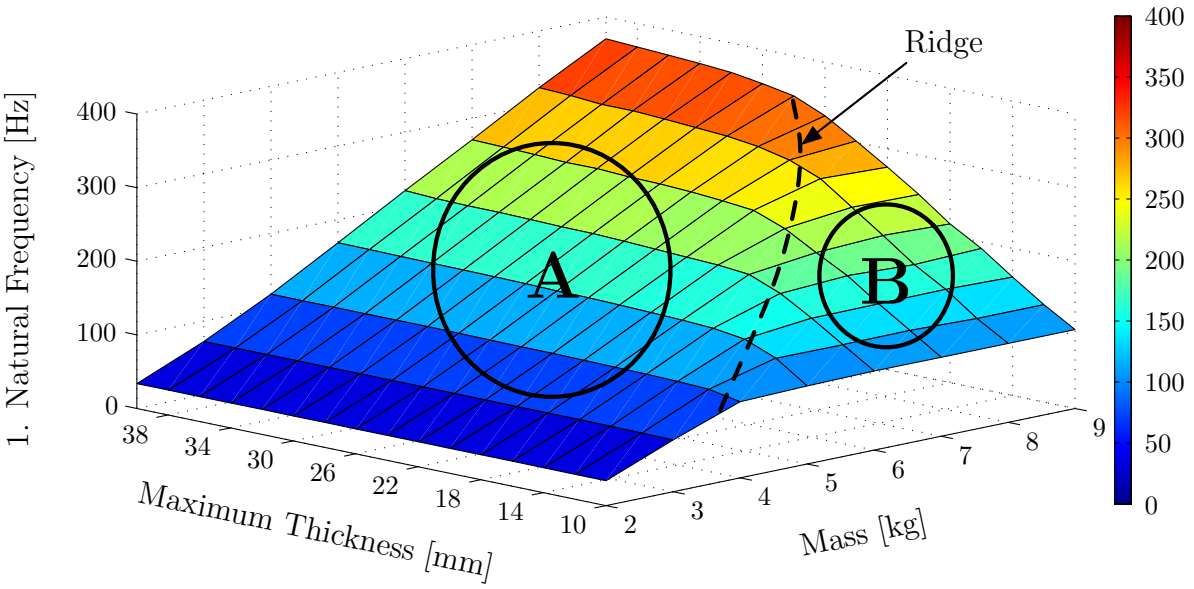

Figure 6.13.: Optimization results for higher natural frequencies with different constraint limits.

6.2.2.5. Parameter study with different material stiffnesses

The calculation series in this section uses varied Young's moduli of the laminate which represents the choice of different materials and carbon fibers. A disk with a maximum mass constraint of 6 kg and a maximum thickness of 20 mm is chosen for the optimizations. A homogeneous quasi-isotropic material is used in the different optimizations. Figure 6.14 shows the results obtained in the different optimizations of the disk concerning the effect of the material stiffness on the natural frequencies of the disk. For each stiffness value, a quasi-isotropic homogeneous disk has been designed through an optimization of the thickness distribution. The plot shows that the stiffness is directly proportional to the natural frequency with a bilinear behavior. For values of the material stiffness higher than 90 GPa, in fact, increasing the stiffness is less effective than it is for lower values. In the rotating system, the same results are obtained.

Between the two boundary values of the Young's modulus, the natural frequency of the static disk increases by 68 %. The values of an intermediate stiffness laminate and a high stiffness laminate are marked with gray areas in figure 6.14. Changing the material from intermediate to high stiffness leads to an increase of the natural frequencies by 19.8 % in the numerical calculation. This value is consistent with the results of the analytical equation 6.20, which is established in detail in chapter 4.2.2:

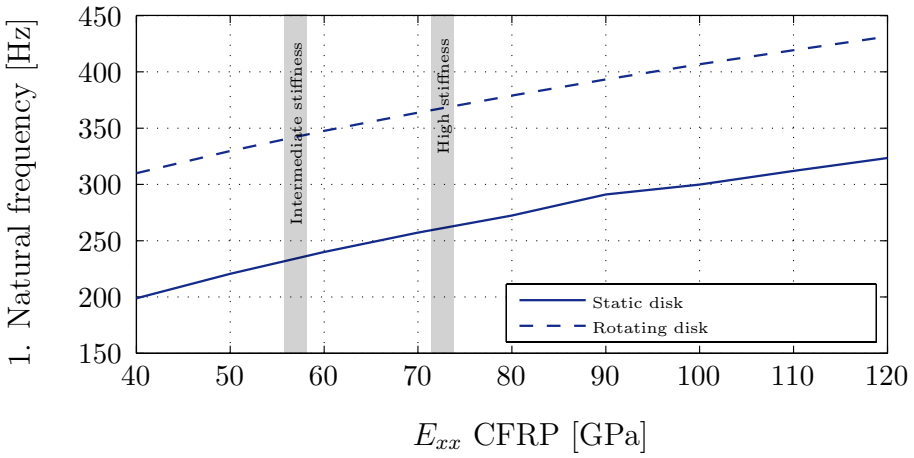

Figure 6.14.: Effect of the material stiffness on the first natural frequency of a disk.

$$f_e = \zeta \cdot \frac{h}{\pi \cdot d^2} \cdot \sqrt{\frac{E}{\varrho}} \tag{6.20}$$

The increase of the first natural frequency gained by changing the material from intermediate stiffness (IS) fibers to high stiffness (HS) fibers can be calculated with the following equation 6.21:

$$\Delta f_e = \sqrt{\frac{E_{HS}}{E_{IS}}} - 1 = 20.2\% \tag{6.21}$$

In equation 6.21, E_{HS} represents the Young's modulus of the high stiffness laminate and E_{IS} represents the Young's modulus of the intermediate stiffness laminate. An equal density of both materials is assumed.

6.2.2.6. Effect of a sandwich design on the natural frequencies

In the present design of the CFRP disks of the TOF experiments, the coating material is placed on the outer diameter of the disks around the cut-outs, as can be seen in chapter 1 in figure 1.2. This coating has a significant influence on the natural frequencies of the disk: high masses on the outer diameter lead to a decrease of the natural frequencies. Furthermore, this mass, due to its poor mechanical properties, does not add any stiffness to the disk. The coating material is a mixture of boron and epoxy. In the case of deep cut-outs, the coating material occupies a large part of the disk and has a substantial influence on the inertial load applied on the structure. In this case, therefore, it is more effective if the boron is placed between the CFRP layers instead of coated on the outside.

With this change in design, the first natural frequency increases by more than 40 %.

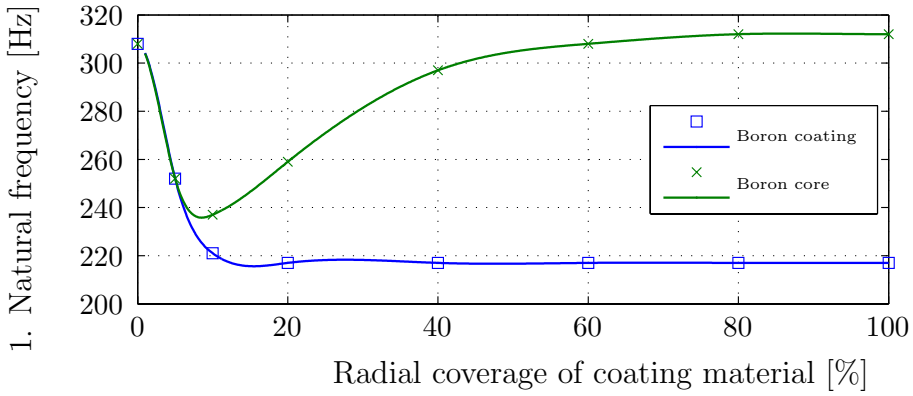

Figure 6.15.: First natural frequency versus radial coverage of the coating material.

Figure 6.15 gives an overview of the procedure described above. For cut-outs that are 15 % of the disk radius, the boron layer as a coating decreases the natural frequencies by 30 %. A boron core is of interest for all disks with a boron coverage higher than 20 % of the disk radius, and is advised for all disks with cut-outs longer than 40 % of the disk radius. This new manufacturing method might be an appropriate procedure to increase the natural frequencies without changing the weight of the disk nor its stiffness properties.

6.2.2.7. Optimal input parameters for the optimization of the structural dynamics

In the previous sections, different parameters of the optimization of CFRP disks for higher natural frequencies have been varied. Some parameters have a clear optimal value. In order to best satisfy the requirements of the manufacturing, a zone based model is the favorite one. Concerning the design space, the use of the maximum thickness of 40 mm is the optimal variant. Yet there is one input parameter which leads to different solutions: The objective function with regard to the natural frequencies in the static system resp. the rotating system. In table 6.1, the results of the first 10 natural frequencies are compared in the static system, and in table 6.2, these first 10 natural frequencies are compared in the rotating system. These calculations are repeated, adding the zone based model and the summation of the first 5 natural frequencies in the objective function. The results of the first 5 natural frequencies are listed below in table 6.5, and the corresponding thickness distributions are plotted in figure 6.16. With regard to the natural frequencies of the rotating system, the first natural frequency increases in the rotating system by 14 % from 510.0 Hz to 581.3 Hz. However, in the static system, the first natural frequency decreases by a factor of 10 from 265.4 Hz to 27.6 Hz. Such a low first natural frequency causes

multiple vibration problems such as coupling modes of the disk and the shaft, which are not considered in this optimization.

Table 6.5.: First 5 natural frequencies of an optimized disk with objective function, which combines $f_{e,i}$ and $f_{e,\omega_{cyc},i}$.

Mode No.	1	2	3	4	5
Static system, $z = -\sum_{i=1}^{5} f_{e,i}$ [Hz]	265.4	269.4	282.4	305.8	329.6
Static system, $z = -\sum_{i=1}^{5} f_{e,\omega_{cyc},i}$ [Hz]	27.6	27.7	28.5	28.6	33.6
Rotating system, $z = -\sum_{i=1}^{5} f_{e,i}$ [Hz]	510.0	525.4	544.6	621.3	649.5
Rotating system, $z = -\sum_{i=1}^{5} f_{e,\omega_{cyc},i}$ [Hz]	581.3	588.7	596.2	612.0	623.3

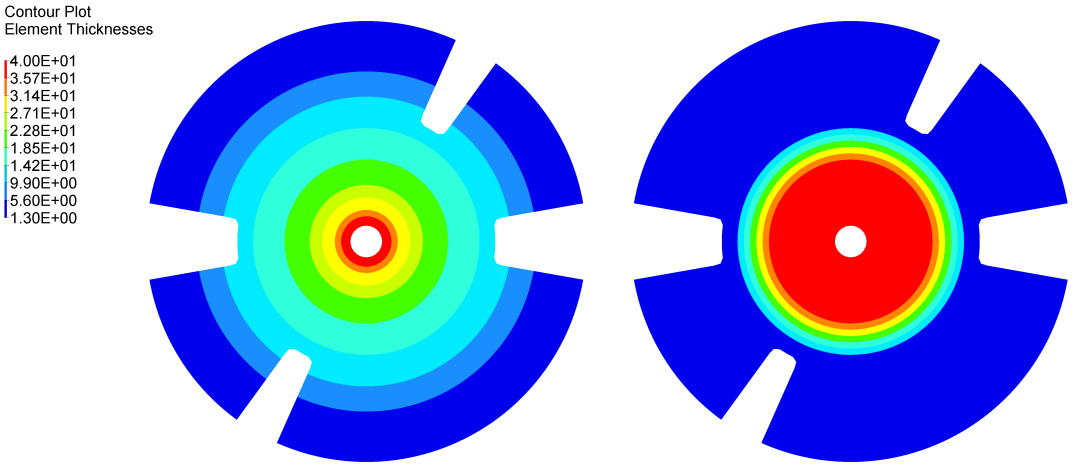

Figure 6.16.: Comparison of the thickness distribution of two disks optimized for higher natural frequencies, left optimized with $z = -\sum_{i=1}^{5} f_{e,i}$ and right with $z = -\sum_{i=1}^{5} f_{e,\omega_{cyc},i}$.

The comparison of the thickness distribution of the two variants described above is shown in figure 6.16. On the left side, the thickness distribution is optimized with $z = -\sum_{i=1}^{5} f_{e,i}$ and on the right side with $z = -\sum_{i=1}^{5} f_{e,\omega_{cyc},i}$. The benefits of the version on the left are the higher natural frequencies in the static case while the benefits of the version on the right are the higher natural frequencies in the rotating system. In order to obtain the advantages from both variants, a new objective function is chosen in the optimization problem and given with equation 6.22.

$$\min_{\mathbf{t_P}}\{z(\omega_{cyc}, \mathbf{t_P}) \mid \mathbf{g}(\mathbf{t_P}) \leq 0\} \tag{6.22}$$

with

$$z = -\sum_{i=1}^{n_{f_e}} f_{e,i}(\mathbf{t_P}) - \sum_{i=1}^{n_{f_e}} f_{e,\omega_{cyc},i}(\omega_{cyc}, \mathbf{t_P}) \tag{6.23}$$

$$g_1 = \frac{m(\mathbf{t_P})}{m_{max}} - 1 \leq 0 \tag{6.24}$$

$$g_{1+j} = FI_j \cdot N_{SF} - 1 \leq 0 \quad \text{with } j = 1, \ldots, n_{elem} \tag{6.25}$$

with

z	...	Objective function
n_{f_e}	...	Number of considered natural frequencies
$f_{e,i}$	...	i-th natural frequency in the static system
$f_{e,\omega_{cyc},i}$	...	i-th natural frequency at rotational speed ω_{cyc}
ω_{cyc}	...	Rotational speed
$\mathbf{t_P}$	...	Vector of ply thicknesses, i.e. vector of design variables
$\mathbf{g}$	...	Vector of constraints
m	...	Mass
FI_j	...	Failure index of element j
N_{SF}	...	Safety factor

The objective function given with equation 6.23 considers both variants: The natural frequencies in the static system and in the rotating system. The other parameters are equal to the previous calculations. A maximum mass constraint of $m_{max} = 6\,\text{kg}$ is chosen and a design space limit of a maximum thickness of $t_{p,max} = 40\,\text{mm}$. The rotational speed of the disk is $\omega_{cyc} = 384\,\text{Hz}$. The optimization is computed twice. First, with $n_{f_e} = 3$, and second with $n_{f_e} = 5$. An exemplary input file of the optimization conducted with Hyperworks Optistruct is given in the appendix in section B.1. The values of the natural frequencies in the rotating system are by ca. factor 2 higher than the values of the natural frequencies in the static system. Without adding a weight factor, as described in section 6.2.2.3, this leads to a domination of the natural frequencies of the rotating system. Nevertheless, this can be considered as a desirable effect. The values of the natural frequencies of the two variants are compared to each other in table 6.6.

The values of both variants are slightly different. In the static system, the values of the variant with $n_{f_e} = 5$ are by 3.2 % higher than those of the variant with $n_{f_e} = 3$. In the

Table 6.6.: First 5 natural frequencies of a disk optimized with optimal input parameters.

Mode No.	1	2	3	4	5
Static system, $n_{f_e} = 3$ [Hz]	243.0	243.8	247.4	251.4	265.4
Static system, $n_{f_e} = 5$ [Hz]	250.7	251.6	256.2	261.4	275.8
Rotating system, $n_{f_e} = 3$ [Hz]	572.9	574.6	596.4	643.6	667.5
Rotating system, $n_{f_e} = 5$ [Hz]	565.3	569.2	591.0	642.7	667.6

rotating system, it is the other way around. Here, the values of the variant with $n_{f_e} = 3$ are by 1.3 % higher than those of the variant with $n_{f_e} = 5$. The thickness distributions of both variants are plotted in figure 6.17. In the variant with $n_{f_e} = 3$, the area with the maximum thickness of 40 mm is slightly larger than the one of the variant with $n_{f_e} = 5$. The gradient of the thickness distribution is slightly lower in the variant with $n_{f_e} = 3$. To summarize, the optimization with the objective function which combines the natural frequencies of the static and the rotating system, leads to the best results of this optimization approach. As the favorite, the variant with $n_{f_e} = 3$ is chosen due to the higher natural frequencies in the rotating system.

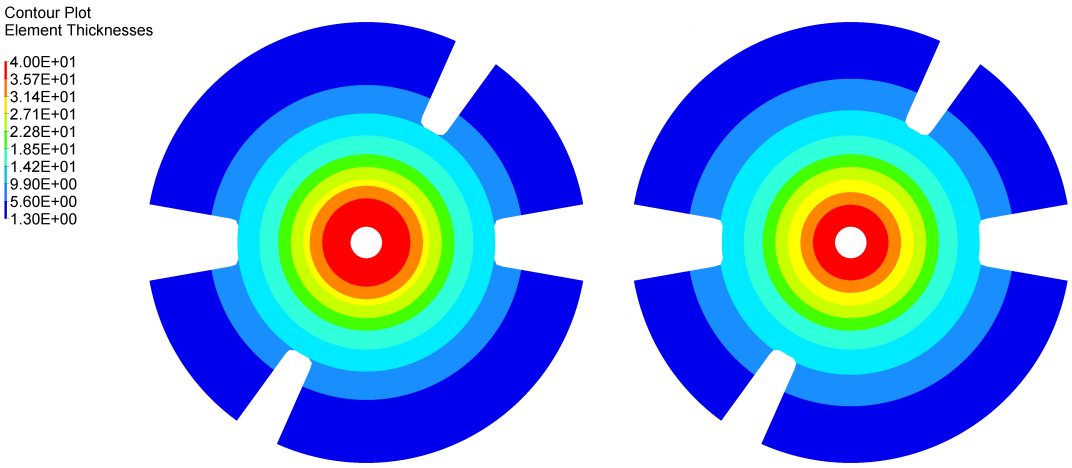

Figure 6.17.: Thickness distribution of a disk, optimized with optimal input parameters, left with $n_{f_e} = 3$ and right with $n_{f_e} = 5$.

6.2.3. Limitation of the widening of the central through-hole of CFRP disks

The radial widening around the central through-hole, caused by the centrifugal forces, can lead to the hub detaching itself from the disk. Thus, with higher rotational speeds, the preload of the cold pressing-in becomes lower. With a numerical optimization approach, the thickness of the disk is optimized for a minimal radial displacement around the through-hole. The following optimization approach minimizes the radial displacement of the element nodes n_{cn} during operational speed while taking into account a mass constraint as well as the maximum-strain failure criterion $\varepsilon_{\max,emp} = 1.27\,\%$ multiplied with a safety factor of $N_{SF} = 1.2$ due to uncertainty in load. As an additional constraint, the first natural frequency of the disk has to be higher than the rotational speed, as shown in equation (6.29).

$$\min_{\mathbf{t_P}} \{ z(\omega_{cyc}, \mathbf{t_P}) \mid \mathbf{g}(\omega_{cyc}, \mathbf{t_P}) \leq 0 \} \tag{6.26}$$

with

$$z = \sum_{i=1}^{n_{cn}} u_{r,i}(\omega_{cyc}, \mathbf{t_P}) \tag{6.27}$$

$$g_1 = \frac{m(\mathbf{t_P})}{m_{max}} - 1 \leq 0 \tag{6.28}$$

$$g_2 = \frac{f_{e,1}(\omega_{cyc}, \mathbf{t_P})}{\omega_{cyc}} - 1 \leq 0 \tag{6.29}$$

$$g_{2+j} = FI_j(\omega_{cyc}, \mathbf{t_P}) \cdot N_{SF} - 1 \leq 0 \quad \text{with } j = 1, \ldots, n_{elem} \tag{6.30}$$

with

z	...	Objective function
n_{cn}	...	Set of nodes around the central through-hole of a disk
$u_{r,i}$	...	Radial displacement of node i
ω_{cyc}	...	Rotational speed
$\mathbf{t_P}$	...	Vector of ply thicknesses, i.e. vector of design variables
m	...	Mass
$\mathbf{g}$	...	Vector of constraints
m	...	Mass
$f_{e,1}$	...	First natural frequency
FI_j	...	Failure index of element j
N_{SF}	...	Safety factor

Table 6.7.: Overview of the responses of the optimal design.

Responses	Value
Radial displacement u_r	102.8 μm
Total mass m	4.8 kg
Smallest natural frequency $\min\{f_i\}$	391.3 Hz

The result of this optimization with a mass constraint of m_{max} = 6 kg and a maximum thickness of the disk of 40 mm is shown in figure 6.18. The rotational speed is ω_{cyc} = 350 Hz. An abrupt change in thickness occurs at around 40 % of the radius, which is consistent with the analytical prediction as given with figure 6.2. An additional thickness of the disk leads to a higher stiffness as well as a higher mass, which results in higher centrifugal forces. Up to a certain radius, it is advantageous to have a higher thickness, as the stiffening dominates the higher centrifugal forces. This explains the sharp decrease in thickness.

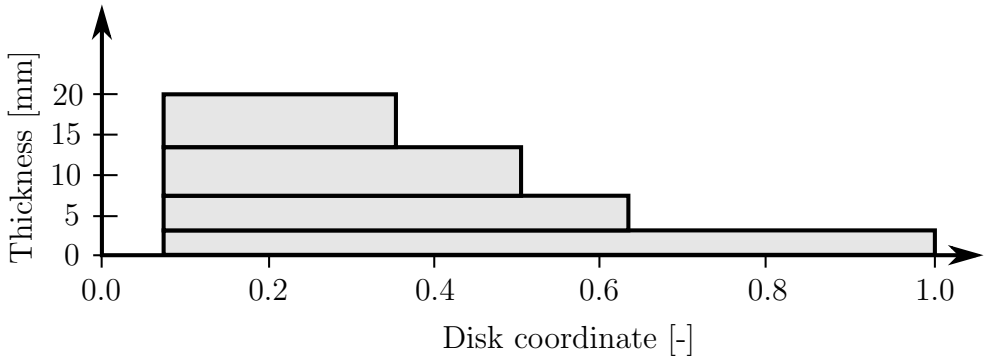

Figure 6.18.: Thickness distribution of the half-section of the disk after optimization for lower radial displacement.

The optimization described in the previous passage is conducted with a discretization of 4 steps in thickness direction. This leads to an abrupt change in thickness at disk coordinates 0.36, 0.51 and 0.64. In order to achieve a better accordance with the analytical results shown in section 6.1, a second FEM model with a thickness discretization of a multiple of the thickness of eight plies with the layup $[0/45/90/\text{-}45]_s$ is created. The results of the second model of the numerical optimization for lower radial displacement at the central through-hole are shown in figure 6.19. At a discreet radius r_E, there is a jump in the thickness distribution from 40 mm to 18 mm. For $r < r_E$, it is beneficial to thicken the disk. Additional layers placed in this area lead to less widening of the through-hole. For

$r > r_E$, it is unprofitable to add additional layers due to the fact that the additional weight of the added layers leads to higher centrifugal forces and more widening of the central through-hole [147]. In order to get a better comparison to the analytical results, there are no constraints concerning the natural frequencies in this optimization. The value of r_E is influenced by the density and the Young's modulus of the material. For a lower density and a higher Young's modulus, r_E gets shifted to higher values. The thickness distribution shown in figure 6.19 is the result of the optimization of the CFRP disk with $r_E \approx 80\,\text{mm}$. The material used is M30SC with a Young's modulus of $E_{xx} = 54\,000\,\text{MPa}$ and a density of $\varrho = 1.52\,{}^{g}/_{\text{cm}^3}$.

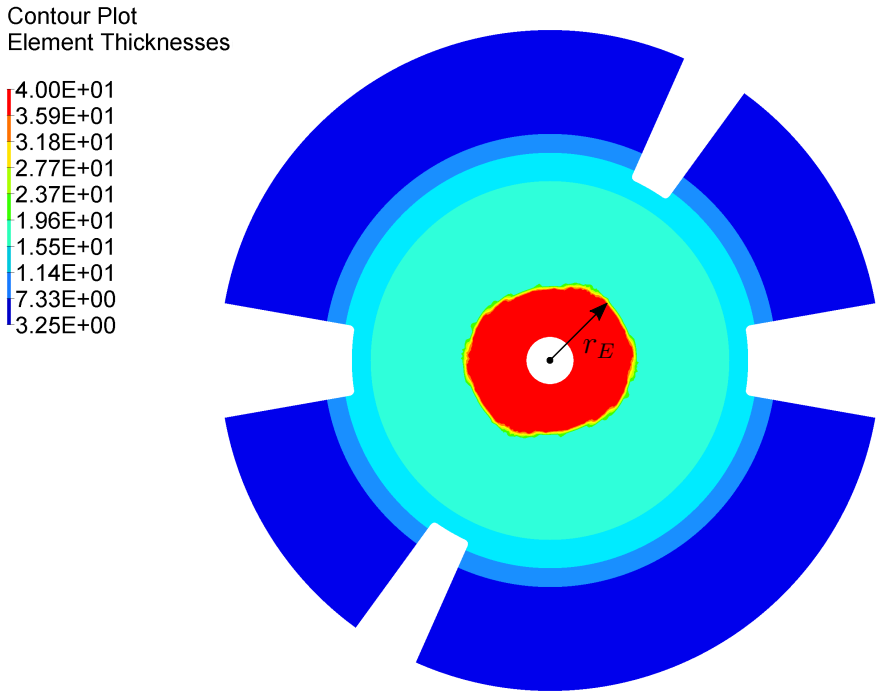

Figure 6.19.: Optimized thickness distribution for lower radial displacement at the central through-hole [147].

6.2.4. Optimization of the shapes of the cut-outs

After performing multiple stress analyses, the cut-outs and especially their bottom shapes can be identified to be among the most critical areas in terms of sensitivity to stress overshoots and thus in terms of being sensitive to initial failure. So as to mitigate those stress overshoots, an optimization task with the following set of equations is defined and subsequently solved to find an optimal cut-out shape [2, 15, 19, 62, 63, 85].

$$\min_{\mathbf{x_S}} \max\{\mathbf{z}(\omega_{cyc}, \mathbf{x_S}) \mid \mathbf{g}(\omega_{cyc}, \mathbf{x_S}) \leq 0\} \tag{6.31}$$

with

$$z_j = FI_j(\omega_{cyc}, \mathbf{x_S}) \quad \text{with } j = 1, \ldots, n_{elem} \tag{6.32}$$

$$g_1 = \frac{m(\mathbf{x_S})}{m_{max}} - 1 \leq 0 \tag{6.33}$$

$$g_2 = \frac{f_{e,1}(\omega_{cyc}, \mathbf{x_S})}{\omega_{cyc}} - 1 \leq 0 \tag{6.34}$$

with

$\mathbf{z}$	...	Vector of objective functions
FI_j	...	Failure index of element j
ω_{cyc}	...	Rotational speed
$\mathbf{x_S}$	...	Shape variables, i.e. $\Omega(\mathbf{x_S}) = \Omega(\mathbf{x_0}) + \sum_k \mathbf{b}_k x_{S,k}$
$\mathbf{g}$	...	Vector of constraints
m	...	Mass
$f_{e,1}$	...	First natural frequency
$\Omega(\mathbf{x_S})$	...	Domain of the shape variables
$\mathbf{b}_k$	...	Base vector

In figure 6.20, a sketch of the optimization equation is shown. For the optimization, a quarter model of the disk is used with symmetric boundary conditions. The blue line shows the shape of the cut-out defined by the base vectors $\mathbf{b}_k$ multiplied by the shape variables $\mathbf{x_S}$.

The optimization task as specified with equation (6.31) represents a min - max problem defined in such a way that the maximum failure index is being minimized whilst all constraints keep being taken into consideration. The failure index is caused by the high centrifugal forces and is evidently sensitive to the shape of the cut-out. The Tsai-Wu failure criterion is used with the material parameters of table 5.2. In equation (6.33), a

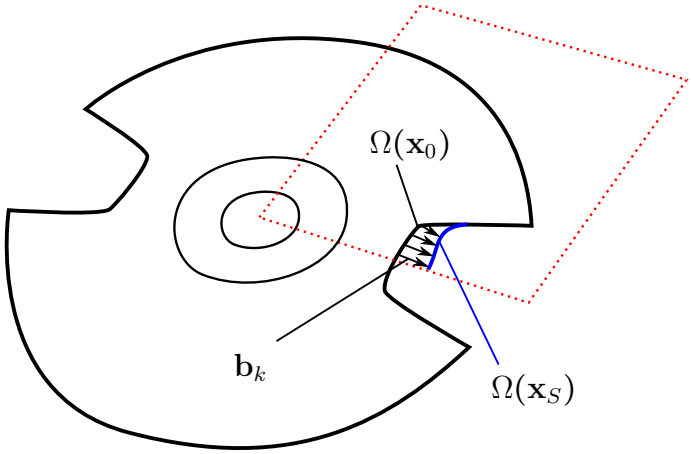

Figure 6.20.: Sketch of shape optimization with the shape domain $\Omega(\mathbf{x_S})$.

mass constraint is determined and in equation (6.34), a constraint of the first natural frequency being higher than the rotational speed is defined.

With figure 6.21, the result of an optimization with a mass constraint of $m_{max} = 6\,\text{kg}$ is given. The rotational speed which is considered in the optimization, is $\omega_{cyc} = 380\,\text{Hz}$. It can be seen that the failure index, which is a measure for initial composite failure, has been reduced from 1.8 to 0.9. This reduction is remarkable, since the optimization has notably reduced the stress overshoots and has thereby realized a transition from a highly failure-prone design to a feasible one. This latter, feasible design comprising a change in shape from the initial design is given with the zoom in figure 6.22.

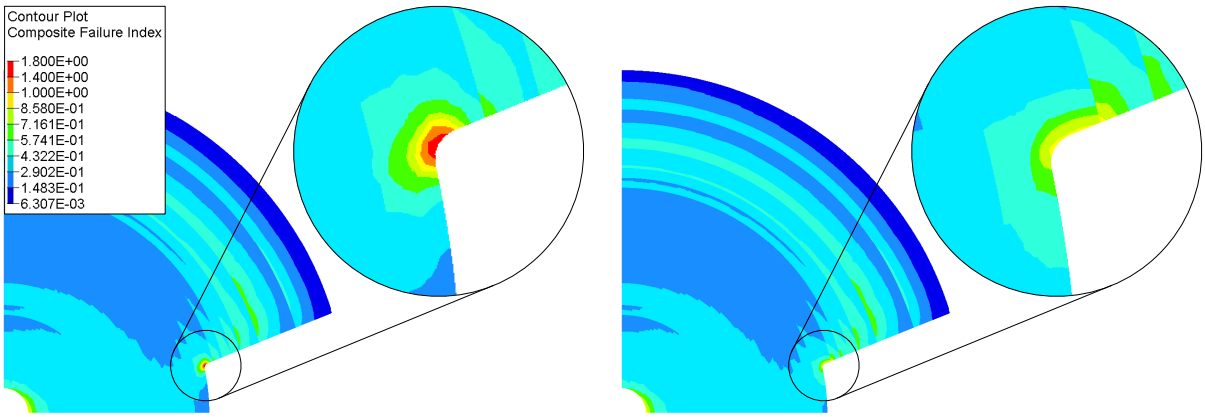

Figure 6.21.: Left: Failure index original design, Right: Failure index optimized design.

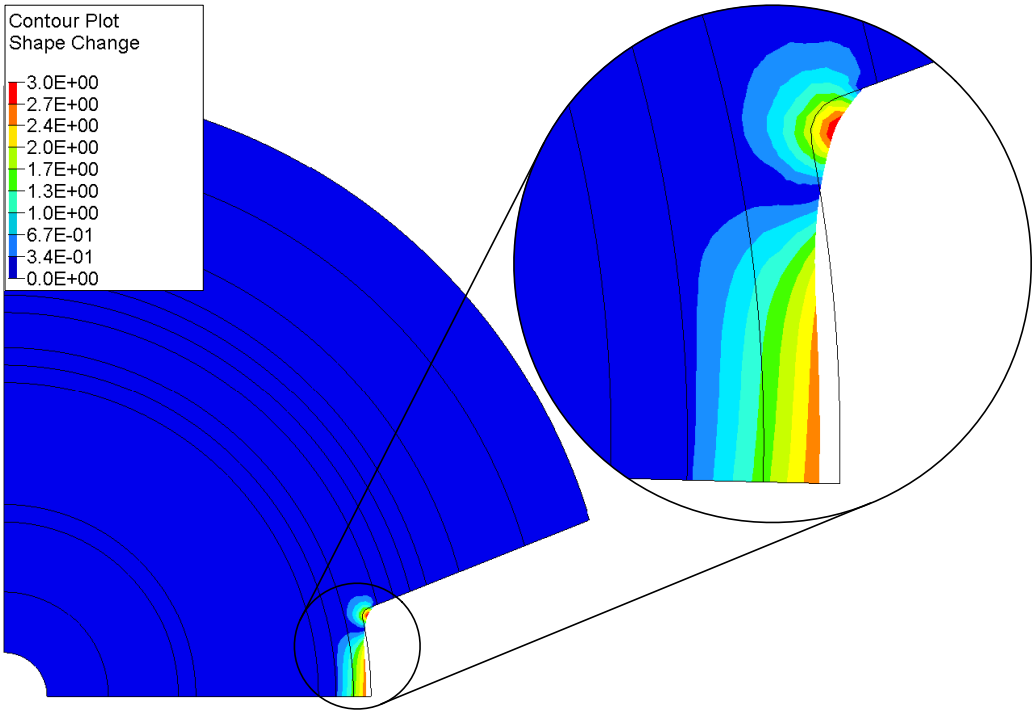

Figure 6.22.: Change of the shape of the cut-outs after optimization for lower failure index.

6.3. Numerical optimization of the hub of a CFRP disk

In the previous sections, an optimization of the CFRP disk itself has been described. To achieve higher rotational speeds and more stable disks, a holistic approach has to be made, considering the disk as well as the hub and the shaft. A significant interface is the one between the CFRP disk and the aluminum hub. During operation of the CFRP disks, the central through-hole widens due to centrifugal forces. The amount of the widening depends on the following parameters:

- rotational speed
- geometrical dimensions of the disk
- diameter of the central through-hole
- stiffness of the disk

A typical diameter of the central through-hole of a CFRP disk is between 50 mm and 75 mm. This through-hole of an exemplary disk with a central through-hole of 50 mm widens between 0.15 mm to 0.4 mm at a rotational speed of 350 Hz, which is equivalent to a strain of 0.3 % to 0.8 %. These strain values are above the maximum strain of high strength aluminum, which is 0.5 % to 0.6 %. In the following section, a new solution approach for such a disk-hub connection is presented [29, 113, 140, 142, 143].

6.3.1. Connection between an aluminum hub and a fiber-reinforced disk

The main task of a shaft-hub connection is the transmission of rotation and torque from the shaft to the hub. There are four main shaft-hub connections in literature [91]:

- friction joint
- positive fit joint
- prestressed positive fit joint
- adhesive joint

Below, the friction joint is treated in more detail. A friction joint is beneficial for fiber composite structures due to its reduction of stress peaks compared with positive fit joints. The central part of the disk, which is the area around the central through-hole for the hub, is highly stressed due to the centrifugal forces during rotation. A positive fit joint

adds additional stress to this area. To compensate for this additional stress, the disk has to be thickened, which leads to a higher mass and higher centrifugal forces. Therefore, only friction joints are investigated in the next steps.

The force of friction F_f at the lateral surface is defined by the normal force F_n and the coefficient of adhesion μ resp. the safety against gliding S_g:

$$F_f = F_n \mu = \frac{F_n}{S_g} \tag{6.35}$$

In a clamping connection, the normal force is generated by prestressed bolts, which leads to a non-uniform distribution of the normal force. In this case, the hub is slotted or parted [91]. The nomenclature of the shaft-hub connection for the system consisting of a disk and a hub is different to standard literature. In standard literature, the shaft-hub connection consists of a shaft, which is the inner part, and a hub, which is the outer part. The hub is clamped or pressed onto the shaft, which leads to an interference fit. The system described further on this thesis consists of a disk and a hub with the hub being the inner part, which is pressed into the disk, and the disk being the outer part. The connection between the hub and the drive shaft will not be mentioned furthermore, because it is a standard connection in mechanical engineering which causes no problems.

In general, the joint pressure of an interference fit is defined by the normal force F_n and the lateral surface A:

$$p_j = \frac{F_n}{A} \tag{6.36}$$

The lateral surface A of the central through-hole is defined by the joint diameter d_j and the length of the joint l_j:

$$A = \pi d_j l_j \tag{6.37}$$

Thereby, the maximum torque that can be transmitted by the friction fit connection considering a safety factor S_g is:

$$\tau = \frac{\pi p_j}{2 S_g} d_j^2 l_j \mu \tag{6.38}$$

In a cylindrical interference fit, the joint pressure needed for the torque transmission depends on the deformation of the hub and the disk. The outer diameter of the hub is larger than the inner diameter of the disk. After pressing the hub into the disk, this oversize of the hub generates the joint pressure. During operation, the shaft-hub connection is exposed to temperature influences and centrifugal forces. In the design process of the

interference fit, the oversize has to be calculated. The joining as well as the yield point of the material have to be taken into consideration.

6.3.2. Constraints of the numerical optimization of the disk-hub connection

For the numerical optimization of the hub, a model is chosen which is similar to the one of the CFRP disk described in the previous section. It has two areas: A non-design space around the inner diameter, which is colored gray in figure 6.23 and a design space, which is colored blue. The geometrical parameters of the disk-hub connection are listed in table 6.8. The non-design space is used for the mounting of the hub onto the shaft.

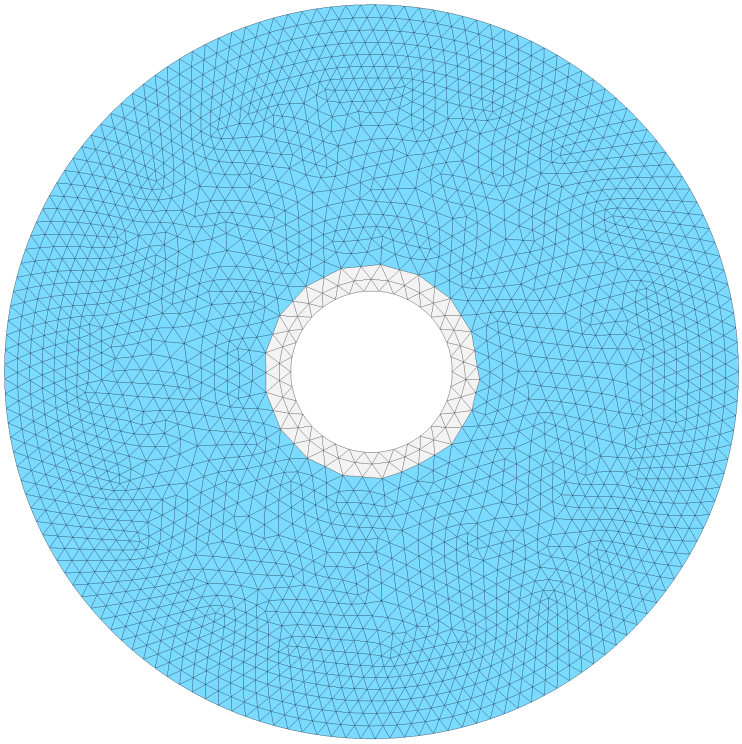

Figure 6.23.: FE model for the numerical topology optimization of the hub.

The FE model of the hub is composed of 4 715 triangle elements of the second order (CTRIA6). In contrast to the model of the CFRP disk, the outer shape of the structure is not defined at the beginning of the optimization process. In the optimization of the CFRP disk, only the thickness of defined zones is adopted while in the optimization of the hub,

Table 6.8.: Geometry parameters of the disk-hub connection.

Outer diameter of the hub	$d_{o,hub} = 50\,\text{mm}$
Inner diameter of the hub	$d_{i,hub} = 11\,\text{mm}$
Length of the hub	$l_j = 30\,\text{mm}$

the geometrical shape has to be generated. Therefore, for the hub a topology optimization is performed in contrast to the free-size optimization of the CFRP disk [37, 74, 117]. The material of the hub is high strength aluminum AL7075. The material properties are listed in table 6.9. An exemplary input file of the optimization conducted with Hyperworks Optistruct is given in the appendix in section B.2.

Table 6.9.: Material properties aluminum AL7075.

$E\,[\text{MPa}]$	$G\,[\text{MPa}]$	$\nu\,[-]$	$R_m\,[\text{MPa}]$	$\tau_m\,[\text{MPa}]$	$\alpha \cdot 10^{-6}\left[\frac{1}{\text{K}}\right]$	$\varrho\left[\frac{\text{g}}{\text{cm}^3}\right]$
73 000	26 200	0.33	505	305	23.4	2.80

6.3.3. Optimization of the hub under an additional temperature load

To achieve a cylindrical interference fit, the most simple variant is a full aluminum hub with a defined oversize. Using the thermal expansion coefficient of the material, the hub can be cooled down, for example with liquid nitrogen, and afterwards mounted into the disk. This solution is suitable as long as the widening of the central through-hole of the disk is smaller than the maximal strain of the aluminum. For example, for a radial widening of 0.2 mm at a radius of 25 mm, which corresponds to 0.8 % strain, a full aluminum hub will show a plastic deformation and the connection will detach itself at a rotational speed below the operational one.

For deformations as described in this example, a geometrical solution of the widening of the hub is necessary. In order to find suitable designs, different topology optimizations are shown below. One possibility is the optimization of the structure contraction at a defined temperature difference. The optimization problem is given with equation 6.39.

$$\min_{\boldsymbol{\rho_e}}\{z(T,\boldsymbol{\rho_e}) \mid \mathbf{g}(T,\boldsymbol{\rho_e}) \leq 0\} \tag{6.39}$$

with

$$z = -\sum_{i=1}^{n_{on}} u_{r,i}(T,\boldsymbol{\rho_e}) \quad \text{with } i = 1,\ldots,n_{on} \tag{6.40}$$

$$g_1 = \frac{V(\boldsymbol{\rho_e})}{V_{max}} - 1 \leq 0 \tag{6.41}$$

$$g_{1+j} = FI_j(T,\boldsymbol{\rho_e}) \cdot N_{SF} - 1 \leq 0 \quad \text{with } j = 1,\ldots,n_{elem} \tag{6.42}$$

with

z	...	Objective function
n_{on}	...	Set of nodes at the outer diameter of the hub
$u_{r,i}$	...	Radial displacement of node i
T	...	Temperature
$\boldsymbol{\rho_e}$	...	Vector of element density, i.e. vector of design variables
$\mathbf{g}$	...	Vector of constraints
V	...	Volume
FI_j	...	Failure index of element j
N_{SF}	...	Safety factor

The result of the optimization shows a structure which is comparable to a wheel spoke. A plot of the element density of the design hub is shown on the left side in figure 6.24 while the corresponding field of displacement of the new structure after an equalization is shown on the right side. In the following section 6.3.4, the results are discussed and a new design of a hub based on the optimization results, is presented.

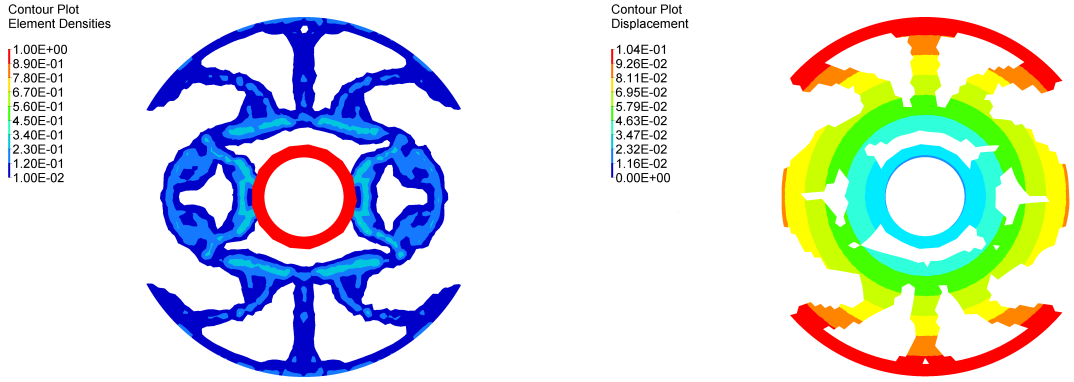

(a) (b)

Figure 6.24.: Optimized hub under an additional temperature load, (a) element density after optimization, (b) field of the radial displacement at $\Delta T = 180\,\mathrm{K}$.

6.3.4. Discussion of the results of the contact analysis of the optimized hub

With the preliminary contemplations on optimization made in the previous section, a new design of the hub is realized. This new approach with large chambers and a single curved outer surface area has improved and optimized the final design. The performance of the new hub design is evaluated by means of non-linear contact analyses. The corresponding FE model is shown in figure 6.25. The major improvement of the new hub design is the decrease of the stresses and the increase of the radial widening compared to the initial design. No plasticity is encountered up to a rotational frequency of 500 Hz. The critical stresses occur at the small radius of the chamber surfaces. Figure 6.26 shows a plot of the stress distribution of the new hub design. Hubs with a thinner cross section exhibit lower stress values. Concerning the second criterion, the contact behavior, the performance of the new hub design has been increased.

Figure 5.6 shows the initial contact pressure on the bearing surfaces after pressing the hub into the central through-hole of the disk. It can be seen that only the edges of the chamber surfaces are in contact. Figure 6.27 shows the contact pressure on the bearing surfaces at a rotational frequency of 500 Hz with a soft and a stiff modeling of the tungsten weights. Only the areas with a pressure greater than 1 MPa are highlighted. The remaining area, plotted in gray, can be supposed not to be in contact any more at a rotational frequency of 500 Hz. The new hub design is manufactured with wire cutting and tested in detail. The results of the test are presented in chapter 7.2.2.

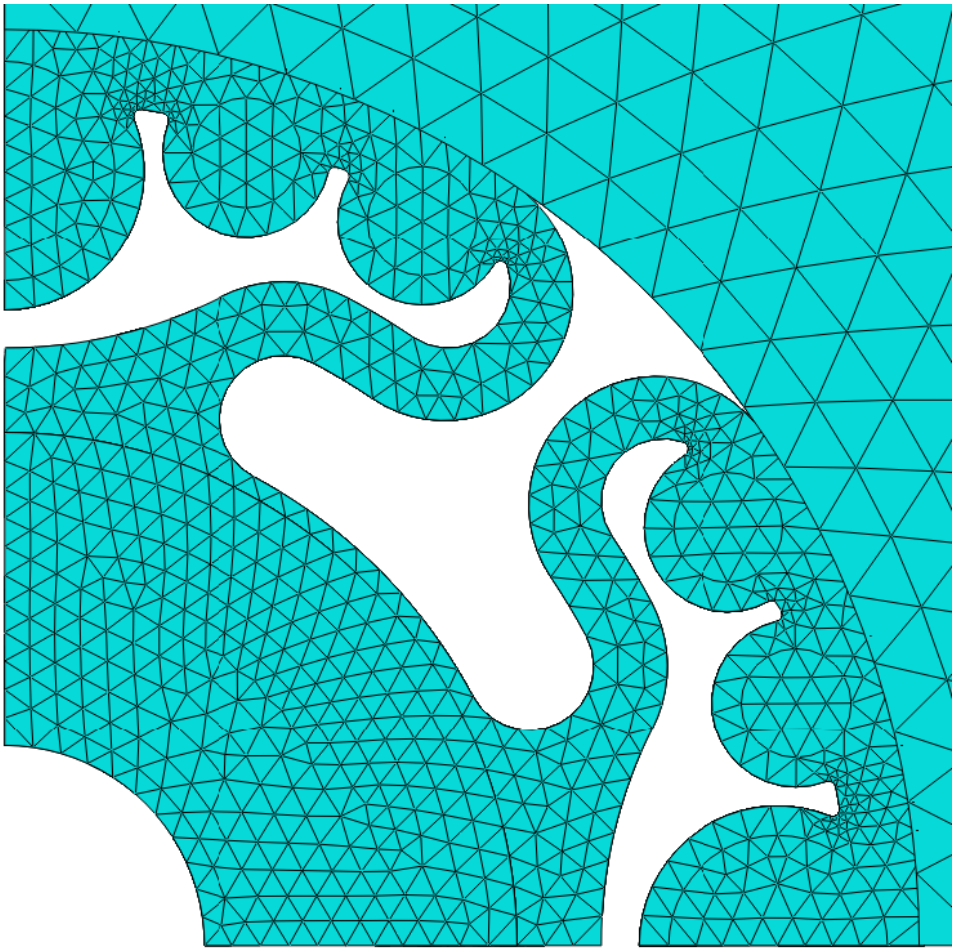

Figure 6.25.: Finite element model of the new hub and the disk in the contact area.

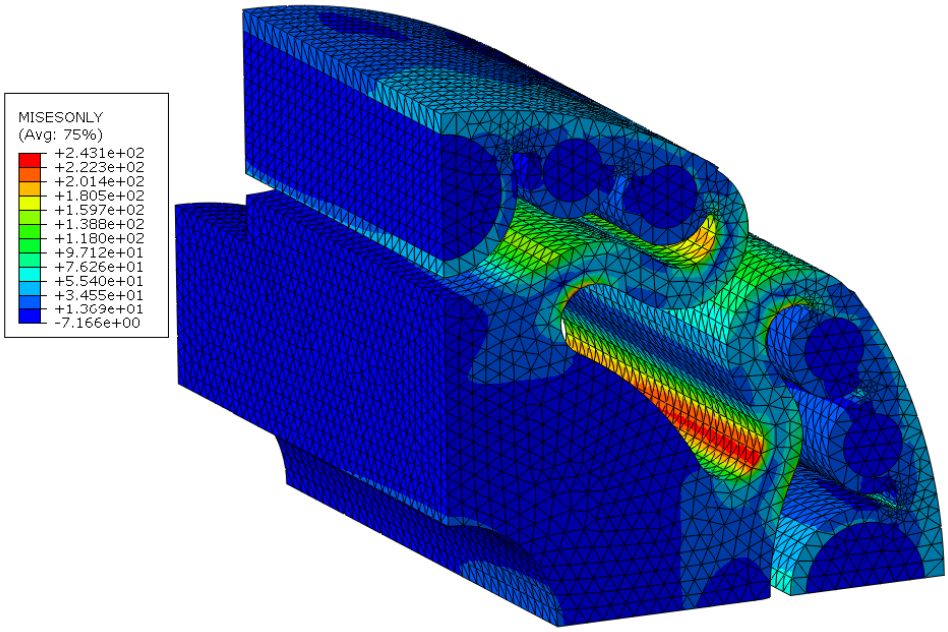

Figure 6.26.: Stress distribution in the hub at a rotational frequency of 500 Hz.

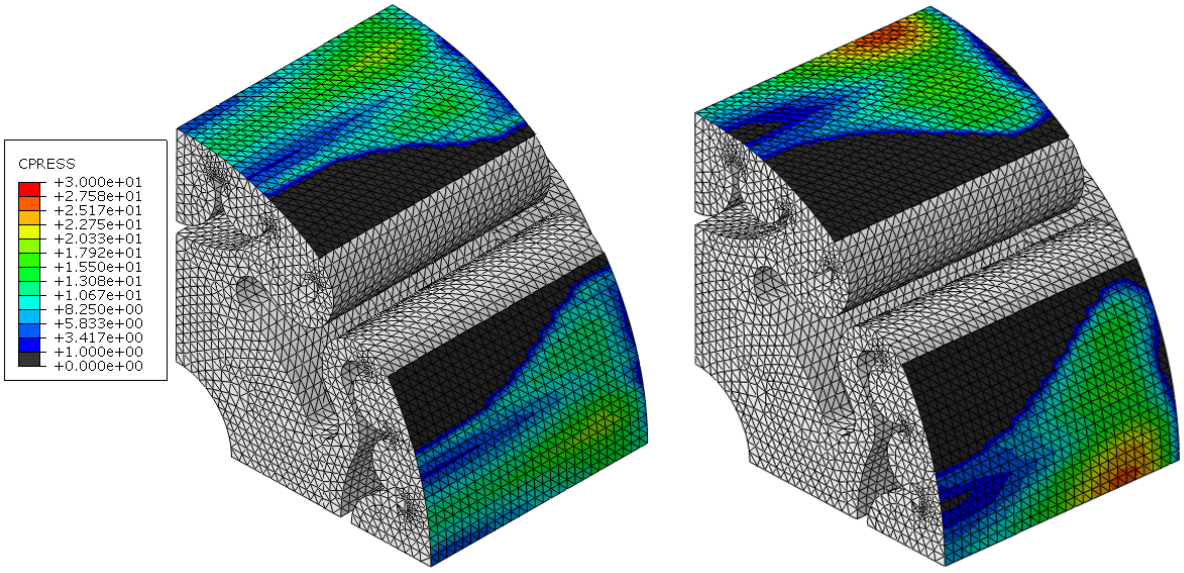

Figure 6.27.: Contact pressure between disk and hub at a rotational frequency of 500 Hz, (left) with a soft tungsten modeling and (right) with a stiff tungsten modeling.

7

Experimental measurement and testing of CFRP disks

In this chapter, experimental measurements of CFRP disks are presented. Firstly, a detailed description of the measurement of natural frequencies and eigenmodes of various disks is given. Secondly, several spinning tests of disks in an overspeed test stand are described and results for the stiffness and the strength of the disks are given. Both, the measurements of the natural frequencies and the spinning tests are performed with disks of an equal design in order to allow for a comparison of the calculation and the measurement.

Contents

7.1. Measurement of natural frequencies and eigenmodes

For a verification of the FEM calculation of the natural frequencies in chapter 5, the first prototype CFRP disk of the project NEAT is chosen. A draft of the disk including its dimensions is given in the appendix A.1. For this verification, the natural frequencies of the disk are measured using a bump test in which the disk gets treated with a hammer. In the left side (a) of figure 7.1, the experimental setup is shown. In the right side (b) of figure 7.1, a photograph of the acceleration sensor is shown.

(a) (b)

Figure 7.1.: Test setup of the measurement of the natural frequencies of a CFRP disk, (a) Chopper disk NEAT C1 with four acceleration sensors, (b) detailed view of an acceleration sensor.

The measurement is conducted in two different configurations. The first configuration comprises the CFRP disk and the hub. The hub is clamped to a massive test stand, which is considered to be a rigid body. This configuration allows for a good comparability to the FEM calculations, as these calculations are usually performed with disk and hub. In this configuration, the system boundary is precisely defined to be between the hub and the rigid test stand.

The second configuration is a measurement of the natural frequencies of the disk, which is mounted into the overspeed test stand. The overspeed test stand is described in detail in the following section 7.2. This configuration comprises the disk, the hub and the shaft as well as the bearing of the shaft and the overspeed test stand itself. In this configuration, the system boundary is not precisely defined. The overspeed test stand itself represents a high mass but is not considered to be a rigid body. The damping bearings of the shaft are pressurized with oil. The FE modeling of such bearings causes uncertainties which make a comparison of the measured and the calculated values imprecise. However, the measured

values of the static natural frequencies can be compared with the resonance frequencies during the spinning tests.

The results of both configurations of the measurement of the natural frequencies are given in the following subsections 7.1.1 and 7.1.2.

7.1.1. Natural frequencies of the disk and the hub

The hub of the disk is clamped at its front and back side to the rigid test stand. The acceleration sensors are located on the edge of the disk. Sensors 1 and 2 are placed on the larger area between the cut-outs, and sensors 3 and 4 are placed on the smaller area. Sensors 1 and 3 are placed near to the cut-outs while sensors 2 and 4 are placed at the midpoint between two cut-outs. The positioning of the sensors is shown in the draft in figure 7.2.

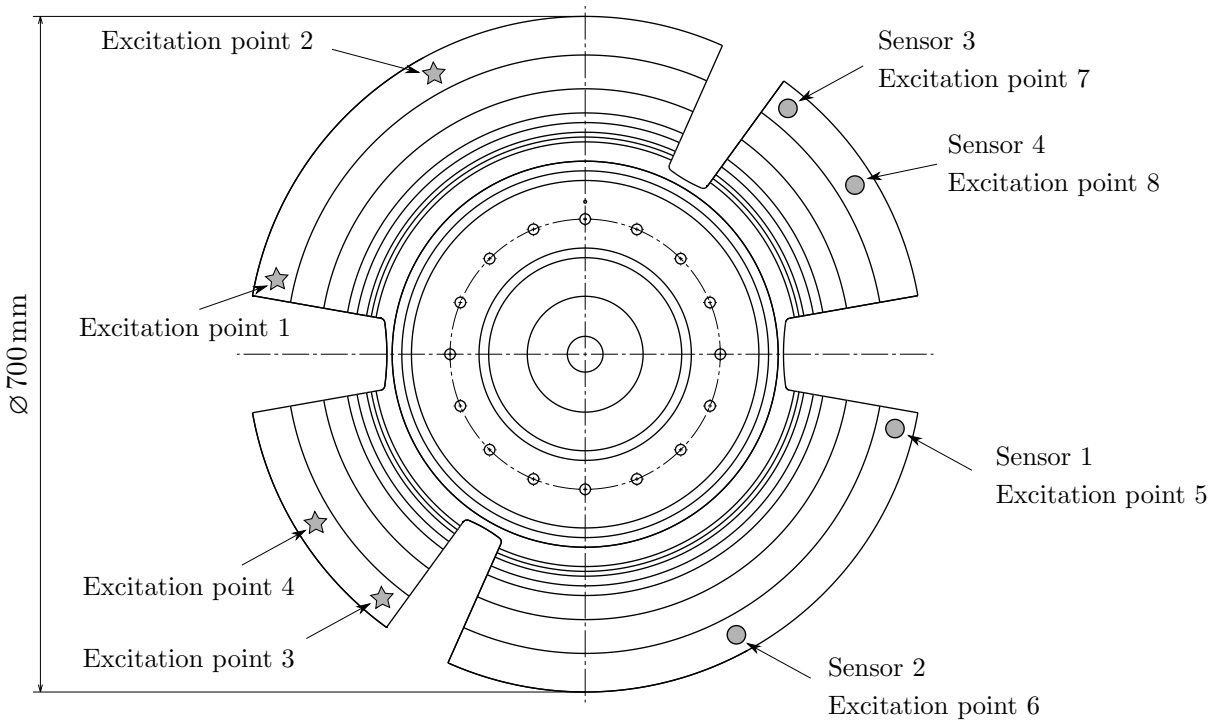

Figure 7.2.: Positions of the acceleration sensors on the disk.

The results of the first measurement are plotted in diagram 7.3. The first six natural frequencies are in a range from 209 Hz to 279 Hz and are listed in table 7.1 for all eight measurements. The measurements differ in the excitation point of the hammer. In measurement no. 1 the disk is triggered with the hammer on excitation point 1. Excitation

point 1 is precisely across from sensor 1 on the disk. During measurement no. 2, the disk gets triggered on excitation point 2 and so forth. During measurements no. 5 to no. 8, the disk is triggered on the sensors itself: The excitation point of measurement no. 5 is onto sensor 1, the excitation point of measurement no. 6 is onto sensor 2 and so forth.

The results of the first three natural frequencies match with the calculated ones. The deviation of the numerically calculated natural frequency from the one measured is around 6 %, which can be regarded as a satisfactory value. The deviation of the calculation from the measured values of the subsequent natural frequencies is around 17 %.

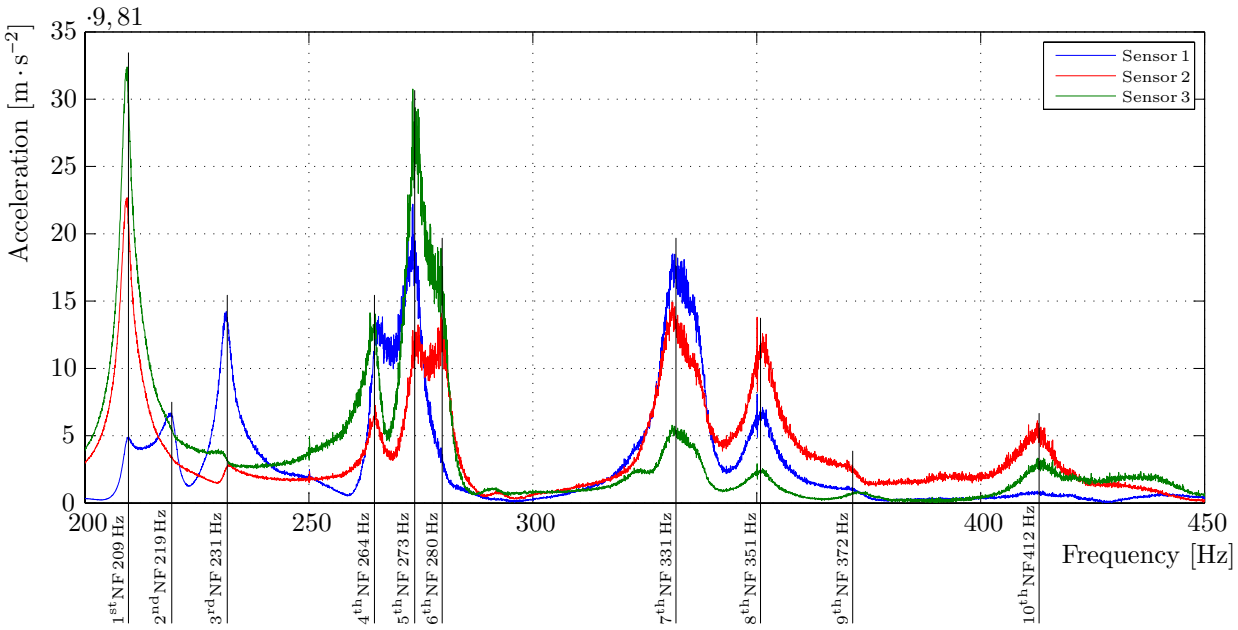

Figure 7.3.: Measurement results of the natural frequencies of the NEAT C1 chopper disk.

Table 7.1.: Measurement results of the first six eigenmodes of the NEAT C1 disk.

	Mode 1	Mode 2	Mode 3	Mode 4	Mode 5	Mode 6
Measurement 1	209.5 Hz	219.0 Hz	232.2 Hz	264.8 Hz	274.0 Hz	279.8 Hz
Measurement 2	210.0 Hz	219.3 Hz	230.3 Hz	265.0 Hz	274.1 Hz	279.7 Hz
Measurement 3	209.2 Hz	219.4 Hz	232.2 Hz	264.2 Hz	–	280.0 Hz
Measurement 4	209.0 Hz	220.0 Hz	231.4 Hz	265.2 Hz	273.8 Hz	280.0 Hz
Measurement 5	209.7 Hz	220.1 Hz	231.6 Hz	264.7 Hz	274.3 Hz	280.0 Hz
Measurement 6	209.3 Hz	220.1 Hz	232.4 Hz	264.1 Hz	273.9 Hz	280.5 Hz
Measurement 7	209.2 Hz	220.2 Hz	231.5 Hz	264.2 Hz	273.3 Hz	280.4 Hz
Measurement 8	209.2 Hz	219.2 Hz	–	264.7 Hz	273.0 Hz	280.2 Hz
Mean Value	209.4 Hz	219.7 Hz	231.6 Hz	264.6 Hz	273.2 Hz	280.1 Hz
Calculated Value	198.9 Hz	204.8 Hz	217.3 Hz	220.2 Hz	224.3 Hz	230.5 Hz
Deviation	5.2 %	7.3 %	6.6 %	20.2 %	21.8 %	21.5 %

7.1.2. Natural frequencies of the complete disk system

In the previous section, the natural frequencies of the disk and the hub have been measured. In this section, the system boundary is extended to the whole system, which consists of the disk, the hub, the shaft, the bearing, the drive and the complete overspeed test stand. A numerical calculation with this extended system is not appropriate due to many uncertainties in the influencing parameters. Nevertheless, information gained in a static natural frequency measurement can be applied for estimations of the rotating systems. Additionally, the shift of the natural frequencies caused by the extension of the system boundary can be determined.

The measurement of the complete system is conducted in the overspeed test stand BI 4, which is described in detail in section 7.2. Two different measurements are done which differ in the position of the acceleration sensors. In the first variant, the acceleration sensors are positioned at the edges of the large areas of the disk. This can be seen in part (a) of figure 7.4 and in the photography in figure 7.5. In the second variant, the acceleration sensors are positioned at the edges of the small areas, which is illustrated in part (b) of figure 7.4. In the first variant, the disk gets excited at the center of its large area and in the second variant in its small area.

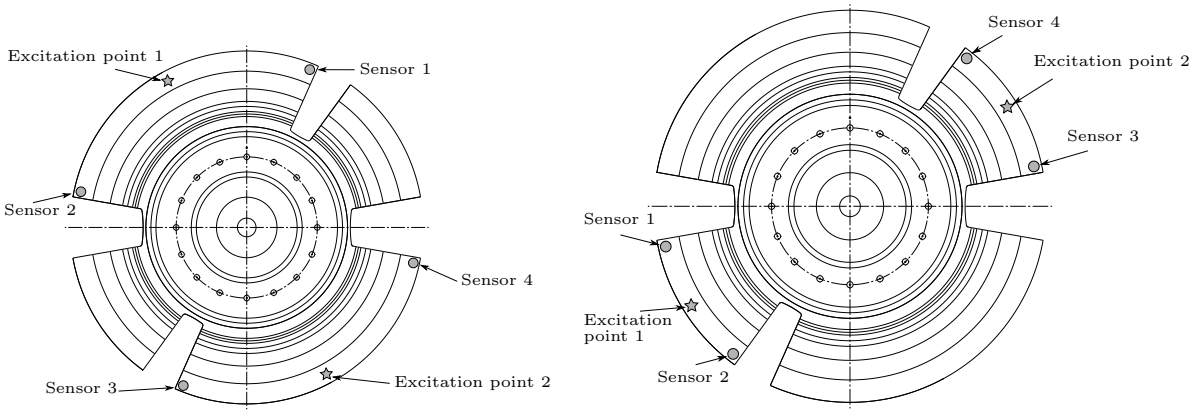

Figure 7.4.: Positions of the acceleration sensors on the disk system, (a) measurement with the sensors on the large area (Variant 1) and (b) measurement with the sensors on the small area (Variant 2).

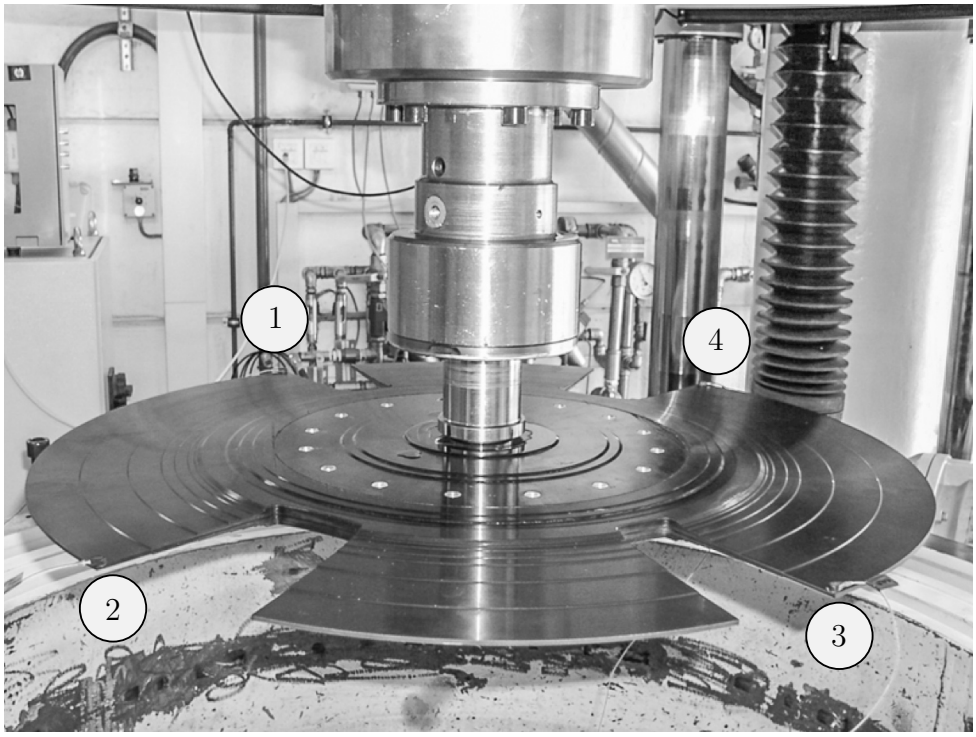

Figure 7.5.: Acceleration sensors applied on the CFRP disk.

The first two natural frequencies which can be measured with the ping test are 71.5 Hz and 76.4 Hz. The first natural frequency appears only in measurement variant 1, where the sensors are located on the large area. The second natural frequency appears in both variants. The shape of the associated eigenmodes is the first bending mode of the shaft. These frequencies can be measured at every ping test of the test stand. Hence, this relatively low natural frequency does not occur at the natural frequency measurement of the disk itself as described in the previous section 7.1.1. The third natural frequency of 243.5 Hz is associated to the eigenmode which describes a bending of the large areas. Hence, this natural frequency is only visible in measurement variant 1. The natural frequencies four, five and six occur in both variants at nearly the same value: Eigenmode no. 4 has a mean value of 270.0 Hz, no. 5 has a mean value of 308.5 Hz and no. 6 has a mean value of 326.1 Hz.

The graphs of the measurements are given in figure 7.6 for the first variant, where the sensors are located in the large area, and in figure 7.7 for the second variant, where the sensors are located in the small area. The value of the amplitude can be treated as a relative one because it is dependent on the intensity of the impact of the hammer. In variant 1, the first and the second eigenmodes differ from each other whereas in measurement 2 both eigenmodes result in one peak. The third eigenmode is visible with a small peak in figure 7.6 whereas the graph of figure 7.7 shows only a small sweep in the area around 240 Hz. The values of the first six natural frequencies are listed in table 7.2 for both variants 1 and 2.

Table 7.2.: Measurement results of the first six eigenmodes of the NEAT C1 disk and the test stand.

	Mode 1	Mode 2	Mode 3	Mode 4	Mode 5	Mode 6
Variant 1	71.5 Hz	76.2 Hz	243.5 Hz	270.1 Hz	309.8 Hz	323.1 Hz
Variant 2	– – Hz	76.6 Hz	– – Hz	269.9 Hz	307.2 Hz	329.1 Hz
Mean Value	71.5 Hz	76.4 Hz	243.5 Hz	270.0 Hz	308.5 Hz	326.1 Hz

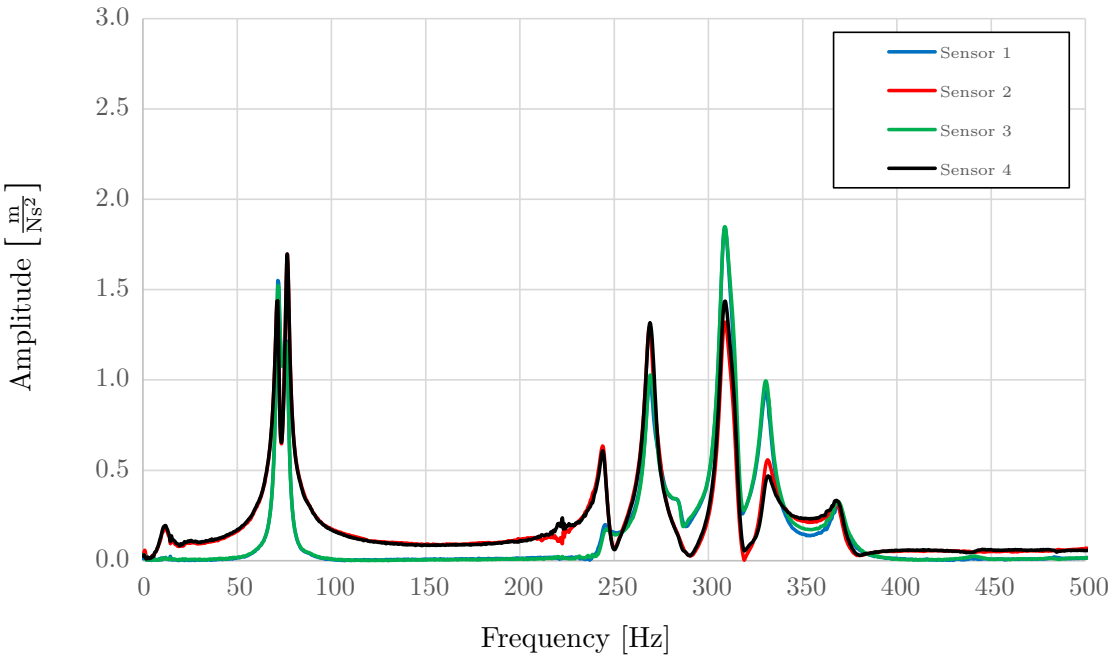

Figure 7.6.: Natural frequency measurement of the disk system with the sensors on the large area (Variant 1).

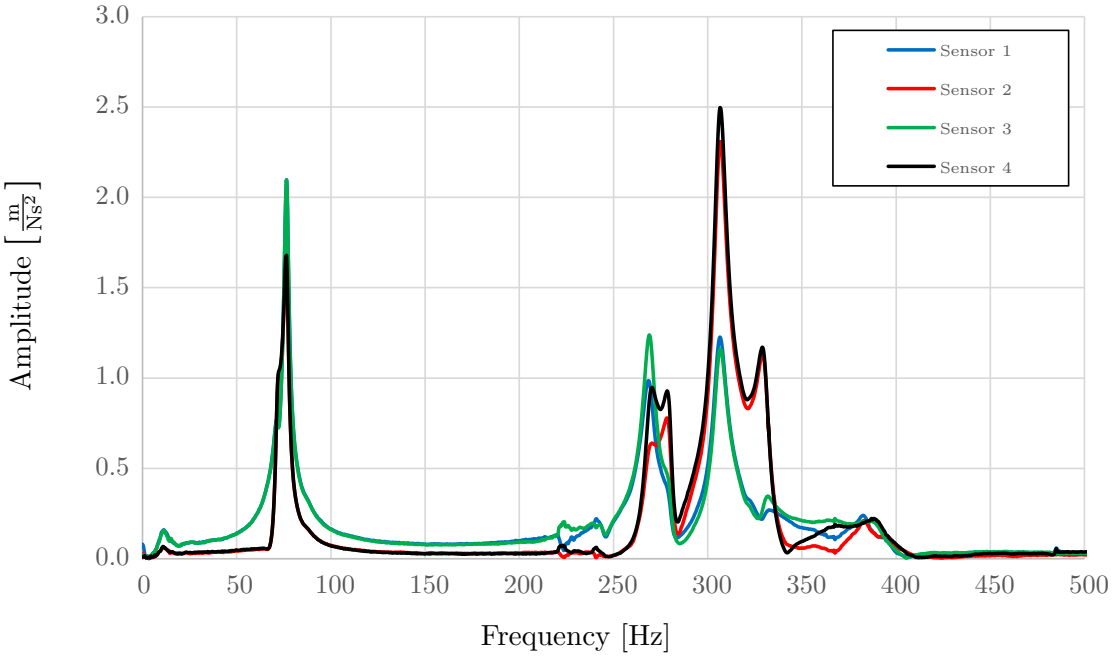

Figure 7.7.: Natural frequency measurement of the disk system with the sensors on the small area (Variant 2).

7.2. Spin test of CFRP disks

Testing of fiber-reinforced structures can be divided into different levels. According to the pyramid of tests by Tomblin [128], there are five levels: Firstly, the level of the coupons; secondly, the level of elements; thirdly, the level of details; fourthly, the level of sub-components and lastly, the level of components. Generally, the quantity of tests decreases from the coupons level to the components level whereas the effort and the costs increase significantly. An example of a pyramid of tests from the field of aviation is given with figure 7.8. This pyramid is established by the Federal Aviation Administration (FAA) for certification tests of aircrafts. For CFRP disks, it is not possible to define specimens on the levels two to four. The hub of the disk can be seen as a part of the sub-components level or the details level but the CFRP disk itself is one piece and is related to the components level [100, 148].

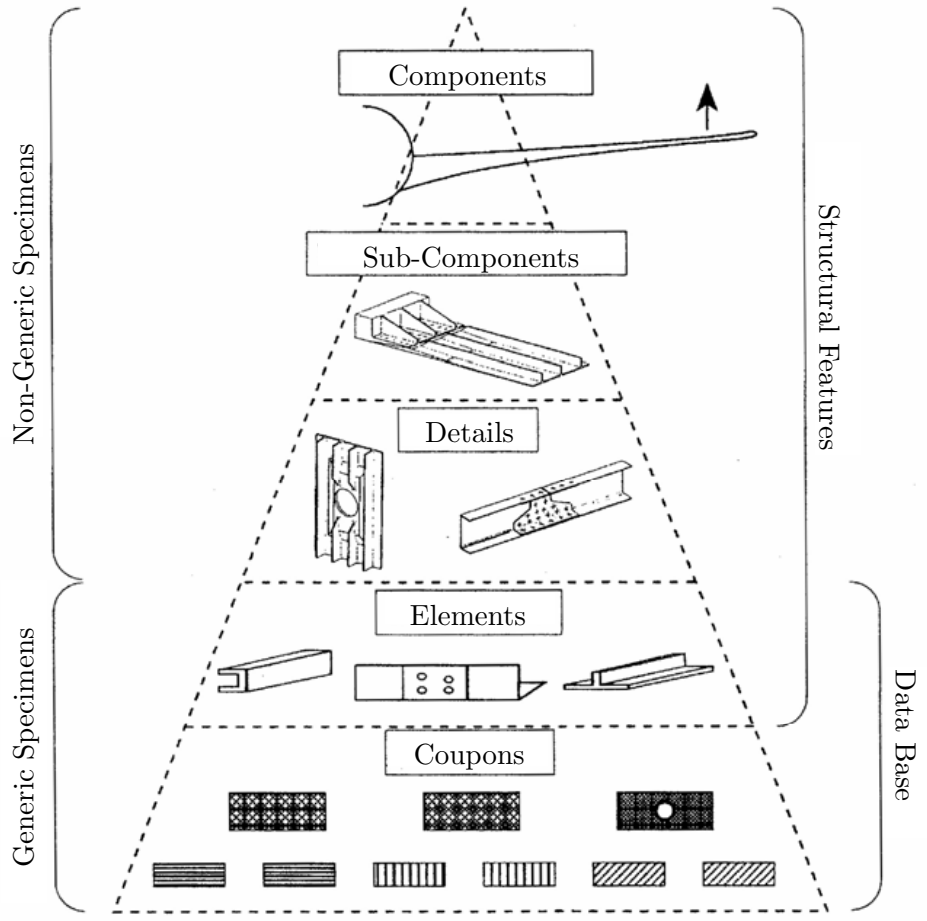

Figure 7.8.: Pyramid of tests for structural substantiation [128].

The material data of the applied lamina is measured by LLB on coupons level and will not be discussed any further. The values of this material characterization are given in chapter 5 in table 5.2. In the following section, the whole CFRP disk on components level will be treated in the spinning tests.

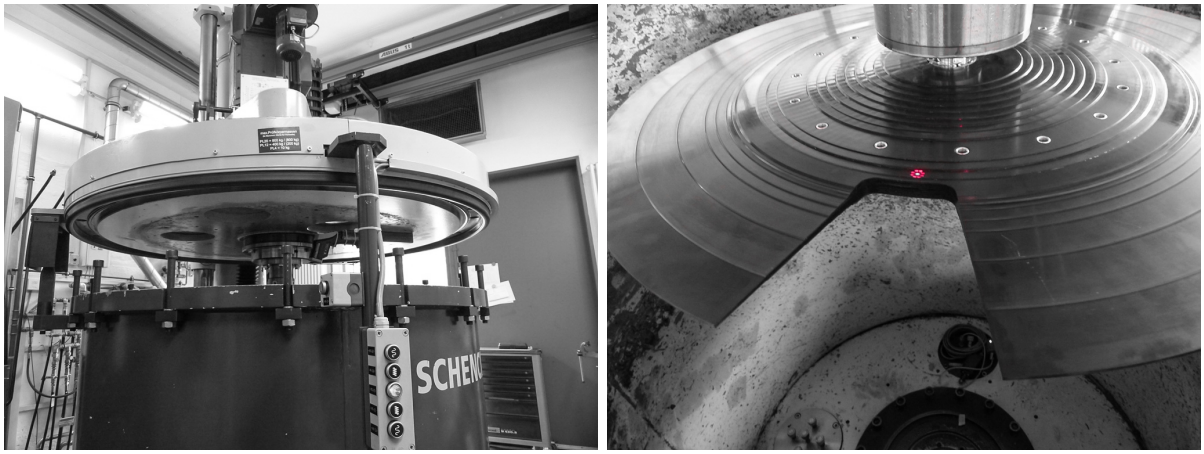

(a) (b)

Figure 7.9.: Overspeed test stand BI 4 by Schenck, (a) test stand with mounted CFRP disk, (b) applied pyrometer for a non-contact temperature measurement during rotation.

The spinning tests are conducted with an overspeed test stand BI 4 by Schenck. The test stand is composed of a vacuum-sealed container with an integrated burst protection. This protection absorbs the energy from the fragments when the rotor bursts. The covering lid of the container resists against high internal pressure. The mechanical drive is mounted on the top of the container. The engine is connected to a precision roller-bearing spindle, which is driven via a flat belt. The overspeed test stand is shown in the left side (a) of figure 7.9. To measure the temperature of the CFRP disk during the test, a pyrometer is applied to the test stand. With this pyrometer, the temperature of the laminate can be measured without contact. During the spinning test, the test stand is under a vacuum of a range from $7 \cdot 10^{-2}$ mbar to $9 \cdot 10^{-2}$ mbar. This leads to a heating of the CFRP due to friction between the disk and the remaining air molecules. At the same time, the vacuum is a good isolator, which means that the generated heat will be transfered slowly from the disk to the housing [121]. The pyrometer measurement spot can be seen in red in the right side (b) of figure 7.9.

7.2.1. Measurement of the widening of the central through-hole of CFRP disks during rotation

The radial widening of the central through-hole of the CFRP disk is a major design criterion. In the previous chapters, different CFRP disks have been analyzed for their radial widening of the through-hole and have been optimized for lower radial displacements. To verify the calculations of the widening and to avoid the displacement effect caused by the cut-outs leading to a non-uniform deformation of the central through-hole at high rotational speeds, a disk without cut-outs is manufactured. The radial extension of the through-hole of this test disk is 0.10 mm or 0.4 % at a rotational speed of 298 Hz. This widening is circular. In this disk, a full aluminum hub with a radial oversize of 0.10 mm is assembled by cold pressing-in. The radial extension of the aluminum hub during rotation is 0.001 mm or 0.004 %, which can be regarded as negligible. The geometrical parameters of the disk are listed in table 7.3 and pictures of the disk are shown in figure 7.10. The picture on the left shows the disk from the bottom. The picture on the right shows the disk mounted on the shaft and assembled in the spinning test machine.

Table 7.3.: Dimensions of the tested CFRP disk.

Diameter	700 mm
Maximum thickness	26.2 mm
Minimum thickness	3.2 mm
Mass	6.680 kg
Diameter of the central through-hole	50 mm

Hence, a spinning test of this disk is done with the aim of measuring the detachment of the disk from the hub at a rotational speed of around 298 Hz. During the spinning test, the vibrations of the shaft are measured. They are plotted together with the rotational speed versus the time in figure 7.11. The vibrations are given in percentage. 100 % equals a deflection of the shaft at the upper end of 0.1 mm.

In the graph of figure 7.11, three areas are marked. The first area I shows a resonance starting at t = 180 s and ending at t = 410 s with a maximum vibration of 18 %. This resonance is the second eigenmode of the shaft and is independent of the design of the disk. It occurs on every spinning test at a rotational speed which is dependent on the shaft utilized. This natural frequency was also measured in the previous section 7.1.2 with the static eigenmode measurement of the complete disk system. In area II, the disk gets

(a) (b)

Figure 7.10.: CFRP disk without cut-outs, (a) view from the bottom and (b) disk mounted on the shaft and assembled in the spinning test machine.

further accelerated from 280 Hz to 306 Hz, showing a constant vibration level around 20 %. This vibration level is caused by the permissible residual unbalance. At a rotational speed of 306 Hz, there is an abrupt increase in shaft vibrations from 20 % to 90 %, which is caused by the disk detaching itself from the hub. This is a deviation of 2.7 % from the calculated detachment speed. The detachment is marked with area III in figure 7.11. Accordingly, the FE model of the disk-hub connection can be seen as an appropriate one. After the deceleration of the disk, no damage is noticed in the laminate or in the area around the central through-hole. This detachment is repeated several times with an equal result.

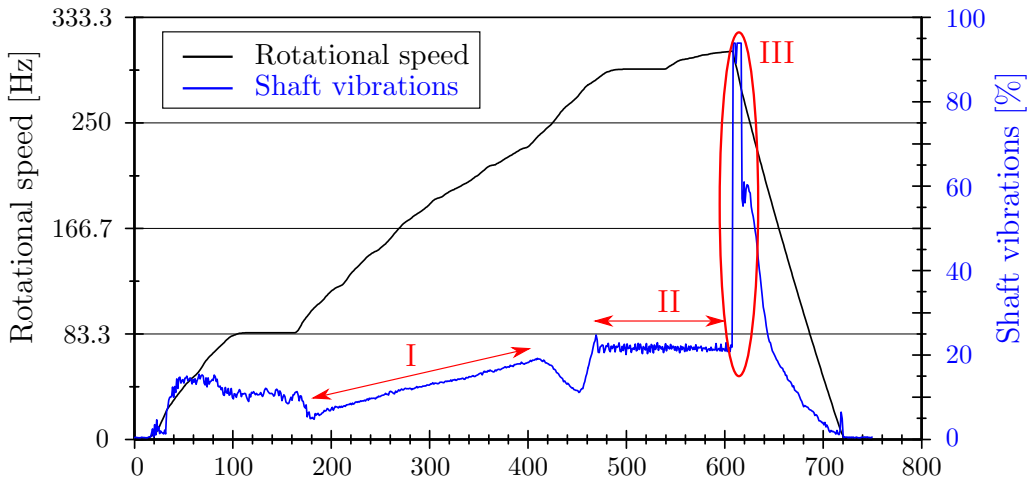

Figure 7.11.: Spinning test of the disk without cut-outs and with a full aluminum hub.

7.2.2. Test of a new hub design for high rotational speeds

In section 6.3, a new design of a hub is presented which has been optimized for high rotational speeds. The numerical calculation of the contact pressure between the hub and the disk is described in chapter 5.2. A full aluminum hub detaches itself from the CFRP disk at a rotational speed of approximately 300 Hz, as shown in the previous section 7.2.1. For higher rotational speeds, the hub needs to widen itself in order to stay in contact with the disk. The new design, which is the result of different optimizations, is shown in figure 7.12. For a better illustration, different variants of the hub are built with additive layer manufacturing (ALM), which is shown on the left side in figure 7.12. The final version of the hub is manufactured of aluminum AL7075 with wire cutting. This version is shown on the right side in figure 7.12. In order to increase the contact pressure of the wings of the hub, tungsten weights are applied in the aluminum hub. Every wing of the hub contains five holes into which tungsten bars are pressed. This can be seen on the right side in figure 7.13.

(a) (b)

Figure 7.12.: New design of a hub for high rotational speeds, (a) Prototype made with additive manufacturing, (b) manufactured of aluminum with wire cutting.

The spin test with the disk of the previous section 7.2.1 is repeated with the new hub. The assembly of the CFRP disk and the new hub is shown in figure 7.13. During this spin test, the disk remains in contact with the hub up to a rotational speed of 380 Hz. This confirms the calculations of the widening of the hub under centrifugal load.

(a) (b)

Figure 7.13.: Application of the new hub in a CFRP disk, (a) overview of the assembly, (b) detailed view on the hub with tungsten weights.

7.2.3. Strength test of disks at overspeed

In the previous sections, the natural frequencies and the widening of the central through-hole of CFRP disks were measured with experiments. In this section, the strength is taken into account. The overspeed test stand is able to resist a failure or a burst of the CFRP disk. Nevertheless, measurement equipment in the test stand can be damaged significantly at the moment of the failure of the disk [100]. Hence, only the vibrations of the shaft are measured and no additional measurement equipment is installed in the test stand. Kogo presents in "Spin Burst Test of Carbon-Carbon Composite Disk" a possibility to measure the strain of rotating disks with strain gages in a vacuum test stand with a telemeter [75]. This test equipment is, however, not available for the test presented here. Due to the very high centrifugal forces in the estimated rotational speed range of the failure, every small fracture will lead to complete failure of the disk.

A graph of an overspeed test is shown in figure 7.14. Here, the shaft vibrations and the rotational speed are plotted versus the time. At the beginning of the test, the disk gets accelerated to 83.3 Hz and maintains this rotational speed for 120 s. Afterwards, the disk gets further accelerated to 350 Hz and again maintains this rotational speed for 120 s. After a deceleration to 83.3 Hz, the disk gets accelerated a second time in steps until failure. The vibration of the shaft in the time area from 1250 s to 1550 s is at a constantly low level of 5 %. This implies a very good static and dynamic balancing of the disk. At 1550 s, there is a peak in the shaft vibrations to nearly 100 %, which is caused by the failure of

the disk. The rotational speed at this point is 380.5 Hz, which equals a tip speed of 897 $^{m}/_{s}$. The tip speed is the velocity of a point on the outer diameter of the disk. In figure 7.14, the vibration peak is marked with area I. A photograph of the destroyed CFRP disk can be seen in figure 7.15. The failure mode remains unclear due to the fact that the disk is completely destroyed. The predicted point of failure from the numerical analysis is at 384 Hz. At this rotational speed, the safety factor becomes $S_f = 1$. On the basis of the measurement data of the shaft vibrations, an interaction between the rotational speed and the natural frequencies can be excluded. A triggering of the disk by a natural frequency would be identifiable by a slow increase in vibration level of the shaft, as can be seen in the time range from 250 s to 350 s in figure 7.14. In contrast, vibration in the time range from 1250 s to 1550 s remains at a low level of around 5 % and shows no increase. Beside the possibility that the failure of the disk is a structural failure of the CFRP laminate, a detachment of the disk itself from the hub cannot be excluded.

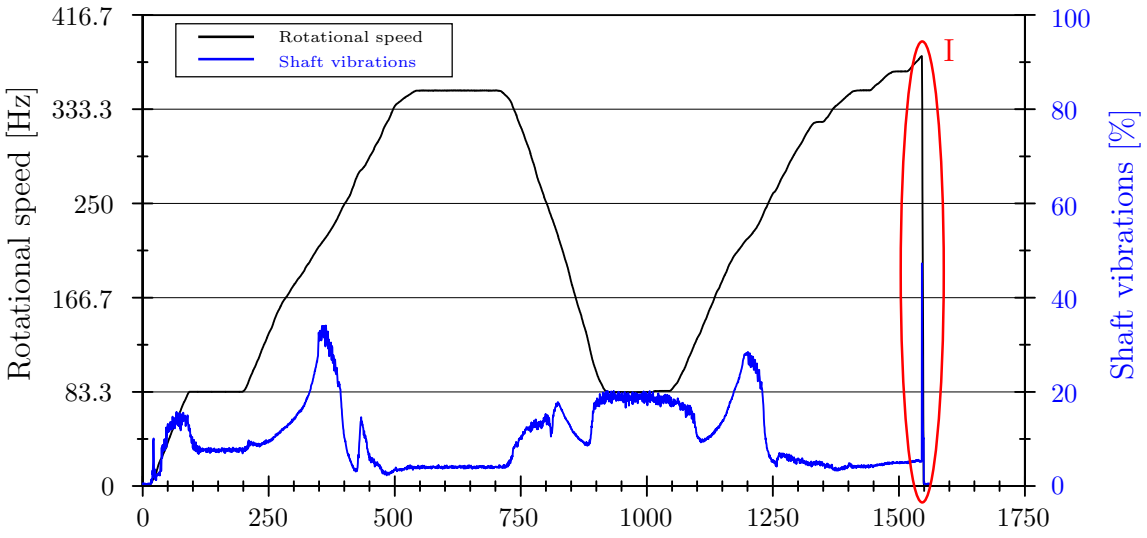

Figure 7.14.: Spinning test of a CFRP disk at overspeed until failure.

Figure 7.15.: Destroyed chopper disk after spinning strength test at overspeed [145].

8

Correlation and discussion of the analysis results and measurement results

In this chapter, the analysis results of the novel design of the CFRP disk are compared with the results of the measurements and tests. It is shown that the dynamic and strength tests confirm the numerical results. The impact of acceleration sensors on the measurement results is pointed out.

Contents

8.1. Comparison of the results of the structural analysis with the measurement of the natural frequencies of a CFRP disk

The natural frequencies of the CFRP disks have been measured in the previous chapter 7 in two different variants: The first variant are the natural frequencies of the disk and the hub and the second variant is the complete disk system. Both measurements are conducted under static conditions with a non-rotating disk. The measurements are performed with acceleration sensors which are placed on the outer diameter of the disks.

The analysis of the natural frequencies of the disk is performed for the first variant with the disk and the hub. Here, the system boundary is precisely defined. For the analyses, a three-dimensional FE model of the disk is used. The acceleration sensors have a mass of 20 g. This has to be taken into account during the analyses. Due to the fact that the disk itself is a three-dimensional model, the sensors as well are modeled with volume elements. In contrast to a modeling with mass points, the modeling with volume elements has the advantage that the stiffening of the model by the sensors is considered as well as the influence of the mass and the inertia.

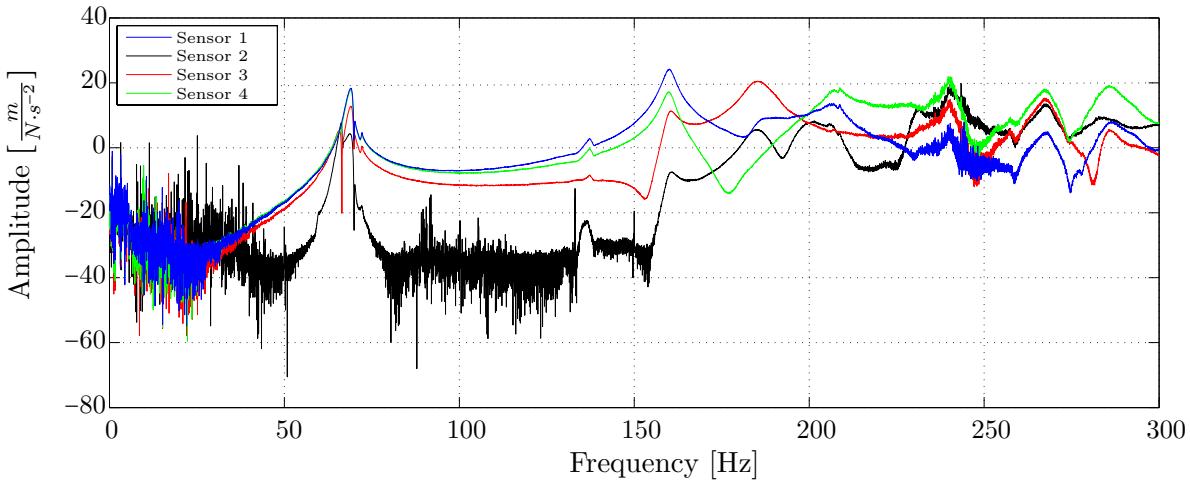

Figure 8.1.: Results of an experimental measurement of the natural frequencies of a CFRP disk.

The comparison between the results of the analysis of the natural frequencies and the measurement of the natural frequencies is listed in table 8.1. For the first two eigenmodes, the deviation between the measurement results and the analysis results is between 7.8 %

Table 8.1.: Comparison between the results of the analysis of the natural frequencies and the measurement of the natural frequencies of a CFRP disk.

	Mode 1	Mode 2	Mode 3	Mode 4	Mode 5	Mode 6
Numerical analysis	72.2 Hz	75.3 Hz	167.7 Hz	176.8 Hz	201.2 Hz	231.1 Hz
Experimental measurement	66.1 Hz	69.4 Hz	160.2 Hz	185.5 Hz	208.1 Hz	239.2 Hz
Deviation	8.4 %	7.8 %	4.5 %	4.9 %	3.4 %	3.5 %

and 8.4 %, and for the eigenmodes three to six between 3.4 % and 4.9 %. The first two eigenmodes are bending modes of the hub while the higher eigenmodes are modes of the disk. The numerical analysis overestimates the values of the bending modes of the hub. This could be caused by the thin-walled construction of the hub, which requires a very fine meshing in the FE tool. The values of the higher eigenmodes are underestimated by the numerical analysis by approximately 4 %. This could be caused by a higher fiber volume ratio in the tested disk. All in all, the correlation between the calculated and the measured results can be treated as a very good one.

Table 8.2.: Comparison between the analysis results of the natural frequencies of a CFRP disk with sensors and a CFRP disk without sensors.

	Mode 1	Mode 2	Mode 3	Mode 4	Mode 5	Mode 6
Numerical analysis with sensors	72.2 Hz	75.3 Hz	167.7 Hz	176.8 Hz	201.2 Hz	231.1 Hz
Numerical analysis without sensors	74.1 Hz	79.8 Hz	214.8 Hz	224.1 Hz	232.7 Hz	258.4 Hz
Deviation	2.6 %	6.0 %	28.1 %	26.8 %	15.7 %	11.8 %

The comparison between the analysis results of the natural frequencies of a CFRP disk with sensors and one without sensors is listed in table 8.2. For the first two modes, the influence of the sensors is between 2.6 % and 6.0 % and can be seen as negligible. These first two eigenmodes are bending modes of the hub, which means that the disk itself behaves as a rigid body and the strain occurs only in the hub. The shape of the eigenmodes is the same for both variants. This explains the small deviation between both variants. The values of the calculation with the sensors are lower than the ones without sensors. This agrees with the assumption of a disadvantageous mass distribution of the

variant with sensors.

For higher eigenmodes, the difference between the results of the model with sensors and the one without sensors increases to a value of 28.1 %. The influence of the sensors on the shape of the eigenmodes cannot be neglected and makes it difficult to find a matching pair that can be compared to each other. In order to validate FE models, a modeling of the sensors is highly recommended.

8.2. Comparison of the results of the structural analysis and the measurement of the strength of the CFRP disk

The strength of CFRP disks is treated in this thesis in chapter 5 as well as in sections 6.2.3 and 6.2.4. Here, the disk is optimized for a higher safety factor against failure with a shape optimization of the bottom area of the cut-outs. An execution of a validation of the calculation results is intricate and cost-intensive due to the complexity of the experiment. In section 7.2.3, a strength test of a CFRP disk is described. The results of the calculation show at a rotational speed of 384 Hz a safety factor of $S_f = 1$ concerning the maximum principle strain in the laminate. During the experimental test, the disk fails at a rotational speed of 380.5 Hz. The deviation between the calculated and the measured results is 0.9 %, which can be treated as a very good correlation. Yet it has to be mentioned that in order to substantiate the results, the measurement should be repeated several times. In the past, certain similar experiments have been conducted at LLB with different CFRP disks. The results of those experiments show values similar to the calculated results of those disks. However, the results of those experiments are not directly comparable to the experiments presented in this thesis as geometry, materials and operational speeds are significantly different.

The stress in the disk is caused mainly by the centrifugal forces and splits up in the laminate into a stress in radial and one in tangential direction, which leads to a multi-axial stress condition. This multi-axial load state makes a test on specimen level difficult. A biaxial tensile test could be performed with a cruciform testing machine by Zwick [155]. This could reduce the high costs of an overspeed burst test of a complete CFRP disk.

9

Summary and conclusions

At the beginning of this chapter, a summary of the conducted research work is given. The summary includes the following three core aspects:

- Structural analysis of different variants of high-speed rotating CFRP disks.
- Design optimization of CFRP disks with regard to their structural dynamics.
- Experimental measurement of the strength and the vibration behavior of CFRP disks.

Afterwards, the results of the analysis and optimization of the CFRP disks rotating at a very high speed are discussed and conclusions are drawn.

Contents

9.1. Summary of the research work

Disks rotating at a high or a very high speed are used in different fields of application. One specific application is the neutron TOF spectroscopy. For better results in the TOF method, higher rotational speeds are needed. This leads not only to a strength problem of the disks, which are made of CFRP, but also to difficulties with the structural dynamics. The same applies for flywheels, which gain a higher energy density with higher speeds of the rotor. Hence, in this thesis, a detailed analysis of the vibration behavior during rotation as well as a design optimization are presented. First, different examples of high speed rotating CFRP disks are described. Further, the fundamentals of the calculation methods used in this thesis are described and set in reference to the utilization on CFRP disks. A special attention is given to the rotordynamic effects which occur during the rotation of disks. Subsequently, a detailed structural analysis of an existing CFRP disk is presented and discussed. The key points of the analysis are the calculation of the natural frequencies of non-rotating and rotating disks, the computation of the displacement field, the calculation of the strain distribution of the disk at different rotational speeds, and the computation of the contact between the disk and the hub. A non-linear solution approach is needed for the latter, which is presented theoretically in section 3.3 and practically applied in section 5.2. Subsequently, the design of the disk is optimized for different functions. The main focus of the optimization lies on an improvement of the structural dynamic behavior of the disk so that the disk can be accelerated to higher rotational speeds. Additionally, the optimization takes into account the strength of the disk as well as the contact behavior of the disk to the hub. Furthermore, an enhanced design approach of CFRP disks taking into account the membrane stiffening of the disk during rotation and manufacturing constraints is introduced. With the results of the structural analysis and the optimization, a new CFRP disk is designed and manufactured at LLB. This new disk is examined experimentally for its vibration behavior, its connection to the hub and finally during an overspeed spin test for its strength. The results of the experimental measurement are compared in detail to the results of the computation. A satisfying correlation of both results is determined.

9.2. Conclusions and outlook

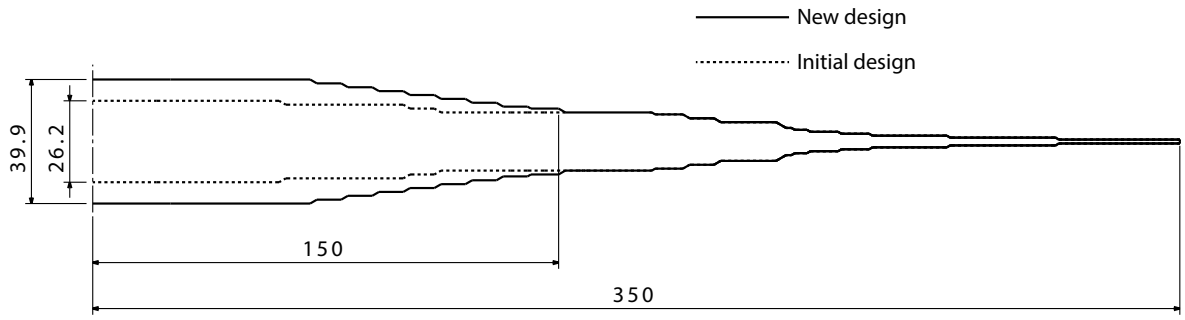

Figure 9.1.: Cross sections of the initial and the new CFRP disk designs.

In this thesis, the design and optimization of high speed rotating CFRP disks with a special regard to their vibration behavior are treated. With higher rotational speeds, the vibration behavior and the structural dynamics become increasingly important. A design with a main focus only on the strength and the centrifugal forces is not able to increase the rotational speeds further on. A profound knowledge of the coherences of the rotordynamic principles is a requirement for an enhancement of the disks. In this thesis, a new design approach for CFRP disks is introduced, which comprises the vibration behavior and the natural frequencies during rotation of a CFRP disk as well as contact phenomena and stress peaks around the cut-outs. With a specific disk for neutron TOF experiments, the improvement of the new design and the application of the design optimization methods are demonstrated. The new design is manufactured and afterwards tested experimentally in order to verify the predicted enhancement. The improvement of the disk which is achieved by the utilization of the design methods, is listed in table 9.1. The first natural frequency of the CFRP disk with the initial design is 217 Hz and the one of the new design is 274 Hz. This equals an increase of 26 %. The radial widening of the central through-hole is reduced from 0.21 mm to 0.16 mm, which equals an improvement of 24 %. The stress peaks in the CFRP laminate around the cut-outs are significantly reduced with a numerical shape optimization. The failure index of the initial design at a rotational speed of 384 Hz is 1.8 and the one of the new design is 0.9, which equals an enhancement of 50 %.

The CFRP disk with the initial design fails at a rotational speed of 303.3 Hz due to the disk detaching itself from the hub. The new design of the disk takes into consideration the results of the optimizations for higher natural frequencies and lower radial displacement around the central through-hole. The cross section of the new design compared with the initial design is shown in figure 9.1. The numerical analysis of the new design shows a

Table 9.1.: Improvement of the CFRP disk achieved by the new design process.

Optimization of...	natural frequencies	radial displacement	shape of the cut-outs
Initial design	217 Hz	0.21 mm	$FI = 1.8$
Optimized design	274 Hz	0.16 mm	$FI = 0.9$
Improvement	+26 %	−24 %	−50 %

maximum possible rotational speed of 383.3 Hz. At this rotational speed, the failure index of the laminate around the cut-outs reaches 1.0 and the disk starts detaching itself from the hub. During the spinning strength test, the CFRP disk fails at a rotational speed of 380.5 Hz, which is a deviation of 0.7 % from the predicted one. Compared to the initial design, this is an improvement of 25 %. Hence, for further designs of CFRP disks, the new design approach can be recommended.

A
Appendix

Contents

A.1. Technical drawings of the disks

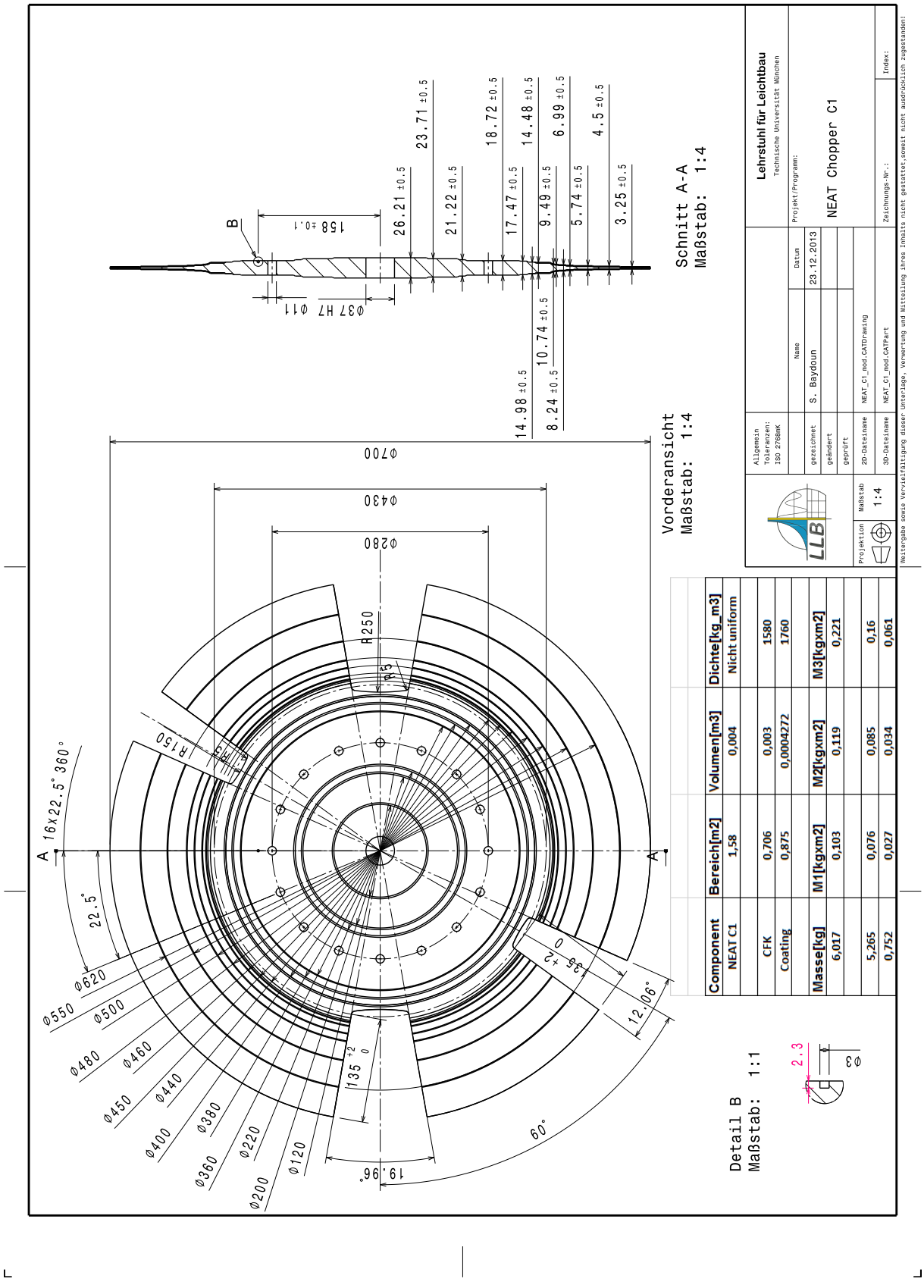

Figure A.1.: Draft of the NEAT C1 chopper disk.

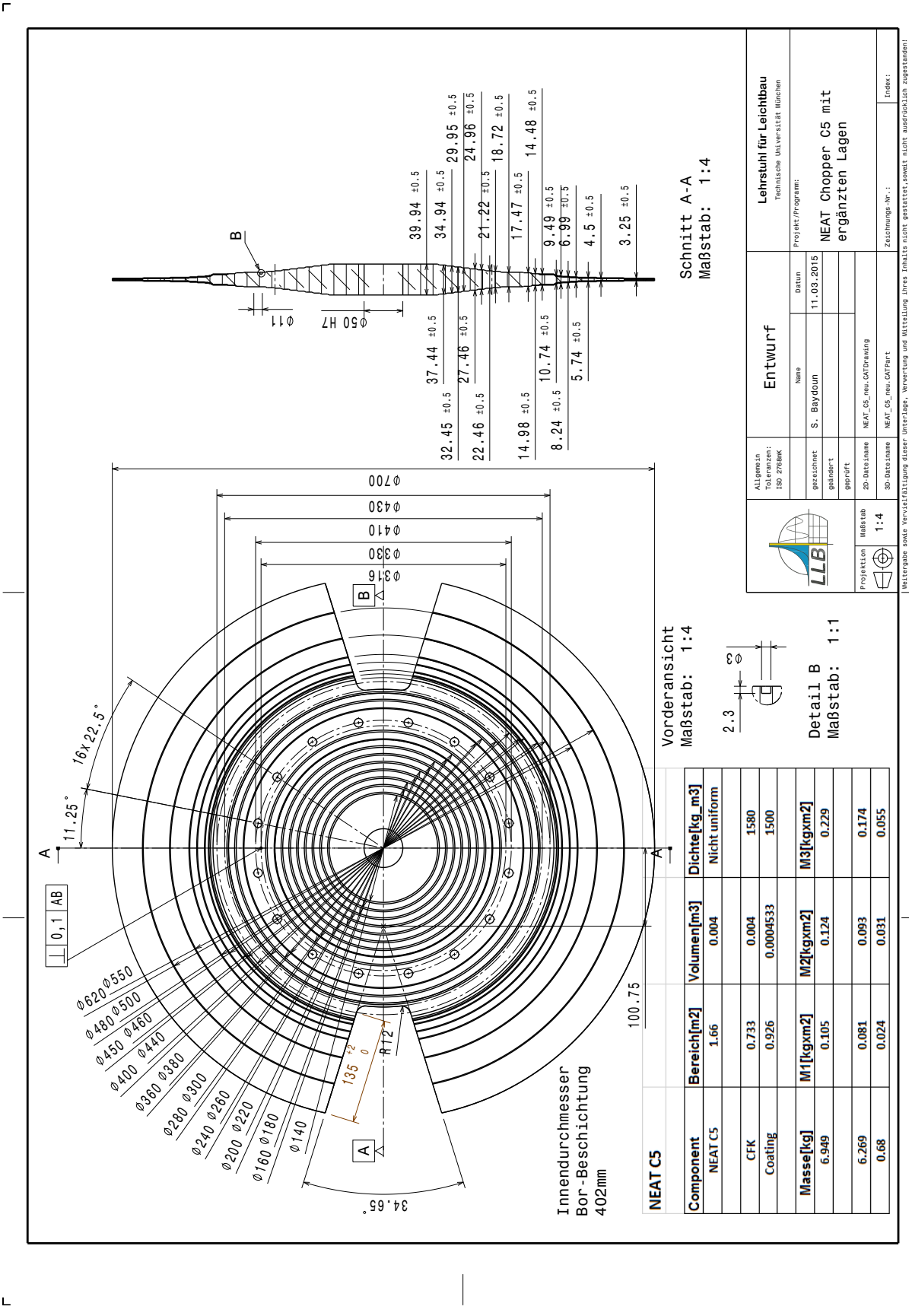

Component	Bereich[m2]	Volumen[m3]	Dichte[kg_m3]
NEAT C5	1.66	0.004	Nicht uniform
CFK	0.733	0.004	1580
Coating	0.926	0.0004533	1500

Masse[kg]	M1[kgxm2]	M2[kgxm2]	M3[kgxm2]
6.949	0.105	0.124	0.229
6.269	0.081	0.093	0.174
0.68	0.024	0.031	0.055

Figure A.2.: Draft of the NEAT C5 chopper disk.

A.2. Technical drawing of the hub

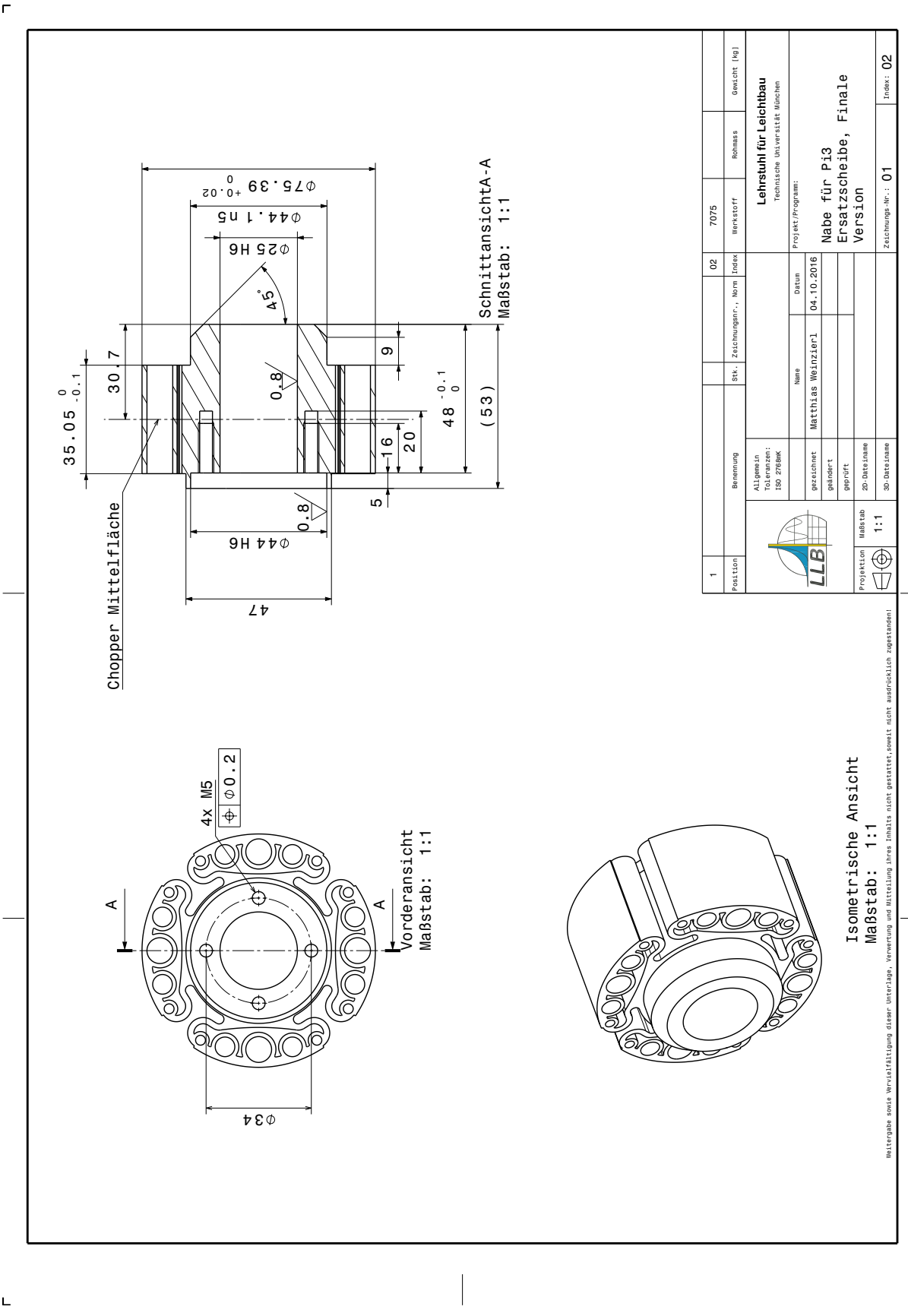

Figure A.3.: Draft of the hub of a chopper disk.

B
Code

Contents

B.1. Input file of the sizing optimization task of the CFRP disk for higher natural frequencies with Hyperworks Optistruct

Listing B.1: Altair Hyperworks Optistruct Code Disk

```
$$#########################################################################$
$$ Script:              Optistruct Input Deck                             $
$$ Datum:               2017/01/09                                        $
$$ Author:              Weinzierl, Matthias                               $
$$#########################################################################$
$$-------------------------------------------------------------------------$
$$                                                                        $
$$ 0 - Description of FreeSize Optimization                               $
$$                                                                        $
$$ 1 - Settings                                                           $
$$      1.0 General Settings                                              $
$$      1.1 Optistruct Settings                                           $
$$      1.2 Load Case and Analysis Definition                             $
$$                                                                        $
$$ 2 - Bulk Data                                                          $
$$      2.0 Design Variables                                              $
$$      2.1 Optimization Responses                                        $
$$      2.2 Mesh                                                          $
$$      2.4 Material and Element Properties                               $
$$      2.5 Definition of Loads and Boundary Conditions                   $
$$                                                                        $
$$-------------------------------------------------------------------------$
$$----1|------2|------3|------4|------5|------6|------7|------8|------9|-----10|$
$$-------------------------------------------------------------------------$
$$   1          Settings                                                  $
$$-------------------------------------------------------------------------$
$$
$$
$$   1.0        General Settings
$$-------------------------------------------------------------------------$
SCREEN LOG
CSTRAIN(H3D,ALL,MECH) = YES
CSTRESS(H3D,ALL) = ALL
DAMAGE(H3D) = ALL
DISPLACEMENT(H3D,,,,) = ALL
ESE(H3D,) = ALL
STRAIN(H3D,ALL,,MECH,) = ALL
STRESS(H3D,ALL,,) = YES
$$
$$
$$   1.1        Optistruct Settings
$$-------------------------------------------------------------------------$
$$  OBJECTIVES Data
$HMNAME OBJECTIVES       1objective
$
```

```
46 DESOBJ(MAX)=5
47 DESGLB          2
48 $
49 ECHO = NONE
50 $$
51 $$
52 $$    1.2          Load Case and Analysis Definition
53 $$-------------------------------------------------------------------------------$
54 SUBCASE          1
55    LABEL modal
56    SPC =          2
57    METHOD(STRUCTURE) =          6
58 $
59 SUBCASE          6
60    LABEL rotation384
61    LOAD =          4
62 $
63 SUBCASE          9
64    LABEL modal384
65    SPC =          2
66    METHOD(STRUCTURE) =          6
67    STATSUB(PRELOAD) =          6
68 $$
69 $$
70 $$-------------------------------------------------------------------------------$
71 $$    2            Bulk Data
                                                $
72 $$-------------------------------------------------------------------------------$
73 BEGIN BULK
74 $
75 $
76 $HMSET          1          2 "set25"
77 $HMSETTYPE          1 "regular"
78 SET       1         ELEM      LIST
79 +         1         2         3         4         5         6         7         8
80 +         9         10        11        12        13        14        15        16
81 +         17        18        19        20        21        22        23        24
82 +         25        26        27        ...
83 $
84 $
85 $HMSET          2          2 "set30"
86 $HMSETTYPE          2 "regular"
87 SET       2         ELEM      LIST
88 +         1251      1252      1253      1254      1255      1256      1257      1258
89 +         1259      1260      1261      1262      1263      1264      1265      1266
90 +         1267      1268      1269      1270      1271      1272      1273      1274
91 +         1275      1276      1277      ...
92 $
93 $
94 $HMSET          3          2 "set40"
95 $HMSETTYPE          3 "regular"
96 SET       3         ELEM      LIST
97 +         3751      ...
98 $$
99 $$
```

```
100 $$    2.0          Design Variables
101 $$-------------------------------------------------------------------------------$
102 $HMNAME DESVARS          1thickness
103 DSIZE    1          PSHELL   1
104 +        THICK      1.28      40.0
105 +        GROUP                      1        2        3        4        5        6
106 +                              7        8        9       10       11       12       13
107 +                             14       15       16       17       18       19       20
108 +                             21       22       23       24       25       26       27
109 +                             28       29       30       31       32       33       34
110 $$
111 $$
112 $$    2.1          Optimization Responses and Constraints
113 $$-------------------------------------------------------------------------------$
114 DRESP1   1          res_massMASS
115 DRESP1   2          res_freqFREQ                                    1
116 DRESP1   3          res_freqFREQ                                    2
117 DRESP1   4          res_freqFREQ                                    3
118 DRESP2   5          res_sum        SUM
119 +        DRESP1L          2        9        3        9        4        9
120 DRESP1   6          res_freqFREQ                                    4
121 DRESP1   7          res_freqFREQ                                    5
122 DRESP1   8          res_freqFREQ                                    6
123 DRESP1   9          res_freqFREQ                                    7
124 DRESP1   10         res_freqFREQ                                    8
125 DRESP1   11         res_freqFREQ                                    9
126 DRESP1   12         res_freqFREQ                                   10
127 $$
128 $$  OPTICONSTRAINTS Data
129 $$
130 $
131 $HMNAME OPTICONSTRAINTS          1con_mass
132 $
133 DCONSTR          1          1          0.006
134 $
135 DCONADD          2          1
136 $
137 $
138 PARAM,CHECKEL,NO
139 PARAM,INREL,-2
140 $HMNAME SYSTCOL          1 "auto2"
141 $HWCOLOR SYSTCOL          1         45
142 $$
143 $$
144 $$    2.2          Mesh
145 $$-------------------------------------------------------------------------------$
146 CORD1C          1    23879   181883   181882
147 $$
148 $$  GRID Data
149 $$
150 GRID          23876          10.0       0.0       0.0               1
151 GRID          23879           0.0       0.0       0.0
152 GRID          23880          ...
153 GRID          ...
154 $$
```

```
$$
$$  CONM2 Elements
$$
CONM2        52331   130893         01.6216-8      0.0       0.0       0.0
CONM2        52332   130894         01.6216-8      0.0       0.0       0.0
CONM2        52333   130895         01.6216-8      0.0       0.0       0.0
CONM2        52334   130896          ...
CONM2        ...
$$
$$
$$  CQUAD8 Elements
$$
CQUAD8           1        1    24939    24948    24951    24937    24947    24950+
+            24955    24938
CQUAD8           2        1    24937    24951    24953    24935    24955    24952+
+            24956    24936
CQUAD8           3        1    24935    ...
CQUAD8           ...
$$
$$
$$    2.4          Material and Element Properties
$$-------------------------------------------------------------------------------$
PSHELL           1        130.0            1                1         0.0
MAT1             154000.0 21000.0 0.032    1.52-9
$$
$$
$$    2.5          Definition of Loads and Boundary Conditions
$$-------------------------------------------------------------------------------$
$HMNAME LOADCOL                  2"shaft"
$HWCOLOR LOADCOL                 2       11
$$
$$  EIGRL cards
$$
$HMNAME LOADCOL                  6"modal"
$HWCOLOR LOADCOL                 6       11
EIGRL            6       1.0              10                                MASS
$$
$$  SPC Data
$$
SPC              2    24389  123456      0.0
SPC              2    24388  123456      0.0
SPC              2    24387  123456      0.0
SPC              2    24386  ...
SPC              ...
$
RFORCE           4    23876        0384.0    0.0       0.0       1.0
+         0.0
$$
ENDDATA
$$-------------------------------------------------------------------------------$$
```

B.2. Input file of the topology optimization of the hub with Hyperworks Optistruct

Listing B.2: Altair Hyperworks Optistruct Code Hub

```
$$#########################################################################$
$$ Script:              Optistruct Input Deck                             $
$$ Datum:               2017/01/09                                        $
$$ Author:              Weinzierl, Matthias                               $
$$#########################################################################$
$$-------------------------------------------------------------------------$
$$                                                                         $
$$ 0 - Description of Topology Optimization                                $
$$                                                                         $
$$ 1 - Settings                                                            $
$$      1.0 General Settings                                               $
$$      1.1 Optistruct Settings                                            $
$$      1.2 Load Case and Analysis Definition                              $
$$                                                                         $
$$ 2 - Bulk Data                                                           $
$$      2.0 Design Variables                                               $
$$      2.1 Optimization Responses                                         $
$$      2.2 Mesh                                                           $
$$      2.4 Material and Element Properties                                $
$$      2.5 Definition of Loads and Boundary Conditions                    $
$$                                                                         $
$$-------------------------------------------------------------------------$
$$----1|------2|------3|------4|------5|------6|------7|------8|------9|-----10|$
$$-------------------------------------------------------------------------$
$$   1          Settings                                                   $
$$-------------------------------------------------------------------------$
$$
$$
$$   1.0        General Settings
$$-------------------------------------------------------------------------$
$$
$$
$$   1.1        Optistruct Settings
$$-------------------------------------------------------------------------$
$HMNAME OBJECTIVES        1objective
$
DESOBJ(MIN)=14
$
  DESSUB =         6
$$
$$
$$   1.2        Load Case and Analysis Definition
$$-------------------------------------------------------------------------$
$HMNAME LOADSTEP                  1"tempload"        1
$
SUBCASE         1
  LABEL tempload
ANALYSIS STATICS
```

```
49    TEMPERATURE(LOAD) =          1
50  $$
51  $$
52  $$-------------------------------------------------------------------------------$
53  $$    2          Bulk Data                                                        $
54  $$-------------------------------------------------------------------------------$
55  BEGIN BULK
56  PARAM,CHECKEL,YES
57  PARAM,POST,0
58  PARAM,INREL,-2
59  $$
60  $$
61  $$    2.0        Design Variables
62  $$-------------------------------------------------------------------------------$
63  $HMNAME DESVARS          1topo
64  DTPL      1        PSHELL   1
65  +         PATRN            2     9624                    2
66  +                                239
67  $$
68  $$
69  $$    2.1        Optimization Responses and Constraints
70  $$-------------------------------------------------------------------------------$
71  DRESP1   6         volfrac VOLFRAC
72  DRESP1   9         stress   STRESS   PSHELL                SVMB              1
73  +                2
74  DRESP1   14        complianCOMP
75  DRESP1   15        displ1   DISP                          TX                80
76  DRESP1   18        displ11  DISP                          TX                82
77  DRESP1   19        displ111DISP                           TX                76
78  $$
79  $$  OPTICONSTRAINTS Data
80  $$
81  $
82  $HMNAME OPTICONSTRAINTS          1displ1_const
83  $
84  DCONSTR           1        15-0.3      -0.2
85  $
86  $HMNAME OPTICONSTRAINTS          4displ11_const
87  $
88  DCONSTR           4        18-0.3      -0.2
89  $
90  $HMNAME OPTICONSTRAINTS          5displ111_const
91  $
92  DCONSTR           5        19-0.3      -0.2
93  $
94  DCONADD           6         1          4          5
95  $$
96  $$
97  $$    2.2        Mesh
98  $$-------------------------------------------------------------------------------$
99  $$  Nodes
100 GRID              2         125.0      0.0        0.0              1
101 GRID             42         125.0      45.859870.0                 1
102 GRID             43         ...
103 GRID             ...
```

```
104 $$
105 $  CTRIA6 Elements
106 CTRIA6      4720       1      42      44     467      43     469     470
107 CTRIA6      4721       1      42     467     463     470     468     465
108 CTRIA6      4722       1      44      46     471      45     473     474
109 CTRIA6      4723       1     ...
110 CTRIA6      ...
111 $$
112 $$
113 $$    2.4         Material and Element Properties
114 $$-------------------------------------------------------------------------------$
115 $HMNAME PROP                    1"design_prop" 4
116 $HWCOLOR PROP                   1       11
117 PSHELL          1       130.0          1               1         0.0
118 $HMNAME PROP                    2"non_design_prop" 4
119 $HWCOLOR PROP                   2       11
120 PSHELL          2       130.0          1               1         0.0
121 $$
122 $$  MAT1 Data
123 $$
124 $HMNAME MAT                     1"alu" "MAT1"
125 $HWCOLOR MAT                    1       11
126 MAT1            170000.0        0.34     2.71-9   2.3-5
127 MAT4            1    221.0
128 $$
129 $$
130 $$    2.5         Definition of Loads and Boundary Conditions
131 $$-------------------------------------------------------------------------------$
132 $HMNAME LOADCOL                  1"temp"
133 $HWCOLOR LOADCOL                 1       11
134 $$
135 $
136 TEMP            1    12156-180.0
137 TEMP            1    12155-180.0
138 TEMP            1    12154-180.0
139 TEMP            1    ...
140 TEMP            ...
141 $$
142 $$
143 ENDDATA
```

C
Bibliography

[1] S. Abrate. Free vibration, buckling, and static deflections of functionally graded plates. *Composites Science and Technology*, 66(14):2383 – 2394, 2006. doi: http://dx.doi.org/10.1016/j.compscitech.2006.02.032. ISSN: 0266-3538, Special Issue in Honour of Professor C.T. Sun.

[2] G. Allaire. *Shape Optimization by the Homogenization Method*. Springer, 2002. ISBN: 978-0-387-95298-7.

[3] V. Antonelli. High Speed Rotating chopper discs made of Carbon Fibre Reinforced Plastics (CFRP). In *Proceedings of DENIM 2012 – 1th Design and Engineering of Neutron Instruments Meeting*, Malmö, Feb. 2012.

[4] V. Antonelli. Verification of strength Corelli CFRPchopper disk. Technical report, Institute of Lightweight Structures, Technische Universität München, 2012.

[5] V. Antonelli. Design, manufacturing and testing of the New Generation of chopper discs for FRMII. Technical Report TUM-MW65/1501-TN, Institute of Lightweight Structures, Technische Universität München, Jan. 2015.

[6] V. Antonelli. Verification of strength of the Topas chopper disc. Technical Report TUM-MW65/1502-TN, Institute of Lightweight Structures, Technische Universität München, Mar. 2015.

[7] V. Antonelli, M. Wedekind, L. Krämer, and H. Baier. The design of a CFRP chopper disc for a time of flight spectrometer. In *Proceedings of ICCM 18 – 18th International Conference on Composite Materials*, 2011.

[8] V. Antonelli, M. Wedekind, L. Krämer, and H. Baier. The Effect of Production on the Efficiency of CFRP Chopper Disks for Time of Flight Spectroscopy. In *Proceedings of SEICO12 – 33nd International Technical Conference & Forum of the Society for the Advancement of Materials and Process Engineering Europe*, volume 12, pages 256–261, 2012. ISBN: 978-3-9523565-5-5.

[9] V. Antonelli, W. Lohstroh, and H. Baier. Feasibility study on a large chopper disc for a TOF spectrometer. In *Proceedings of ICCM 19 – 19th International Conference on Composite Materials*, pages 160–166, 2013. ISBN: 978-0-9696797-1-4.

[10] V. Antonelli, M. Weinzierl, and H. Baier. CFRP chopper discs: state of the art and long term perspective. In *Proceedings of DENIM 2015 – 4th Design and Engineering of Neutron Instruments Meeting*, Budapest, Sept. 2015.

[11] V. Antonelli, M. Weinzierl, and H. Baier. Feasibility study of a sandwich chopper disc for a time of flight (TOF) spectrometer. In *Proceedings of ICCM 20 – 20th International Conference on Composite Materials*, Copenhagen, July 2015.

[12] A. Arani, H. Karami, G. Gharehpetian, and M. Hejazi. Review of Flywheel Energy Storage Systems structures and applications in power systems and microgrids. *Renewable and Sustainable Energy Reviews*, 69:9 – 18, 2017. doi: https://doi.org/10.1016/j.rser.2016.11.166. ISSN: 1364-0321.

[13] S. Arnold, A. Saleeb, and N. Al-Zoubi. Deformation and Life Analysis of Composite Flywheel Disk and Multi-Disk Systems. Technical report, National Aeronautics and Space Administration, Glenn Research Center, Jan. 2001. NASA/TM2001-210578.

[14] ASTM D 3039:2002-12. Standard Test Method for Tensile Properties of Polymer Matrix Composite Materials, Dec. 2002.

[15] H. Baier. Über Algorithmen zur Ermittlung und Charakterisierung Pareto-optimaler Lösungen bei Entwurfsaufgaben elastischer Tragwerke. *Zeitschrift für Angewandte Mathematik und Mechanik*, 57:318–320, 1977.

[16] H. Baier. *Mathematische Programmierung zur Optimierung von Tragwerken insbesondere bei mehrfachen Zielen.* Dissertation, Technische Hochschule Darmstadt, 1978.

[17] H. Baier. Multidisciplinary Design Optimization, 2015.

[18] H. Baier, C. Seeßelberg, and B. Specht. *Optimierung in der Strukturmechanik.* Vieweg+Teubner Verlag, Braunschweig, 1994. ISBN: 978-3-322-90701-1.

[19] N. Bakhtiary. A New Approach for Sizing, Shape and Topology Optimization. *SAE International Congress and Exposition*, 1996.

[20] S. Baydoun. Study on the performance of a press-fitted joint in the framework of PI3-NG chopperdiscs by means of FEM based contact analyses. Technical Report TUM MW65/1506-TN, Institute of Lightweight Structures, Technische Universität München, Mar. 2014.

[21] S. Baydoun. Study on the criticality of interlaminar stresses in composite chopperdiscs such as the Pi3-NG by means of 3D FEM analyses. Technical Report TUM MW65/1401-TN, Institute of Lightweight Structures, Technische Universität München, Mar. 2016.

[22] D. Bender. Chapter 10 - Flywheels. In T. M. Letcher, editor, *Storing Energy*, pages 183–201. Elsevier, Oxford, 2016. doi: https://doi.org/10.1016/B978-0-12-803440-8.00010-5. ISBN: 978-0-12-803440-8.

[23] M. Bendse and O. Sigmund. *Topology Optimization*. Springer, 2004. doi: 10.1007/978-3-662-05086-6. ISBN: 978-3-662-05086-6.

[24] Biezeno/Grammel. *Technische Dynamik, Zweiter Band, Dampfturbinen und Brennkraftmaschinen*. Springer-Verlag, Berlin/Göttingen/Heidelberg, 1953. ISBN: 978-3-642-65190-8.

[25] J. Blaauwendraad. *Plates and FEM*. Springer, 2010. doi: 10.1007/978-90-481-3596-7. ISBN: 978-90-481-3595-0.

[26] B. Bolund, H. Bernhoff, and M. Leijon. Flywheel energy and power storage systems. *Renewable and Sustainable Energy Reviews*, 11(2):235 – 258, 2007. doi: http://dx.doi.org/10.1016/j.rser.2005.01.004. ISSN: 1364-0321.

[27] P. Böni. New concepts for neutron instrumentation. *Nuclear Instruments and Methods in Physics Research Section A: Accelerators, Spectrometers, Detectors and Associated Equipment*, 586(1):1–8, 2008. doi: http://dx.doi.org/10.1016/j.nima.2007.11.059.

[28] J.-F. Bonnans, J. Gilbert, C. Lemarechal, and C. Sagastizbal. *Numerical Optimization: Theoretical and Practical Aspects*. Springer-Verlag Berlin Heidelberg, 2. ed. edition, 2006. ISBN: 978-3-540-35445-1.

[29] M. Bürgle. Untersuchung von Welle-Nabe-Verbindungen einer CFK-Chopperscheibe. Bachelor's thesis, Technische Universität München, Aerospace Department, Institute of Lightweight Structures, Dec. 2016.

[30] X. Chen and M. M. Kostreva. *Methods of Feasible Directions: A Review*, pages 205–219. Springer US, Boston, MA, 2000. ISBN 978-1-4613-0301-5. doi: https://doi.org/10.1007/978-1-4613-0301-5_14.

[31] M. A. Conteh and E. C. Nsofor. Composite flywheel material design for high-speed energy storage. *Journal of Applied Research and Technology*, 14(3):184 – 190, 2016. doi: http://dx.doi.org/10.1016/j.jart.2016.04.005. ISSN: 1665-6423.

[32] J. Copley. On the use of multiple-slot multiple disk chopper assemblies to pulse thermal neutron beams. *Nuclear Instruments and Methods in Physics Research Section A: Accelerators, Spectrometers, Detectors and Associated Equipment*, 273(1): 67–76, 1988. doi: http://dx.doi.org/10.1016/0168-9002(88)90800-5. ISSN: 0168-9002.

[33] J. Copley. Optimized design of the chopper disks and the neutron guide in a disk chopper neutron time-of-flight spectrometer. *Nuclear Instruments and Methods in Physics Research Section A: Accelerators, Spectrometers, Detectors and Associated Equipment*, 291(3):519–532, 1990. doi: http://dx.doi.org/10.1016/0168-9002(90)90001-M. ISSN: 0168-9002.

[34] J. Copley. The Disk Chopper Spectrometer at NIST: The Good, The Bad and The Ugly. In *Proceedings of ICANS 17 – 17th Meeting of the International Collaboration on Advanced Neutron Sources*, 2005.

[35] J. Copley and J. Cook. The Disk Chopper Spectrometer at NIST: a new instrument for quasielastic neutron scattering studies. *Chemical Physics*, 292:477–485, 2003.

[36] J. Copley and T. Udovic. Neutron Time-of-Flight Spectroscopy. *Journal of Research of the National Institute of Standards and Technology*, 98(1):71–87, 1993.

[37] K. Coutinho and J. Costa. Compliance minimization using topology optimization method with tetrahedrical elements. In *Proceedings of COBEM 2011 - 21st Brazilian Congress of Mechanical Engineering*, Natal, Oct. 2011.

[38] DIN 65378:1989-11. Aerospace; fiber reinforced plastics; testing of unidirectional laminates; tensile test transverse to fiber direction, Nov. 1989.

[39] DIN EN 2561:1995-11. Aerospace series - Carbon fibre reinforced plastics - Unidirectional laminates - tensile test parallel to the fibre direction, Nov. 1995.

[40] DIN EN 2563:1997-03. Aerospace series - Carbon fibre reinforced plastics - Unidirectional laminates; determination of apparent interlaminar shear strength, Mar. 1997.

[41] DIN EN ISO 527-4:1997-07. Plastics – Determination of tensile properties – Part 4: Test conditions for isotropic and anisotropic fibre-reinforced plastic composites, July 1997.

[42] B. Dirr and H. Waller. Zum Problem der Berechnung der Eigenfrequenzen und Eigenformen elastischer ebener Kontinua. *Ingenieur-Archiv*, 43(2-3):74–91, 1974. doi: 10.1007/BF00537141. ISSN: 0020-1154.

[43] R. Freymann. *Strukturdynamik: Ein anwendungsorientiertes Lehrbuch*. Springer-Verlag Berlin Heidelberg, Berlin, Heidelberg, 2011. ISBN: 9783642196980.

[44] E. Friebe. Steifheit und Schwingungsverhalten von Kreissägeblättern. *Holz als Roh- und Werkstoff*, 28(9):349–357, 1970.

[45] Fujitsu. FUJITSU Server PRIMERGY RX200 S8 Dual socket 1U rack server, Nov. 2015.

[46] C. W. Gabrys and C. E. Bakis. Design and Manufacturing of Filament Wound Elastomeric Matrix Composite Flywheels. *Journal of Reinforced Plastics and Composites*, 16(6):488–502, 1997. doi: http://dx.doi.org/10.1177/073168449701600601.

[47] R. Gasch, R. Nordmann, and H. Pfützner. *Rotordynamik*. Springer, 2006. ISBN: 3-540-41240-9.

[48] R. Gasch, K. Knothe, and R. Liebich. *Strukturdynamik: Diskrete Systeme und Kontinua*. Springer, 2012. ISBN: 9783540889762.

[49] G. Genta. Some considerations on the constant stress disc profile. *Meccanica*, 24(4): 235–248, 1989. ISSN: 0025-6455.

[50] G. Gogu. Kritische Drehzahlen von Kreissägeblättern. *Holz als Roh- und Werkstoff*, 46(5):173–182, 1988.

[51] G. Gogu. Die Verwölbung von Kreissägeblättern unter dem Einfluß von Membranspannungen. *Holz als Roh- und Werkstoff*, 46(4):135–140, 1988.

[52] G. Gogu. Berechnung der Eigenfrequenzen von Kreissägeblättern mit der Finite-Element-Methode. *Holz als Roh- und Werkstoff*, 46(3):91–100, 1988.

[53] H. Graf. Untersuchung von rotordynamischen Effekten an CFK-Chopper-Scheiben. Term paper, Technische Universität München, Aerospace Department, Institute of Lightweight Structures, Apr. 2015.

[54] C. Grätz. Geometrieuntersuchung an schnellumlaufenden Chopperscheiben. Master's thesis, Technische Universität München, Aerospace Department, Institute of Lightweight Structures, 2009.

[55] F. Gunsing, U. Abbondanno, and G. Aerts. Status and outlook of the neutron time-of-flight facility (n-tof) at CERN. *Nuclear Instruments and Methods in Physics Research Section B: Beam Interactions with Materials and Atoms*, 261(12):925–929, 2007. doi: http://dx.doi.org/10.1016/j.nimb.2007.03.096. ISSN: 0168-583X.

[56] G. Günther and M. Russina. Background optimization for the neutron time-of-flight spectrometer NEAT. *Nuclear Instruments and Methods in Physics Research Section A: Accelerators, Spectrometers, Detectors and Associated Equipment*, 828:250 – 261, 2016. doi: http://dx.doi.org/10.1016/j.nima.2016.05.022. ISSN: 0168-9002.

[57] Z. Gürdal and R. Haftka. *Elements of Structural Optimization*. Kluwer Academic Publishers Group, 1990. ISBN: 0-7923-1505-7.

[58] Z. Gürdal, R. Haftka, and P. Hajela. *Design and Optimization of Laminated Composite Materials*. John Wiley & Sons, 1999. ISBN: 978-0-471-25276-4.

[59] W. Gutierrez-Wing. *Modal Analysis of Rotating Machinery Structures*. Dissertation, Department of Mechanical Engineering, Imperial College London, University of London, Sept. 2003.

[60] L. Hart-Smith. Chapter 3.5 – Predictions of the original and truncated maximum-strain failure models for certain fibrous composite laminates. In M. Hinton, A. Kaddour, and P. Soden, editors, *Failure Criteria in Fibre-Reinforced-Polymer Composites*, pages 179–218. Elsevier, Oxford, 2004. doi: 10.1016/B978-008044475-8/50009-3. ISBN: 978-0-08-044475-8.

[61] L. Harzheim. *Strukturoptimierung, Grundlagen und Anwendung*. Wissenschaftlicher Verlag Harri Deutsch GmbH, 2008. ISBN 978-3-8171-1809-0.

[62] J. Haslinger and P. Neittaanmäki. *Finite Element Approximation for Optimal Shape, Material and Topology Design*. John Wiley & Sons Ltd, 1996. ISBN: 978-0-471-95850-5.

[63] Haslinger, J. and Mäkinen, R.A.E. *Introduction to Shape Optimization: Theory, Approximation, and Computation*. SIAM, 2003. doi: http://dx.doi.org/10.1137/1.9780898718690.

[64] Heinz Maier-Leibnitz Zentrum. Powtex, 2016. URL `http://www.mlz-garching.de/powtex`. Last accessed on 2016-02-23.

[65] Heinz Maier-Leibnitz Zentrum. Toftof, 2016. URL `http://www.mlz-garching.de/toftof`. Last accessed on 2016-02-03.

[66] Helmholtz-Zentrum Berlin. Overview NEAT II. `https://www.helmholtz-berlin.de/media/media/zentrum/perspektiven/rz_neat_detail.pdf`, 2015. Last accessed on 2015-11-10.

[67] N. Hiroshima, H. Hatta, M. Koyama, J. Yoshimura, Y. Nagura, K. Goto, and Y. Kogo. Spin test of three-dimensional composite rotor for flywheel energy storage system. *Composite Structures*, 136:626 – 634, 2016. doi: http://dx.doi.org/10.1016/j.compstruct.2015.10.035. ISSN: 0263-8223.

[68] U. Hollburg. *Maschinendynamik*. Oldenbourg, München [u.a.], 2., verb. und erw. aufl. edition, 2007. ISBN: 978-3-486-57898-0.

[69] HyperWorks. *OptiStruct User's Guide*. Altair, 14.0 edition, 2015.

[70] A. Inc. *Rotordynamic Analysis Guide*, 12.1 edition, Nov. 2009.

[71] R. Jackson, L. LeGore, Z. Yang, P. Kleban, and B. Frederick. Application of the interleaved comb chopper to time-of-flight electron spectrometry. *Surface Science*, 502-503:240–248, 2002. doi: http://dx.doi.org/10.1016/S0039-6028(01)01951-3. ISSN: 0039-6028.

[72] P. Kelly. Mechanics Lecture Notes Part III: Foundations of Continuum Mechanics, 2015.

[73] G. R. Kirchhoff. *Gesammelte Abhandlungen*. Barth, Leipzig, 1882.

[74] K. Knothe and H. Wessels. *Finite Elemente*. Springer, 2008. ISBN: 978-3-540-72188-8.

[75] Y. Kogo, H. Hatta, H. Kawada, T. Shigemura, H. Ohnabe, T. Mizutani, and F. Tomioka. Spin Burst Test of Carbon-Carbon Composite Disk. *Journal of*

Composite Materials, 32(11):1016–1035, 1998. doi: http://dx.doi.org/10.1177/002199839803201101.

[76] K. König. Zur Berechnung von Schwingungen in bewegten Strukturen. Technical report, VDI Bericht 536, 1984.

[77] M. Krack, M. Secanell, and P. Mertiny. Advanced optimization strategies for cost-sensitive design of energy storage flywheel rotors. In *Proceedings of the International SAMPE Symposium and Exhibition of the Society for the Advancement of Materials and Process Engineering*, 2010.

[78] M. Krack, M. Secanell, and P. Mertiny. Cost optimization of hybrid composite flywheel rotors for energy storage. *Structural and Multidisciplinary Optimization*, 41 (5):779–795, may 2010. doi: http://dx.doi.org/10.1007/s00158-009-0469-y. ISSN: 1615-1488.

[79] M. Krack, M. Secanell, and P. Mertiny. Rotor Design for High-Speed Flywheel Energy Storage Systems. In R. Carbone, editor, *Energy Storage in the Emerging Era of Smart Grids*. InTech, 2011. doi: 10.5772/18359. ISBN: 978-953-307-269-2.

[80] J. Launhardt. Numerical Contact Simulation of the Shaft-Hub Joint-Connection of CFRP Chopper Disks. Bachelor's thesis, Technische Universität München, Aerospace Department, Institute of Lightweight Structures, Aug. 2015.

[81] C. Le, J. Norato, T. Bruns, C. Ha, and D. Tortorelli. Stress-based topology optimization for continua. *Structural and Multidisciplinary Optimization*, 41(4):605–620, Apr. 2010. ISSN 1615-1488. doi: 10.1007/s00158-009-0440-y.

[82] R. Lechner. Multi-chopper time-of-flight spectrometers for spallation sources. *Physica B: Condensed Matter*, 276-278:67–68, 2000. doi: http://dx.doi.org/10.1016/S0921-4526(99)01329-0. ISSN: 0921-4526.

[83] M. MacCamhaoil. Static and Dynamic Balancing of Rigid Rotors. Technical report, Brürl and Kjaer, 1976.

[84] C. Mahieux. Cost effective manufacturing process of thermoplastic matrix composites for the traditional industry: the example of a carbon-fiber reinforced thermoplastic flywheel. *Composite Structures*, 52(3):517 – 521, 2001. doi: http://dx.doi.org/10.1016/S0263-8223(01)00041-1. Design and Manufacturing of Composite Structures.

[85] R. Meske, J. Sauter, and E. Schnack. Nonparametric gradient-less shape optimization for real-world applications. *Structural and Multidisciplinary Optimization*, 30(3): 201–218, 2005. doi: http://dx.doi.org/10.1007/s00158-005-0518-0. ISSN: 1615-1488.

[86] M. Mitradjieva-Daneva. *Feasible Direction Methods for Constrained Nonlinear Optimization*. Dissertation, Division of Optimization, Department of Mathematics, Linköping University, Sweden, 2007. ISBN: 978-91-85715-11-4.

[87] C. Mote and R. Szymani. A review report on principal developments in thin circular saw vibration and control research. *Holz als Roh- und Werkstoff*, 35(5):189–196, 1977. doi: 10.1007/BF02610942. ISSN: 0018-3768.

[88] C. D. Mote, Jr. Free Vibration of Initially Stressed Circular Disks. *Journal of Engineering for Industry*, 87(2):258–264, May 1965. ISBN: 1087-1357.

[89] S. Mousavi, F. Faraji, A. Majazi, and K. Al-Haddad. A comprehensive review of Flywheel Energy Storage System technology. *Renewable and Sustainable Energy Reviews*, 67:477–490, 2017. doi: https://doi.org/10.1016/j.rser.2016.09.060. ISSN: 1364-0321.

[90] M. Neto, A. Amaro, L. Roseiro, J. Cirne, and R. Leal. *Engineering Computation of Structures: The Finite Element Method*. Springer, 2015. doi: 10.1007/978-3-319-17710-6. ISBN: 978-3-319-17709-0.

[91] G. Niemann, H. Winter, and B.-R. Höhn. *Maschinenelemente*, volume Band 1: Konstruktion und Berechnung von Verbindungen, Lagern, Wellen. Springer-Verlag Berlin Heidelberg, 2005. doi: 10.1007/b137557. ISBN: 978-3-540-25125-5.

[92] A. Olason and D. Tidman. Methodology for Topology and Shape Optimization in the Design Process. Master's thesis, Chalmers University of Technology, Department of Applied Mechanics, Division of Dynamics, Nov. 2010.

[93] G. Pahlitzsch and B. Rowinski. Über das Schwingungsverhalten von Kreissägeblättern – Zweite Mitteilung: Ermittlung und Auswirkungen der kritischen Drehzahlen und Eigenfrequenzen der Sägeblätter. *Holz als Roh- und Werkstoff*, 24(8):341–346, 1966.

[94] J. Pajot. Optimal Design Exploration Using Global Response Surface Method: Rail Crush. Technical report, Altair, 2013.

[95] Pjrensburg. Example of cylindrical flywheel rotor assembly, July 2012. URL `https://en.wikipedia.org/wiki/Flywheel_energy_storage`. Last accessed on 2017-06-29.

[96] T. Pühlhofer. Finite Element Analyse Chopper Disc6 unter besonderer Beachtung des 1. Stufensprungs bei r=260 mm. Technical Report TUM-MW65/0408-TN, Institute of Lightweight Structures, Technische Universität München, Dec. 2004.

[97] T. Pühlhofer. Finite Element Analyse der Astrium Chopper-Scheibe Disc5, sowie Maßnahmen zur Drehzahlsteigerung. Technical Report TUM-MW65/0407-TN, Institute of Lightweight Structures, Technische Universität München, Dec. 2004.

[98] T. Pühlhofer. Wesentliche Festigkeitseigenschaften und Tendenzen rotierender FVW Scheiben konstanter Dicke mit Nabenbohrung und Fensterausschnitten. Technical Report TUM-MW65/0402-TN, Institute of Lightweight Structures, Technische Universität München, May 2004.

[99] T. Pühlhofer. Studie zu Chopperscheiben mit großem Fensterausschnitt Design Wuchtproblematik Analyse. Technical Report TUM-MW65/0502-TN, Institute of Lightweight Structures, Technische Universität München, Feb. 2005.

[100] T. Pühlhofer. Chopperscheibe NCS016-S1 - Ursachen der Rißbildung nach dem Schleudertest. Technical Report TUM-MW65/0703-TN, Institute of Lightweight Structures, Technische Universität München, May 2007.

[101] T. Pühlhofer and J. Wittmann. Rechnerische Untersuchung von Maßnahmen zur Erhöhung der Betriebsdrehzahl von Chopper-Scheiben. Technical Report TUM-MW65/0308-TN, Institute of Lightweight Structures, Technische Universität München, May 2004.

[102] T. Pühlhofer and J. Wittmann. Finite Element Analyse – Astrium Chopper Disc3, Disc4 und 6 und Modifikationen zur Drehzahlsteigerung. Technical Report TUM-MW65/0403-TN, Institute of Lightweight Structures, Technische Universität München, 2004.

[103] T. Pühlhofer, H. Baier, L. Krämer, and T. Unruh. Design, manufacturing and testing of high speed rotating CFRP chopper discs. In *Proceedings of the 27th International SAMPE Europe Conference 2006 of the Society for the Advancement of Materials and Process Engineering*, pages 327–332, 2006.

[104] S. Rao. *Engineering Optimization*. John Wiley & Sons, 2009. ISBN: 978-0-470-18352-6.

[105] H. Reißner. Über die unsymmetrische Biegung dünner Kreisringplatten. *Ingenieur-Archiv*, 1(1):72–83, 1929. doi: 10.1007/BF02079709. ISSN: 0020-1154.

[106] F. Rieg, R. Hackenschmidt, and B. Alber-Laukant. *Finite Elemente Analyse für Ingenieure*. Carl Hanser Verlag, 2014. doi: 10.3139/9783446443181.

[107] B. Rowinski. *Schwingungsverhalten und Schwingungsursachen von Kreissägeblättern*. Dissertation, Technische Hochschule Carolo-Wilhelmina zu Braunschweig, Fakultät für Maschinenwesen, 1967.

[108] G. Rozvany and B. Karihaloo, editors. *Structural Optimization*. Kluwer Academic Publishers, 1988. doi: 10.1007/978-94-009-1413-1. ISBN: 978-94-009-1413-1.

[109] J. Rückert. *Kirchhoff Plates and Large Deformations - Modelling and C^1-continuous Discretization*. Dissertation, Department of Mathematics at Chemnitz University of Technology, Chemnitz, Apr. 2013.

[110] J. Rückert and A. Meyer. *Kirchhoff plates and large deformation*, volume 2012,01 of *CSC*. Techn. Univ., Fak. für Mathematik, Chemnitz, 2012. ISSN: 1864-0087.

[111] M. Schatz. *Multicriteria Optimization of Fiber Composite Structures with Respect to Structural Performance and Manufacturing*. Dissertation, Technische Universität München, 2016.

[112] M. Schatz, A. Hermanutz, and H. Baier. Multi-criteria optimization of an aircraft propeller considering manufacturing. *Structural and Multidisciplinary Optimization*, pages 1–13, 2016. doi: http://dx.doi.org/10.1007/s00158-016-1541-z. ISSN: 1615-1488.

[113] P. Schulz. Numerische Optimierung einer Wellen-Nabe-Verbindung einer CFK Chopperscheibe. Term paper, Technische Universität München, Aerospace Department, Institute of Lightweight Structures, Oct. 2015.

[114] A. Schumacher. *Optimierung Mechanischer Strukturen*. Springer, 2013. doi: 10.1007/978-3-642-34700-9. ISBN: 978-3-642-34699-6.

[115] C. Schwarz. Analysis and extension of composite optimization under manufacturing and strength constraints with optistruct. Master's Thesis, Technische Universität München, Aerospace Department, Institute of Lightweight Structures, 2013.

[116] S. Sepp. Rotordynamische Strukturanalyse von CFK Chopper Scheiben. Term paper, Technische Universität München, Aerospace Department, Institute of Lightweight Structures, Aug. 2016.

[117] O. Sigmund. On the Design of Compliant Mechanisms Using Topology Optimization. *Mechanics of Structures and Machines: An International Journal*, 25(4):493–524, 1997. doi: http://dx.doi.org/10.1080/08905459708945415.

[118] J.-Y. So, M. Moon, S.-J. Cho, Y.-H. Choi, C.-H. Lee, and J.-G. Park. Current design of disk chopper time-of-flight spectrometer at KAERI. *Journal of Neutron Research*, 15(1):23–30, 2007. ISBN: 1023-8166.

[119] R. Southwell. On the Free Transverse Vibrations of a Uniform Circular Disc Clamped at its Centre; and on the Effects of Rotation. *Philosophical Transactions of the Royal Society of London*, A(101):133–153, 1922.

[120] D. Srikrishnanivas. Rotor Dynamic Analysis of RM12 Jet Engine Rotor using ANSYS. Master's thesis, Department of Mechanical Engineering, Blekinge Institute of Technology, Karlskrona, Sweden, 2012.

[121] H. Stelzer, C. Weißbacher, H. Soltner, F. Janssen, M. Butzek, T. Kozielewski, B. Lindenau, M. Monkenbusch, and M. Ohl. Investigation of the temperature rise due to eddy currents in large chopper disks operated at polarized neutron beamlines. *Nuclear Instruments and Methods in Physics Research Section A: Accelerators, Spectrometers, Detectors and Associated Equipment*, 594(2):228–231, 2008. doi: http://dx.doi.org/10.1016/j.nima.2008.06.040. ISSN: 0168-9002.

[122] W. Stephan and R. Postl. *Schwingungen elastischer Kontinua*, volume 72 of *Leitfäden der angewandten Mathematik und Mechanik*. Teubner, Stuttgart, 1995. ISBN: 3519023776.

[123] P. Strobach. Entwicklung eines Sandwichchoppers. Term paper, Technische Universität München, Aerospace Department, Institute of Lightweight Structures, 2013.

[124] M. Strobl, M. Bulat, and K. Habicht. The wavelength frame multiplication chopper system for the ESS test beamline at the BER II reactor – a concept study of a fundamental ESS instrument principle. *Nuclear Instruments and Methods in Physics Research Section A: Accelerators, Spectrometers, Detectors and Associated Equipment*, 705:74–84, 2013. doi: http://dx.doi.org/10.1016/j.nima.2012.11.190. ISSN: 0168-9002.

[125] F. Sturm. Shape Optimization of Integral Hinges in a Compliant Mechanism Rib of a Morphing Wing Airfoil. Master's Thesis, Technische Universität München, Aerospace Department, Institute of Lightweight Structures, 2016.

[126] R. Szymani and J. Mote, C.D. Principal developments in thin circular saw vibration and control research. *Holz als Roh- und Werkstoff*, 35(6):219–225, 1977. ISSN: 0018-3768.

[127] A. Ter-Gazarian. *Energy Storage for power systems*. Peter Peregrinus Ltd., 1994. ISBN: 0-86341-264-5.

[128] J. Tomblin and W. Seneviratne. Laminate Statistical Allowable Generation for Fiber-Reinforced Composite Materials: Lamina Variability Method. Technical Report NOT/FAA/Ar-06/53, U.S. Department of Transportation, Federal Aviation Administration, Air Traffic Organization Operations Planning, Office of Aviation Research and Development, Jan. 2009.

[129] A. Tura. Computer Aided Design, 2014.

[130] J. Tzeng, R. Emerson, and P. Moy. Composite Flywheel Development for Energy Storage. Technical report, U.S. Army Research Laboratory, Jan. 2005. ARL-TR-3388.

[131] J. Tzeng, R. Emerson, and P. Moy. Composite flywheels for energy storage. *Composites Science and Technology*, 66(14):2520 – 2527, 2006. doi: http://dx.doi.org/10.1016/j.compscitech.2006.01.025. ISSN: 0266-3538, Special Issue in Honour of Professor C.T. Sun.

[132] T. Unruh, J. Neuhaus, and W. Petry. The high-resolution time-of-flight spectrometer TOFTOF. *Nuclear Instruments and Methods in Physics Research Section A: Accelerators, Spectrometers, Detectors and Associated Equipment*, 580(3):1414–1422, 2007. doi: http://dx.doi.org/10.1016/j.nima.2007.07.015. ISSN: 0168-9002.

[133] T. Unruh, J. Neuhaus, and W. Petry. Erratum to "'the high-resolution time-of-flight spectrometer TOFTOF"' [nucl. instr. and meth. a 580 (2007) 1414-1422]. *Nuclear Instruments and Methods in Physics Research Section A: Accelerators, Spectrometers, Detectors and Associated Equipment*, 585(3):201, 2008. doi: http://dx.doi.org/10.1016/j.nima.2007.11.019. ISSN: 0168-9002.

[134] J. Vance, F. Zeidan, and B. Murphy. *Machinery vibration and rotordynamics*. Wiley, 2010. ISBN: 978-0-471-46213-2.

[135] G. Vanderplaats. *Multidiscipline Design Optimization: Textbook*. Vanderplaats Research & Development, Incorporated, 2007. ISBN: 9780944956045.

[136] A. Vickery and P. Deen. Choppers to optimise the repetition rate multiplication technique on a direct geometry neutron chopper spectrometer. *Review of Scientific Instruments*, 85(11):115103, 2014. doi: http://dx.doi.org/10.1063/1.4900958.

[137] V. Vullo and F. Vivio. *Rotors: Stress Analysis and Design*. Springer-Verlag Mailand, 2013. ISBN: 978-88-470-2561-5.

[138] P. Wang, B. Yang, and W. Cai. Development of a bandwidth limiting neutron chopper for {CSNS}. *Nuclear Instruments and Methods in Physics Research Section A: Accelerators, Spectrometers, Detectors and Associated Equipment*, 792:56–60, 2015. doi: http://dx.doi.org/10.1016/j.nima.2015.04.047. ISSN: 0168-9002.

[139] M. Weinzierl. A Study of the Structural Dynamics of Chopper Disks. Master's thesis, Technische Universität München, Aerospace Department, Institute of Lightweight Structures, May 2014.

[140] M. Weinzierl. Design einer neuen Nabe für die NEAT II Chopper Scheiben. Technical Report TUM-MW65/1505-TN, Institute of Lightweight Structures, Technische Universität München, Sept. 2015.

[141] M. Weinzierl and H. Baier. Leichtbau bei extrem schnell rotierenden Scheiben für neutronenphysikalische Versuchsanlagen. In *Technisch-wissenschaftliche Seminarreihe: Hochleistungsstrukturen im Leichtbau*, Garching bei München, Dec. 2015. Lehrstuhl für Leichtbau.

[142] M. Weinzierl and H. Baier. Design and optimization of a hub for a CFRP disk rotating at a very high speed. In *Proceedings of ICCS 19 – 19th International Conference on Composite Structures*, Porto, Sept. 2016.

[143] M. Weinzierl and H. Baier. Chopper Supplier Forum 2016 Chopper disk manufacturer update. In *Proceedings of DENIM 2016 – 5th Design and Engineering of Neutron Instruments Meeting*, Lund, Sept. 2016.

[144] M. Weinzierl, V. Antonelli, M. Schatz, and H. Baier. A study of the structural dynamics of CFRP chopper disks. In *Proceedings of the 9th SAMPE Europe Technical Conference of the Society for the Advancement of Materials and Process Engineering*, pages 172–178, Sept. 2014. ISBN: 978-90-821727-1-3.

[145] M. Weinzierl, H. Baier, L. Krämer, and V. Antonelli. Design and certification of the chopper disks for the NEAT II TOF spectrometer: A lesson learned. In *Proceedings of DENIM 2015 – 4th Design and Engineering of Neutron Instruments Meeting*, Budapest, Sept. 2015.

[146] M. Weinzierl, M. Schatz, V. Antonelli, and H. Baier. Structural Design Optimization of CFRP Chopper Disks. In *Proceedings of ICCS 18 – 18th International Conference on Composite Structures*, Lisbon, June 2015.

[147] M. Weinzierl, V. Antonelli, and H. Baier. Design and certification of the chopper disks for the NEAT II TOF spectrometer. In *Proceedings of ECCM 17 – 17th European Conference on Composite Materials*, Munich, June 2016. ISBN: 978-3-00-053387-7.

[148] M. Weinzierl, M. Schatz, V. Antonelli, and H. Baier. Structural design optimization of CFRP chopper disks. *Composite Structures*, 140:351–359, Apr. 2016. ISSN 0263-8223. doi: http://dx.doi.org/10.1016/j.compstruct.2015.12.016.

[149] A. v. Well. Double-disk chopper for neutron time-of-flight experiments. *Physica B: Condensed Matter*, 180:959–961, 1992. doi: http://dx.doi.org/10.1016/0921-4526(92)90521-S. ISSN: 0921-4526.

[150] J. Wiedemann. *Leichtbau: Elemente und Konstruktion*. Klassiker der Technik. Springer-Verlag Berlin Heidelberg, Berlin, Heidelberg, 3. edition, 2007. ISBN: 9783540336570.

[151] C.-H. Yang and S.-C. Huang. Coupling Vibrations in Rotating Shaft-Disk-Blades System. *Journal of Vibration and Acoustics*, 129(1):48–57, Feb. 2007. doi: http://dx.doi.org/10.1115/1.2221328.

[152] V. Yastrebov. *Computational contact mechanics: geometry, detection and numerical techniques*. Dissertation, Ecole Nationale Supérieure des Mines de Paris, 2011. pastel-00657305.

[153] S. Y. Yoon, Z. Lin, and P. E. Allaire. *Control of Surge in Centrifugal Compressors by Active Magnetic Bearings*. Springer, 2013. doi: 10.1007/978-1-4471-4240-9. ISBN: 978-1-4471-4239-3.

[154] K. Zhang, L. Jiang, X. Dai, J. Dong, and X. Zhang. Prototype of bandwidth limiting neutron chopper. *Physics Procedia*, 26:55–60, 2012. doi: http://dx.doi.org/10.1016/j.phpro.2012.03.009. Proceedings of the first two meetings of the Union of Compact Accelerator-Driven Neutron Sources.

[155] Zwick Roell. Testing Machines for Biaxial Tensile Tests, 2016. URL https://www.zwick.com/en/biaxial-testing-machines/cruciform-testing-machine. Last accessed on 2017-07-12.